Implementation of a high resolution optical feedback interferometer for microfluidics applications

Raul da Costa Moreira

To cite this version:

Raul da Costa Moreira. Implementation of a high resolution optical feedback interferometer for microfluidics applications. Optics / Photonic. Institut National Polytechnique de Toulouse - INPT, 2019. English. NNT : 2019INPT0028 . tel-04166316

HAL Id: tel-04166316
https://theses.hal.science/tel-04166316

Submitted on 19 Jul 2023

THÈSE

En vue de l'obtention du

DOCTORAT DE L'UNIVERSITÉ DE TOULOUSE

Délivré par :
Institut National Polytechnique de Toulouse (Toulouse INP)

Discipline ou spécialité :
Photonique et système optoélectronique

Présentée et soutenue par :
M. RAUL DA COSTA MOREIRA
le jeudi 6 juin 2019

Titre :

Implementation of a high resolution optical feedback interferometer for microfluidics applications

---

Ecole doctorale :
Génie Electrique, Electronique, Télécommunications (GEET)

Unité de recherche :
Laboratoire d'Analyse et d'Architecture des Systèmes (LAAS)

Directeur(s) de Thèse :
M. THIERRY BOSCH
M. JULIEN PERCHOUX

Rapporteurs :
M. ERIC LACOT, UNIVERSITE GRENOBLE ALPES
M. SANTIAGO ROYO, CD6 Universitat Politecnica Catalunya

Membre(s) du jury :
Mme ALEXANDRA ALEXANDROVA, UNIVERSITE LYON 1, Président
M. GUY PLANTIER, EC SUP ELECTRONIQUE OUEST, Invité
M. JULIEN PERCHOUX, TOULOUSE INP, Membre
Mme KARINE LOUBIERE, CNRS TOULOUSE, Membre
M. THIERRY BOSCH, TOULOUSE INP, Membre

IMPLEMENTATION OF A HIGH RESOLUTION OPTICAL FEEDBACK INTERFEROMETER FOR MICROFLUIDICS APPLICATIONS

Implémentation d'un Interféromètre par Réinjection Optique à Haute Résolution pour les Applications Microfluidiques

Doctorat de l'UNIVERSITÉ DE TOULOUSE

Institut National Polytechnique de Toulouse

(INP Toulouse)

École doctorale et spécialité :

GEET : Photonique et Systèmes Optoélectroniques

Unité de Recherche :

Laboratoire d'Analyse et d'Architecture des Systèmes (LAAS-CNRS) – équipe OSE, France.

Directeur de Thèse : Prof. Thierry BOSCH

Co-directeur : Dr. Julien PERCHOUX

Abstract

Recent progress of interferometric sensors based on the optical feedback in a laser diode have demonstrated possibility for measurement of flow rates and flow-profiles at the micro-scale. That type of compact and embedded sensors is very promising for a research and industrial field –microfluidics – that is a growing domain of activities, at the frontiers of the physics, the chemical science, the biology and the biomedical. However, the acquisition of flow rate or local velocity at high resolution remains a very challenging issue, and the sensors that have been proposed so far did not have been giving sufficient information on the nature of the particles flowing.

The present thesis is driven by the implementation, validation and evaluation of the sensing performances of the optical feedback interferometry technology in both chemical and biomedical fields of applications. The elaboration of a new generation of sensors that will provide both a high spatial resolution for 2D Doppler imaging is presented, as well as a methodology that gives further information on the flowing particles concentration and/or dimensions. Then, a new embedded optical feedback interferometry imager for flowmetry has been realized using a 2-axis beam-steering mirror mounted on Micro-Electro-Mechanical Systems (MEMS) thus taking the full advantage of the compactness offered by the optical feedback interferometry sensing scheme.

While previous works on optical feedback interferometry flowmetry have been limited to high particle densities fluids in single or multiple scattering regimes, we present also a sensing technique based on the optical feedback interferometry scheme in a laser diode that enables single particle detection at micro and nanoscales through the Doppler-Fizeau effect. Thanks to the proposed signal processing, this sensing technique can detect the presence of single spherical polystyrene micro/nanospheres seeded in watery suspensions, and measure their flow velocity, even when their diameter is below half the laser wavelength. It discriminates particle by their diameter up to a ratio of 5 between large and small ones while most of the technologies for particle characterization is bulk and requires manipulation of the fluid with small volume handling, precise flow and concentration control.

Altogether, the results presented in this thesis realize a major improvement for the use of optical feedback interferometry in the chemical engineering or biomedical applications involving micro-scale flows.

Keywords: *interferometry; Doppler imaging; optical feedback; micro/nanoparticle characterization; flowmetry; self-mixing.*

Résumé

Les progrès récents des capteurs interférométriques basés sur la réinjection optique dans une diode laser ont démontré la possibilité de mesurer des débits d'écoulements et des profils de vitesses d'écoulement à l'échelle micrométrique. Ce type de capteurs compacts et intégrés est très prometteur pour un domaine - la microfluidique - qui est en expansion, aux frontières de la physique, de la chimie, de la biologie et du biomédical. Cependant, la mesure du débit ou de la vitesse locale en haute résolution reste un problème très complexe et les capteurs proposés jusqu'à présent n'ont pas fourni d'informations sur la nature des particules qui s'écoulent.

La présente thèse porte sur la mise en œuvre, la validation et l'évaluation des performances de détection de la technologie OFI dans les domaines d'applications chimiques et biomédicaux. L'élaboration d'une nouvelle génération de capteurs qui fourniront à la fois une haute résolution spatiale pour l'imagerie Doppler 2D est présentée ainsi qu'une approche novatrice permettant de fournir des informations supplémentaires sur la concentration et/ou les dimensions des particules en mouvement. Ensuite, un imageur Doppler par réinjection optique, embarqué dans un système compact pour la débitmétrie a été réalisé à l'aide d'un micro-miroir monté sur des systèmes micro-électromécaniques (MEMS), tirant ainsi pleinement parti de la compacité offerte par le système de détection par réinjection optique.

Alors que les travaux précédents sur la débitmétrie par réinjection optique ont été limités aux fluides à haute densité de particules dans des régimes de diffusion simples ou multiples, nous présentons également une technique permettant la détection de particules uniques de dimensions micro et nanométriques à travers l'effet Doppler-Fizeau. Grâce au traitement du signal proposé, cette technique de détection peut détecter la présence de micro/nanosphères de polystyrène sphériques uniques ensemencées dans des suspensions aqueuses et mesurer leur vitesse d'écoulement, même lorsque leur diamètre est inférieur à la moitié de la longueur d'onde du laser. Cette méthode présente de nombreux avantages par rapport aux méthodes habituelles qui nécessitent une manipulation du fluide, dans des volumes toujours plus petits avec un contrôle précis du débit et de la concentration.

L'ensemble des aspects traités dans cette thèse représente une avancée majeure pour l'utilisation des capteurs par réinjection dans les applications d'ingénierie chimique ou biomédicale impliquant des écoulements à micro-échelle.

Mots clés*: interférométrie; Imagerie Doppler; réinjection optique; caractérisation des micro/ nanoparticules; débitmétrie; auto-mélange.*

Acknowledgements

May the splendor of the bright star watching for the good in the human Intellect be glorified. May It shine, enthroned over each human heart, repelling the evil of ignorance away from the human mind.

Here I am, being initiated to the high university degree of *Philosophiae Doctor* in the renowned University of Toulouse, what a happiness! May I contribute to watch for the health of wisdom in this world, by the blessings from the healing loving kindness. May I always remember, and never forget, that science should be developed under the aegis of a fraternal family in favor of the common well-being of the whole humanity, where we must act as true companions of each other. How good and pleasant it is, when the charity of love and the rigor of knowledge can live together as brothers in union, for harmony.

We are never alone although our own efforts. I share the fruits of my work, first of all, with my family. They have always supported my personal formation as social being. My very deep gratitude to my wife Carolina, with who I live fully aware of the invencible powers of love. I thank my mentors, that guided me and offered me tools to shape well my mind. Thanks to my fellows that along this life journey have been exchanging their perspectives and experiences.

I am grateful to Thierry BOSCH for sharing his senior mentorship in the field of laser self-mixing as my thesis advisor. My very special thanks to Julien PERCHOUX for his very dynamic guidance, always present sharing with me the gifts of his sharp mind. It has been a great honor working under the direct supervision of both, as main representatives of the OSE team (LAAS-CNRS).

My sincere thanks for all support of my colleagues and friends: Evelio R. MIQUET, Antonio LUNA A., Reza ATASHKHOOEI, Yu ZHAO, Adam QUOTB, Clément TRONCHE, Francis JAYAT, Emmanuelle TRONCHE, Francis BONY, Olivier BERNAL, Hélène TAP, Han-Cheng SEAT, Jalal AL R., Fernando URGILES, Mengkoung VENG, Einar KNUDSEN, Bastien GRIMALDI, Harris APRIYANTO, Laura LE BARBIER, Florentin BIGOT, Lavinia CIOTIRCA, Gautier RAVET, Françoise LIZION, Jacson BARTH, Mohanad.

I am very grateful to my country, Brazil, that gave me all the conditions to grow. France, thank you for welcome me, allowing me to help as a citizen of the world. Special thanks to all colleagues from ESEO Angers for the opportunities to develop further my teaching skills grasped during my PhD. Godspeed!

Contents

INTRODUCTION

Since the invention of the light microscope, our capabilities to discover and explore the microscopic universe have been increasing with time. The scientific discoveries have been revealing a world full of wonders offering possibilities of scientific advancements involving multiple fields of applications.

Much of this development has been possible thanks to the evolution of the microelectronics in particular with the exponential growth of the semiconductor industry, and the continuous progress in the processes of device miniaturization has benefited to the design of microelectromechanical systems.

In this context, the microfluidics emerged as a breakthrough technology with a multidisciplinary field of applications involving engineering, physics, chemistry and biology. In the actual microfluidics research and development, we can highlight two main domains of applications: the chemical one, that includes micromixers, microreactors, lab-on-chip and particle characterization devices; and the biomedical one, mostly related to microvascular researches, disease diagnosis, flow cytometry, and DNA analysis.

In the very most of these microfluidics applications, high-resolution sensing accuracy associated to other features such as compactness and non-invasiveness are highly demanded. Then, the sensing advantages offered by the optoelectronics have been combined to the microfluidics to rise a new cross-disciplinary field of research and technology, sometime labelled as “optofluidics”.

This thesis is inscribed in this context as it deploys the laser sensing techniques based on the Optical Feedback Interferometry (OFI) technology for flowmetry applications. The OFI technology holds very attractive features such as noninvasiveness, non-destructiveness, compactness, robustness, simplicity, low cost, and self-alignment, while offering enough performance in terms of spatial resolution for flow velocity measurements at micro-scale.

More than any optical sensing approach, OFI which is likely to be the most compact interferometric system that can be designed offers possibility to conceive embedded scientific tools in any domain where micro-scale flow channels are involved. The maturity of such sensing approach remains however low as compared to micro Particle Image Velocimetry (μ-PIV) or Laser Doppler Velocimetry (LDV). While these methods are nowadays the accepted standards in industry as well as in research, the OFI sensing scheme must upgrade its performances and reliability so that it will become an alternative solution. These improvements will come from new implementations of the OFI sensor, and properly established processing approaches. The present thesis aims at contributing to the improvement of the OFI performances for microfluidics sensing and proposes new implementations of the sensor.

Besides evaluating innovating implementations of the flowmetry based on the OFI technology and towards an approach of integration as a real-time embedded system, our researches also explore the domain of micro and nanoparticles detection and characterizations. It investigates the limit of particle detection regarding the particle size with the milestone of detection (with velocity measurement) of single nanoparticles with diameter far below half the laser wavelength.

The present thesis manuscript is organized as follows:

The first chapter presents a review of the fluidics sensing techniques based on Doppler optical feedback interferometry using laser diodes. A comparative review of the main flowmetry methods based on the OFI using the Speckle effect is proposed. A comparison of the two approaches leads to focus attention to the Doppler approach on which our researches are based. Then, we introduce the definitions of the scattering regimes that play a major role in the signal processing strategy. Eventually, the optical feedback effect modeling is presented, describing the laser diode output power behavior under feedback interference induced by a multiplicity of single scatterers. Finally, we detail the motivations of this thesis in order to place our choices in the actual scientific context.

The second chapter details the aspects that can affect the OFI signal frequency spectrum morphology and introduces different OFI flow monitoring signal processing methods based on the frequency domain analysis. Three optical configurations are experimentally evaluated, with one focusing lens, a pair of collimating/focusing lenses and the innovating use of a transmission diffraction grating. A detailed comparison of the sensor accuracy in flow velocity measurements from single to multiple scattering regimes is performed with those optical configurations, while for each of them the different signal processing methods are compared.

The third chapter presents an OFI 2D Doppler imager developed during our participation to the European project Diagnoptics dedicated to early skin cancer diagnosis and where the OFI sensor had applications for *ex-vivo* and *in-vivo* flow measurement. We present the technical setup and the experiments performed on an optical table with translation stage scanning systems that were the first steps towards the 2D embedded imager. We describe the dedicated algorithm for a signal processing method that handle the strong signal variations induced by the displacement of the target that are likely to happen in the *in-vivo* configuration. Following that, we present and evaluate our design of a handheld 2D OFI Doppler flow imager that has been realized using a 2-axis beam-steering mirror mounted on a Micro-Electro-Mechanical System (MEMS) in order to take the full advantage of the compactness offered by the OFI sensing scheme. Finally, we present and briefly discuss the results of a clinical study performed for skin cancer diagnosis in the frame of Diagnoptics.

The forth chapter presents a major milestone of our research in OFI flowmetry as it demonstrates the possibility to detect and somehow to characterize micro and nanoparticle flowing in a microchannel. After introducing the definition of the single particle regime, a real-time algorithm for single particle detection and velocimetry is described and evaluated experimentally. Then, the capability of detection of large diameter particles seeded in a watery suspension of smaller ones in higher concentration is experimentally evaluated. Finally, we present and validate experimentally the methods to perform quantification of the size or the concentration of particles of similar nature in watery suspensions at the multiple particle regime. This study is carried out for a large range of dilution and so at different scattering regimes. The impact of the flow rate is also evaluated.

Finally, a general conclusion is given, and a further perspective for potential future works is proposed.

CHAPTER 1: Optical feedback interferometry in fluidics sensing

1.1. Context

Since the advent of the laser, the optical feedback effect due to the laser light interaction with the environment was observed, and it was considered a parasitic and undesired aspect in laser operation affecting both the frequency and amplitude of the laser output. The optical feedback, also called self-mixing effect, happens when part of the light from the laser beam, which is scattered from an external target, is retro-injected into the laser's cavity where it creates interferences.

In 1964, Yeh and Cummins [1] became the pioneers in the development of a technique exploiting the Doppler-Fizeau effect with the laser light to measure liquid's velocity, establishing the principles of the Laser Doppler Velocimetry (LDV). In 1965 Foreman applied this approach to measure gas flow [2], and in 1966 improved the approach from Yeh and Cummins for liquid's [3]. But in 1968, Rudd [4] was the first to take benefit of the laser optical feedback effect in the He-Ne gas laser for Doppler velocimetry.

Some years after, Seko [5] demonstrated the capability of optical memory readout from a rotating compact disc due to the laser power modulation by induced optical feedback in a semiconductor laser. The output power in the rear end of the laser was measured by an external photodetector.

The optical feedback effect had been also detected in a CO_2 laser, and H. Chrunside [6] has shown its Doppler velocimetry capability.

1.1.1. Laser diodes for Doppler optical feedback flowmetry

The optical feedback interferometry (OFI) arises from the interference inside the laser diode cavity between the electromagnetic wave generated by the laser and the one from optical feedback, re-entering the cavity due to the back-scattering or reflection from a distant target. These interferences generate modulations of the amplitude and frequency of the laser output beam, which carries information with physical meanings related to the target. For laser diodes with a built-in package photodiode, the OFI power signal can easily be acquired from the photodiode's current after proper amplification. When the OFI scheme is applied to metrology in fluidics applications, it can be also denominated optical feedback flowmetry. In such context, the amplitude of the OFI signal is proportional to the amount of light reinjected into the laser cavity once backscattered by particles embedded into the fluid that cross the laser beam. The backscattered power is related to the power density of illumination, the scattering cross-section of the particles and their optical properties according to the scattering theory. The "sensing volume" is defined here as the volume where the scatterers are generating measurable contributions to the OFI signal.

In 1980, Lang and Kobayashi [7] presented a model for the semiconductor laser operation under optical feedback that nowadays represents the cornerstone on describing the laser dynamics under feedback.

S. Shinohara [8] was the first (1986) to take advantage of the built-in photodiode in a laser diode to exploit the optical feedback signal for Doppler velocimetry, revealing the capability to measure the angular velocity of a solid rotating target. Following, Jentink [9] also demonstrated similar results.

In 1992, de Mul *et al* [10,11] has applied the OFI technique to measure liquid flow, including in-vivo measurements of blood perfusions from human fingertips. The work of de Mul was based on Bonner and Nossal [12], who have developed a theory relating quasi-elastic light scattering measurements to blood flow in tissue microvasculature. This theory implies that the time decay of the photon autocorrelation function scales proportionally with blood red cell size and inversely with mean translational speed. Analysis of multiple interactions of photons with moving cells indicates the manner in which spectral measurements additionally are sensitive to changes in blood volume. The theoretical model leads to predictions of the way in which photon autocorrelations and photocurrent power spectra depend on variables of the moving particles such as angular scattering cross section, size, number density, and speed distribution.

Bonner and Nossal had shown that the normalized first moment of the spectrum, $<\omega>$, is proportional to the RMS speed of the moving particles $\sqrt{<V>^2}$ as:

$$<\omega>=\frac{\beta\sqrt{<V>^2}}{a\sqrt{12\xi}}f(\bar{m}), \qquad (1.1)$$

where a is the radius of an average spherical scatterer, ξ is an empirical factor which is related to the shape of the red blood cells, and β is an instrumental factor which depends primarily upon the optical coherence of the signal at the detector surface. The variable $\bar{m}$, proportional to red blood cell number density, is the average number of "collisions" which a detected photon makes with a moving cell, the function $f(\bar{m})$ is linear with the tissue blood volume for $\bar{m} \ll 1$ (heterodyne) and varies as the square root of tissue blood volume for $\bar{m} \gg 1$. Considering that, the first moment $<\omega>$ of the signal spectrum $S(\omega)$:

$$<\omega>=\int_{-\infty}^{+\infty}|\omega|S(\omega)\mathrm{d}\omega, \qquad (1.2)$$

has been taken as an indication of relative measurements of blood flow.

de Mul *et* al have shown that for optical feedback flowmetry, in the case of liquid flow or tissue perfusion measurements, the 1st moment is proportional to the average velocity times the number of Doppler scattering particles, while the 2nd order statistical raw moment of the frequency distribution of the Doppler frequencies from OFI signal power spectrum defined as

$$<\omega^2>=\int_{-\infty}^{+\infty}|\omega^2|S(\omega)\mathrm{d}\omega, \qquad (1.3)$$

is proportional to the perfusion squared; and, in cases where the multiple-scattering effects are small, the zeroth moment $< \omega^0 >$ (simply the integrated power spectrum, when integrated for $\omega \neq 0$):

$$< \omega^0 >= \int_{-\infty}^{+\infty} S(\omega) \mathrm{d}\omega, \tag{1.4}$$

is proportional to the number of Doppler scattering particles, and consequently to the particle concentration.

Since then, the potential flowmetry applications of OFI technology to biomedical fields have really started to be considered and explored.

OFI with fiber-coupled laser diode was also evaluated for flowmetry by Slot [13] and Koelink [14-17], members of de Mul's team in the University Hospital of Groningen, especially considering the blood perfusion assessment in vivo and in vitro.

Slot performed in vitro experiments (*Fig. 1*) using a rotating bowl filled with human blood (with a normal hematocrit of about 40%) uncoagulated with heparin. The calibration of the blood velocity was performed by placing the bowl in a position of the rotating disk with a known angular velocity, and the position of the fiber was fixed accordingly. By rotating the bowl, the signals were measured while the blood ran both towards and away from the fiber facet.

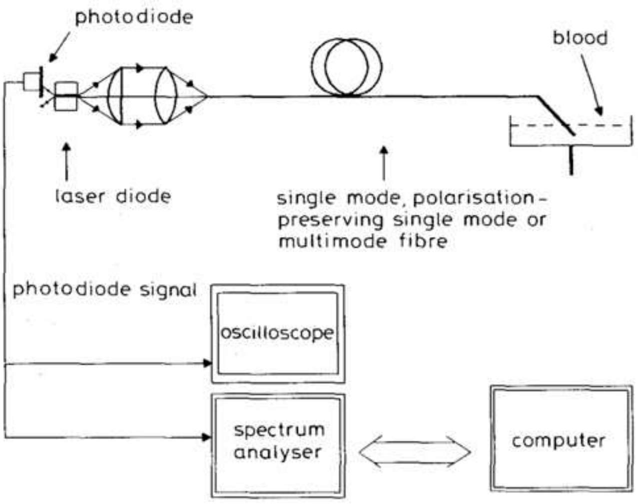

Fig. 1. In vitro experimental setup for self-mixing measurements in a fiber-coupled 780nm diode laser. [13]

Slot has used the first weighted moment of the self-mixing signal spectrum $S(\omega)$:

$$\frac{<\omega>}{<\omega^0>} = \frac{\int_{\omega_1}^{\omega_2} |\omega| S(\omega) \mathrm{d}\omega}{\int_{\omega_1}^{\omega_2} S(\omega) \mathrm{d}\omega}, \qquad (1.5)$$

measured as a function of the blood flow speed in vitro, proving to have a proportional and reproducible relationship with the blood flow velocity after calibration against a properly chosen standard flow. This measurement is shown in *Fig. 2* (with $\omega_1 = 0$ Hz and $\omega_2 = 50$ kHz, because the maximum frequency of the signal spectrum was well below this frequency).

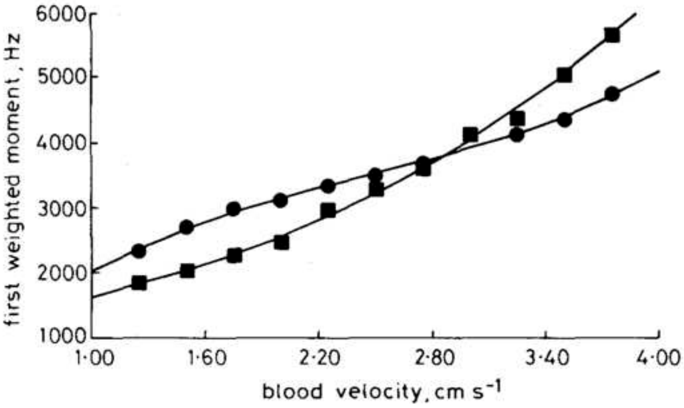

Fig. 2. First (weighted) moment of the self-mixing signal spectrum as a function of the blood velocity with the flow away from fiber facet (•), and flow towards fiber facet (■). [13]

Slot also proved the usability of the fiber-coupled self-mixing technology for blood flow velocimetry in human in vivo experiments. Figure 3 reveals a preliminary self-mixing signal spectrum obtained after introducing the fiber through a Teflon cannula into the left cephalic vein of a healthy volunteer. The fiber was introduced in the direction of the blood flow, so the blood ran away from the fiber facet.

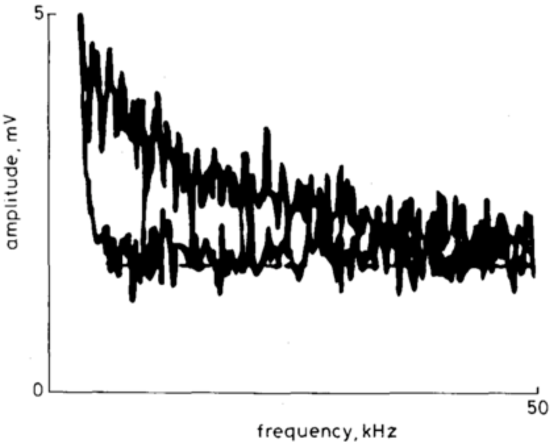

Fig. 3. In vivo measurements of a self-mixing signal spectrum in a human underarm vein. [13]

In *Fig. 3* two spectra can be seen, the upper one corresponds to the spectrum of the free-flowing blood, while the lower is the noise spectrum (biological zero obtained by means of an occlusion with a cuff round in the upper arm).

Slot has also performed an in vivo animal experiment in the same conditions as mentioned in the human one, but now the fiber was introduced into the main artery of the left rear leg of a healthy sheep. The perfusion parameter monitored by a digital signal processor (DSP) was the first unweighted moment $< \omega >$ (with $\omega_1 = 30$ Hz and $\omega_2 = 30$ kHz, limited by the DSP used). The lower limit ω_1 was set to eliminate variations in the signal from non-Doppler shifted light (DC component). Figure 4 shows a real-time recording of the measurements while an occlusion of the lower part of the aorta was performed. The biological zero flow level is clearly visible during the occlusion, and also the overshoot of the blood flow after the occlusion.

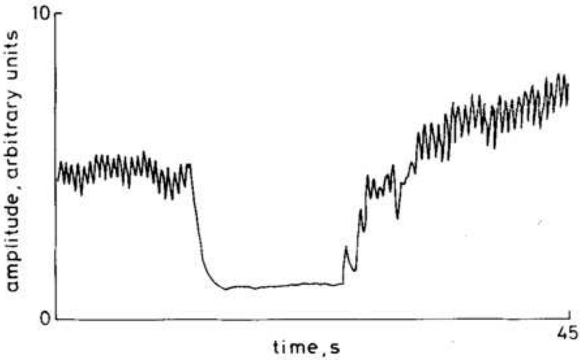

Fig. 4. Recording of the blood flow in the main artery of the left rear leg of a healthy sheep during an occlusion of the lower aorta. The fast fluctuation of the signal is caused by the heartbeat. [13]

Scalise and de Mul in partnership [17, 18] tested the efficiency of this fiber-coupled self-mixing approach to Doppler velocimetry in intra-arterial conditions. In 2001, using the optical glass fiber inserted in the iliac artery of a pig with an endoscopic bask catheter, they obtained less than 9% difference regarding a commercial ultrasound flowmeter [18].

In the domain of in-vivo biomedical applications, Hast [19] has measured the cardiovascular pulse shape from the radial artery with 95.7% of successfully detected pulses from the Doppler spectrogram, in good correlation with the blood pressure signals measured from the middle finger through a commercial equipment. Figure 5 illustrates the measurement system with both techniques.

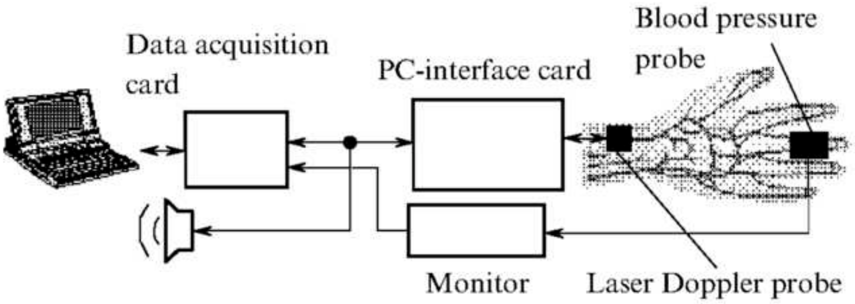

Fig. 5. Block diagram of the measurement system [19].

Figure 6 reveals the good correlation between the detected pulses from blood pressure signal and the Doppler peaks pulses and for a 30-second measurement in a volunteer.

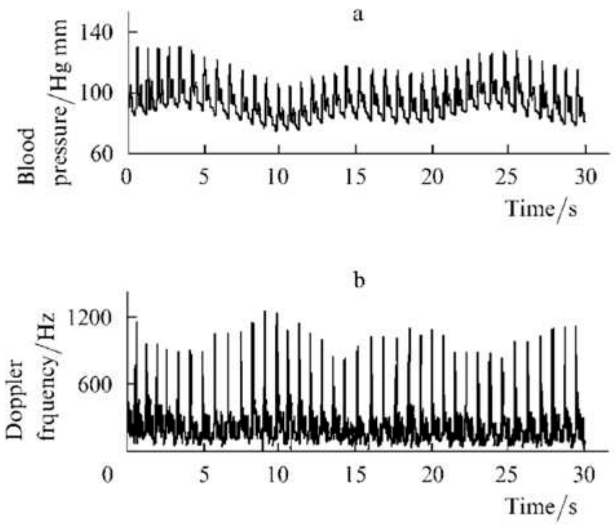

Fig. 6. Blood pressure pulse signal (a) and Doppler spectrogram (b) from a volunteer during a 30-second measurement [19].

Among the possible applications of OFI in the field of chemical engineering, the particle characterization is of major interest. Zakian [21, 22] has shown the possibility to perform particle sizing (using polystyrene monodisperse nanospheres in watery dilute suspensions) at low particle concentration (less than 0.5% in volume). The measurement method was based in diffusion-broadening effect, where the spectral distribution of the scattered light is related to the sphere diameter so that for larger ones the spectral broadening is smaller, while bigger for smaller ones. This effect is explained by the quasi-elastic light-scattering theory, which represents the process of incident frequency broadening due to diffusional dynamic light scattering by small particles; and the spectral line shape is well described by a Lorentzian function with half-width at half-maximum (HWHM) inversely proportional to the radius of the sphere undergoing Brownian motion. In that way, experiments for characterization of the particles size were successfully performed in a diameter range from 20 to 202 nm (*Fig. 7*).

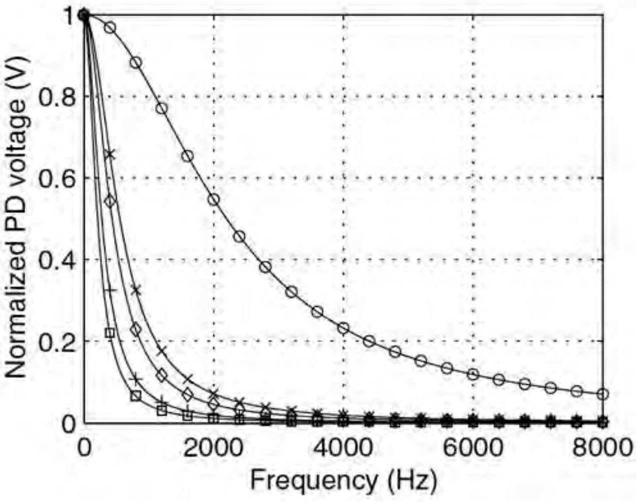

Fig. 7. Collection of Lorentzian fits from spectra (normalized photodiode voltage) of experimental results for different particle diameters. (o 20 nm, × 58 nm, ♦ 70 nm, + 113 nm, and ☐ 202 nm). [21]

Zakian has also performed experiments to measure the maximum flow in a circular tube through layers of scattering media using several spectral signal processing methods based on moments and curve fittings [23]. Milk was used as a phantom model to human blood, due to its high scattering coefficient and low absorption. The purpose was to model the cutaneous microcirculation evaluating the best approach considering the effect of static scattering from skin phantom layers surrounding a 1.5 mm diameter capillary tube. Regarding the signal processing, the result was that an exponential curve fitting in semi-logarithm scale describes well the line shape of the spectrum (*Fig. 8*). The frequency decay constant of the curve (f_0) was used as a flow parameter, as it revealed to be the best to monitor flow under layers up to 1.1 mm in thickness.

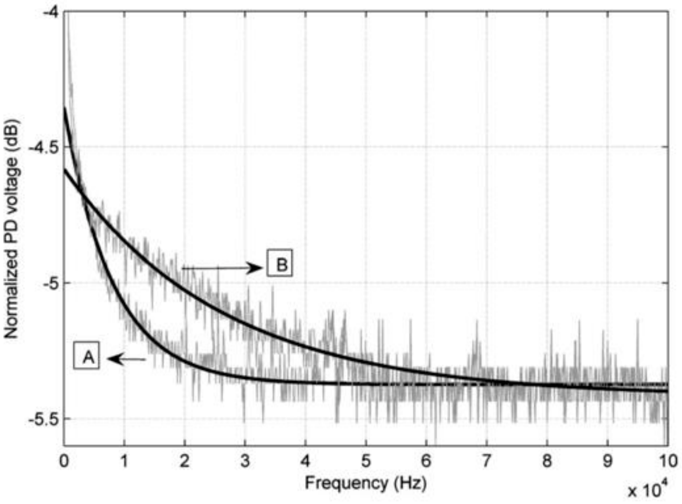

Fig. 8. Example of two spectra sensed with 0.42 mm thick scattering layer at a position showing no flow (graph A) and at a position showing maximum flow (graph B) corresponding to the 50 ml/h. In bold lines we have exponential curves fitted to the graphs. [24]

Following that, he presented a work [24] where the whole OFI sensing system was mounted in a motor driven 2D scanning system in order to image and evaluate the flow map obtained in different flow rates for three types of phantoms in different thicknesses. The *Fig. 9* shows the experimental setup.

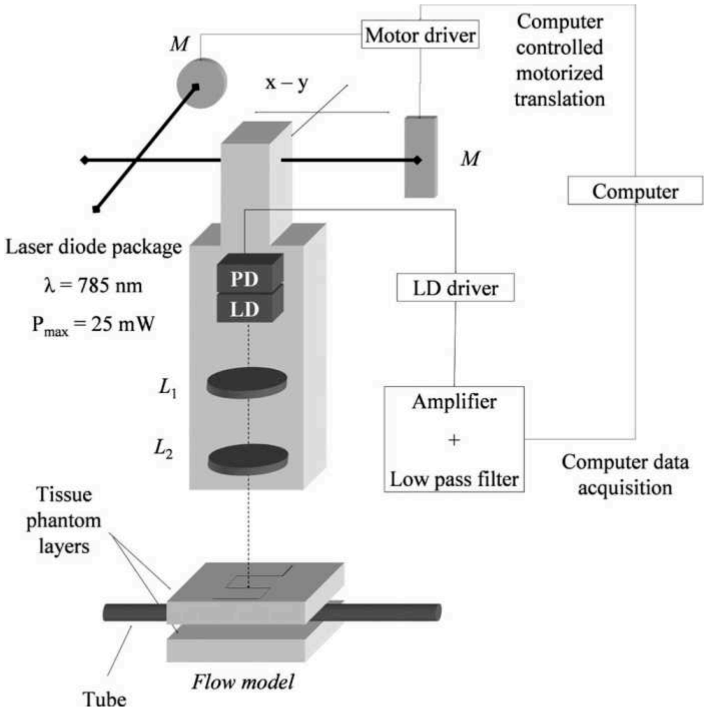

Fig. 9. Experimental setup from [24]. L1: collimating lens, L2: focusing lens, LD: laser diode, PD: photodiode in package.

This was the first published work revealing 2D images of *in-vitro* flow intensity based on OFI system, as it is shown in the *Fig. 10*.

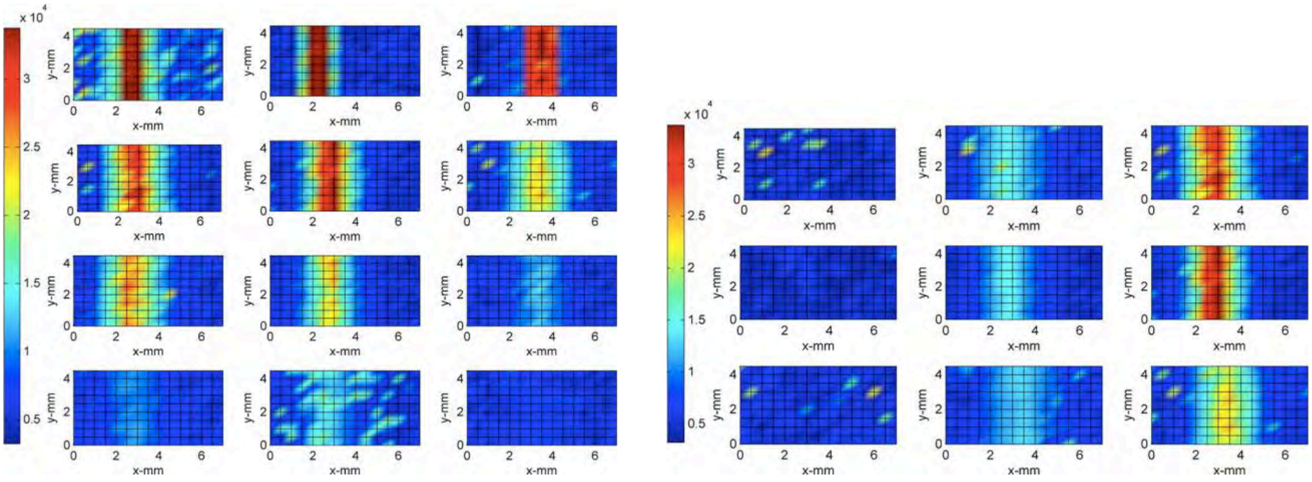

(a)

(b)

Fig. 10. Flow map (f_0 color coded) for three different kinds (columns) of phantom tissue layers (a) with, from top to bottom rows: no layer employed; 0.42 mm; 0.70 mm; and 1.19 mm thick layers. (b) under, from left to right: no flow; 25ml/h and 50ml/h flow rates, with 0.42mm thick layer.

Although the ability to employ OFI sensing scheme for 2D Doppler imaging was demonstrated, the scanning time was considerably long. Even if the acquisitions for each pixel took around 180 ms, the time to change from one position to the next one was around 10s. So wider the scanning area and higher the image resolution, bigger will be the number of pixels and consequently the total scanning time.

With the advent of vertical-cavity surface-emitting laser (VCSEL), the team from the University of Queensland was the first to use a single 850-nm VCSEL laser in a single lens configuration to measure the liquid flow rate utilizing the variation in junction voltage of the laser due to optical feedback interference, as presented by Tucker *et al.* [25]. Despite exhibiting a lower signal-to-noise ratio as compared to the flow rate measurements using an integrated photodiode (PD), both detection methods produced comparable results (*Fig. 11b*) using the cut-off frequency technique (the empirical criterion of -3dB threshold regarding the plateau is depicted in *Fig. 11a*, for the PD spectrum at a slow flow rate). This is an empirical technique, that can be used in spectra which line shape presents a plateau, to estimate the maximum Doppler frequency corresponding theoretically to the maximum flow velocity ($V_{\max}$) according:

$$f_{3\mathrm{dB}} = \frac{2nV_{\max}\cos\theta}{\lambda}, \qquad (1.6)$$

where θ is the angle between the laser beam axis and the scatter velocity vector; n is the refractive index of the fluid; and λ is the wavelength of the laser.

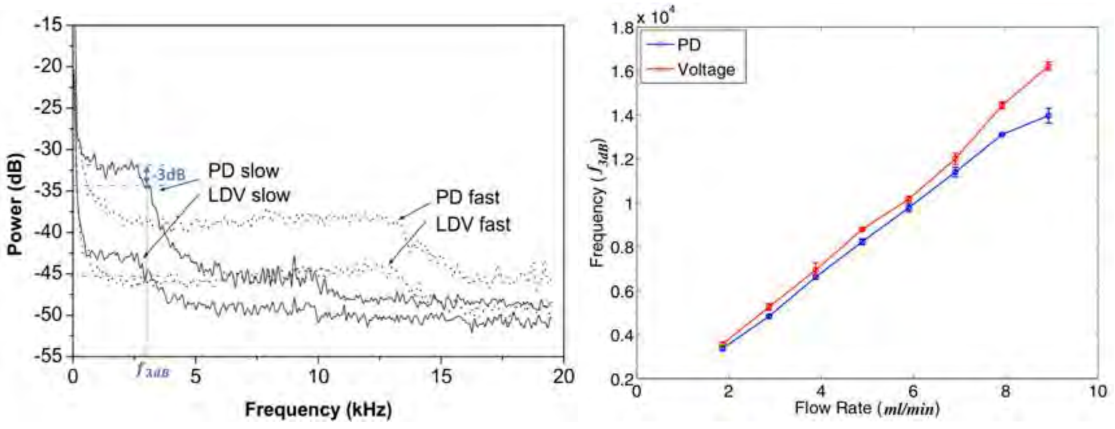

(a) (b)

Fig. 11. (a) Frequency spectra obtained for both schemes at a slow and a fast flow rates: by the junction voltage of the laser diode (LDV) and by the photodetector's current through a transimpedance amplifier (PD). (b) Curves corresponding to the maximum Doppler frequency estimated by the -3 dB cut-off frequency from the spectra for both schemes at different flow rates (2-9 ml/min). [adapted from 25]

As the wide active area of the monitoring photodiode in a VCSEL (*Fig. 12*) makes it vulnerable to optical crosstalk, what is undesired for a proper OFI sensing, this new approach of detection by the laser junction voltage could benefit OFI applications based on VCSEL arrays, becoming cost effectively to manufacture a monolithic array of lasers [26].

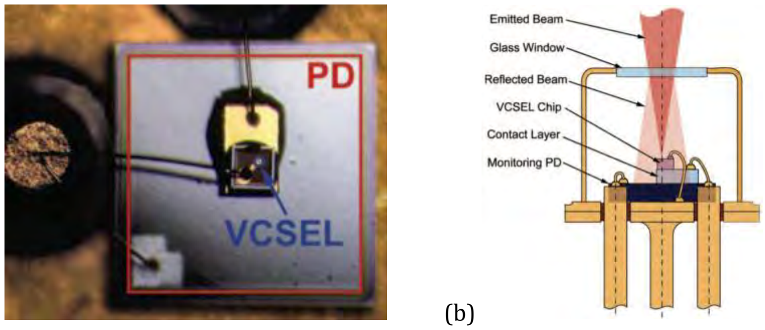

(a) (b)

Fig. 12. (a) Microscope image of VCSEL and PD inside the TO-46 package. (b) component layout of the TO-46 package. [26]

In order to design an imaging system to obtain the velocity flow profile of a flow channel, Tucker *et al.* used eight individual 850-nm VCSELs with integrated PD arranged in a linear array. For each one, a single-lens configuration was provided by a block holding eight aspheric lens (*Fig. 13a*). Each VCSEL in the array was operated intermittently, and the first weighted moment method (with $\omega_1 =$ 75 Hz, which was above the low frequency noise; and $\omega_2 =$ 1.45 kHz, which is the point where the spectrum decays to 3 dB above the noise floor for the smallest measured velocity) was used to compute the average flow velocity from the output power spectra.

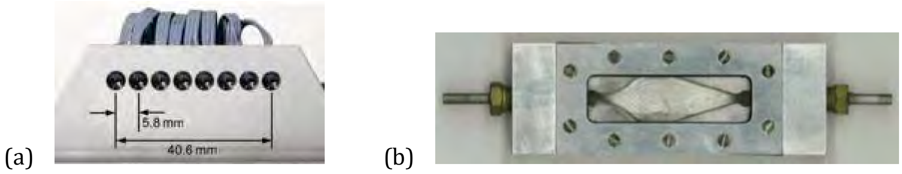

Fig. 13. (a) Prototype of the linear array of eight VCSELs individually mounted in single lens configuration. (b) photograph of the custom-made diverging-converging planar flow channel used for the experimental setup. [26]

The beams were aligned along the centerline of the flow channel (*Fig. 13b*) starting from the entrance of the diverging section to the exit of the converging section. The dimensions of the channel allowed for six beams to be aligned along the centerline of the flow channel. Figure 14a shows the calibration relating the first weighted moment measurement from a single VCSEL in the array at different inlet flow rates. Figure 14b reveals the measured centerline velocity profile for the flow channel.

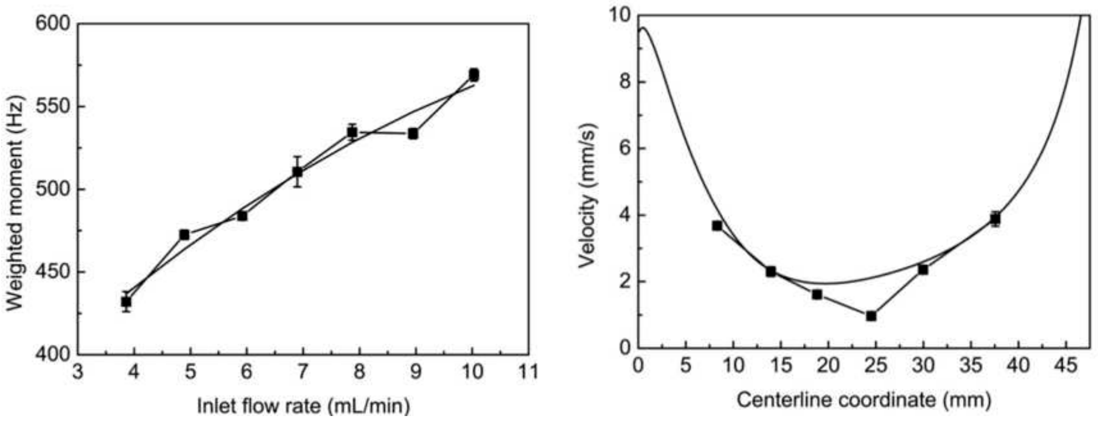

(a) (b)

Fig. 14. (a) First weighted moment (squares) for a single channel of the VCSEL array at different inlet flow rates fitted to a quadratic function. (b) Actual (solid curve), computed by 2D flow simulation with FLUENT software, versus measured (squares) centerline velocity profile for flow channel. [26]

Although this implementation requires a switching or multiplexing circuitry for a horizontal scanning, it represents an improvement on frame rate compared to a single point scanning. For a 2D profile of the channel, it requires still a translation stage to shift vertically the channel's position.

Lim *et al.* [27], also member of the team from the University of Queensland, has shown a fluid-flow imaging system based on a monolithic linear array of twelve 850-nm VCSELs that uses the laser junction voltage detection technique, also including a 2D velocity profile of the flow channel (the same one used by Tucker, *Fig. 15b*) obtained in a single sweep.

He has set a double-lens optical configuration to increase the imaging resolution. As the laser pitch of the array is now much smaller (250 μm, versus 5.08 mm for Tucker's one), then, instead of using individual small lens, he has used only two lenses with active area big enough to cover whole laser array (*Fig. 15a*).

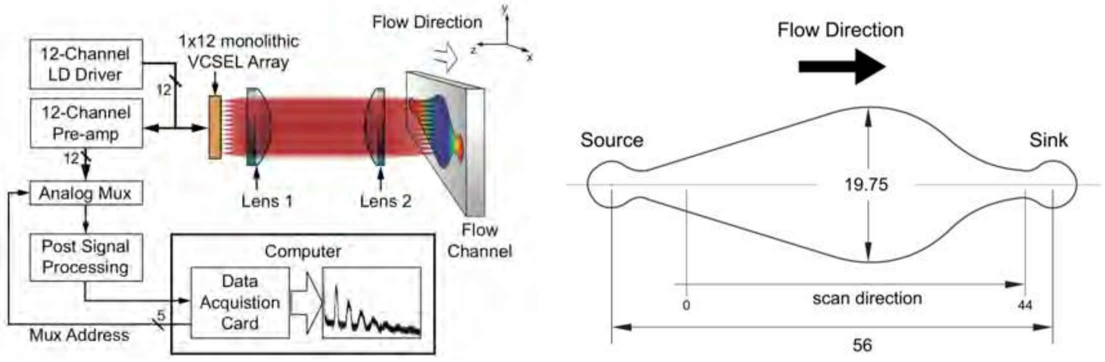

(a) (b)

Fig. 15. (a) Schematic diagram of the flow-channel measurement system. (b) Mechanical drawing of the custom-made flow channel (56 x 19.75 mm). The scanning distance corresponded to 43 mm across the centerline. [27]

A watery suspension made with very diluted milk (2%) was pumped into the flow channel. As the computed spectra presented always a Doppler peak corresponding to the maximum velocity (V_{max}), a curve fitting was performed to extract the peak frequency. Then, the velocity corresponding to each pixel could be calculated by

$$V_{\mathrm{max}} = \frac{2nf_{\mathrm{m}}\cos\theta}{\lambda}, \qquad (1.7)$$

where θ is the angle between the laser beam axis and the scatter velocity vector (80°, for this experimental setup); λ is the wavelength of the laser (850 nm); n is the refractive index of the fluid (≈1.33 for 2% milk at 850 nm); and f_{m} is the Doppler frequency peak extracted from the fitted curve of the spectrum.

Figure 16 shows the image of velocity distribution within the flow channel with an inlet flow of 15ml/min. The total image height of the 12-channel array projected onto the flow channel is 5.5 mm and the height of the flow channel window is 17.6 mm. Therefore, three consecutive horizontal scans were carried out to acquire the velocity distribution image. The horizontal step-size in the translating stage was of 1 mm.

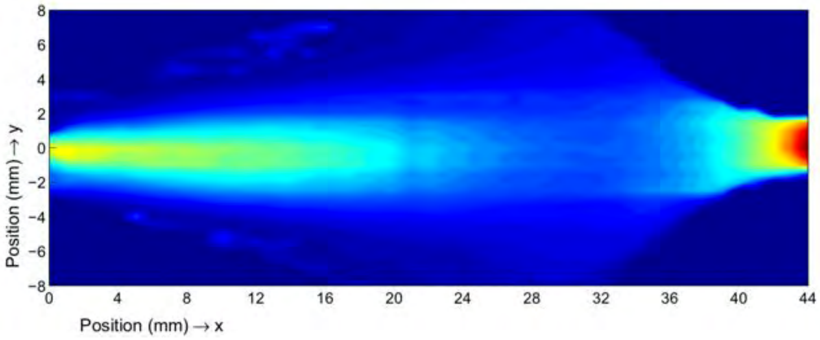

Fig. 16. 2D distribution of the flow velocity profile across the flow channel for an inlet flow of 15ml/min. The velocities were calculated from the measured Doppler peak frequency by *Eq. 1.7*. Pseudo colors ranging from zero (deep blue) to 3.5 cm/s (deep red). [27]

In order to propose the combination of a VCSEL array with a motorized translating stage offering the potential to enhance the rapidity of the scanning system while obtaining a 2D Doppler image for microfluidics applications, Kliese *et al.* [28], another member of the team at Queensland University, has validated his idea using a 665-nm VCSEL in a single lens configuration to obtain with the laser junction voltage technique an image of the flow (*Fig. 17*) in a 100μm square cross section channel. A watery suspension made with 10% diluted milk was pumped at a constant flow rate of 5 μL/min. The Doppler angle was of 80°, formed between the laser axis and the microchannel.

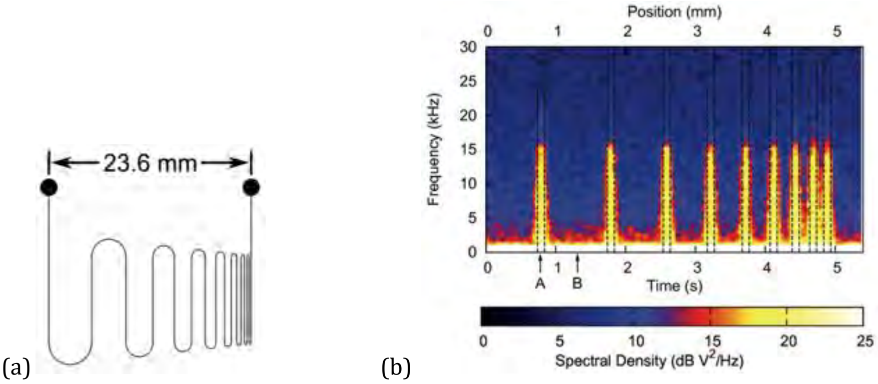

Fig. 17. (a) Microfluidic channel pattern. (b) Spectrogram obtained from the OFI signal as the laser was scanned at a rate of 1 mm/s over the centerline of the right portion of the microchannel (the broken lines indicate the channel positions). [28]

Taking advantage, for the first time, of the blue emitting (GaN 405 nm) laser diode for OFI sensing, Kliese [29] had also shown that although the blue laser has poorer noise performances than the near-IR laser, its shorter wavelength enables to accurately measure very low flow rates down to 26 µm/s in a 1.81mm diameter tube, while pumping a watery suspension made of 3.06 µm polystyrene microspheres at so low particle concentration that the refractive index of the medium was equivalent to the one of the water. The Doppler angle was of 75° between the laser axis and the flow tube.

Figure 18 indicates that the 783-nm IR laser was unable to measure the lowest flow rate of 25.9 µm/s.

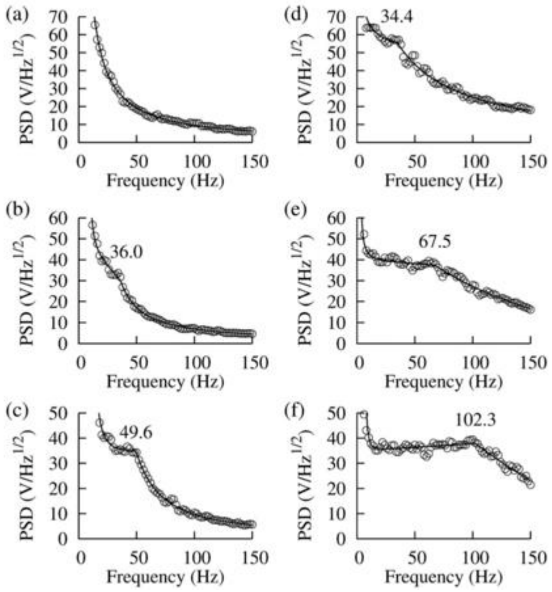

Fig. 18. Averaged OFI spectra for the flow experiments. Results (a)–(c) are for the IR laser, and results (d)–(f) are for the blue laser. The corner frequency for each of the signals is indicated. The maximum flow rate for the results in (a) and (d) was 25.9 µm/s, the rate for (b) and (e) was 51.8 µm/s, and the rate for (c) and (f) was 77.7 µm/s. [29]

On the context of the way forward the OFI sensing integration into the microfluidics system for flowmetry applications, Nikolić *et al.* [30], from the same team at the University of Queensland, integrated an optical fiber directly into a polydimethylsiloxane (PDMS) microfluidic circuit to couple the laser into a 720-µm microchannel (*Fig. 19*), instead of using bulk free-space optics. The laser light source (850nm VCSEL) was coupled into the distal end of the fiber embedded in the optofluidic circuit. Obtaining the OFI signal directly from the junction voltage of the VCSEL, this flow sensor has shown to exhibit feasibility over a range of fluid velocities from 0.5 to 60 mm/s for four bovine milk concentrations: 100%; and 10% w/w, 1% w/w, and 0.2% w/w diluted in water.

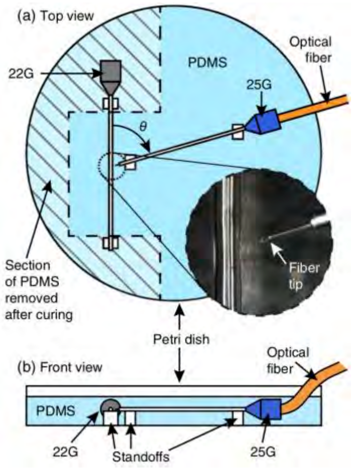

Fig. 19. Device manufacture showing (a) top view with inset showing photograph of the finished device and (b) front view. An optical fiber was stripped and cleaved at one end and glued into a 25G dispensing needle tip for rigidity. This needle tip and a 22G tip were arranged in a Petri dish with standoffs and PDMS was poured to cover both needles. After PDMS curing, the hatched section of PDMS was removed and the 22G tip was pulled out, leaving a microchannel. The angle between the fiber and the channel, θ, was approximately 74°. [30]

1.1.2. Velocity flow profile

Nikolić *et al.* [31], in partnership with Campagnolo *et al.* from the LAAS-OSE team of the University of Toulouse, has also used the 665-nm VCSEL (with the laser junction voltage detection method) associated to a computer-controlled 3-axis motorized translation stage to place the center of the microchannel in the focal plane, and move it across the laser sensing volume for scanning. For that, they had improved the spatial sensing resolution by using a double lens configuration (*Fig. 20a*) what reduces the sensing volume, to accurately reconstruct, by the first time, the velocity profile (*Fig. 20b*) of a laminar flow in a 320μm diameter microchannel with less than 2% of standard deviation.

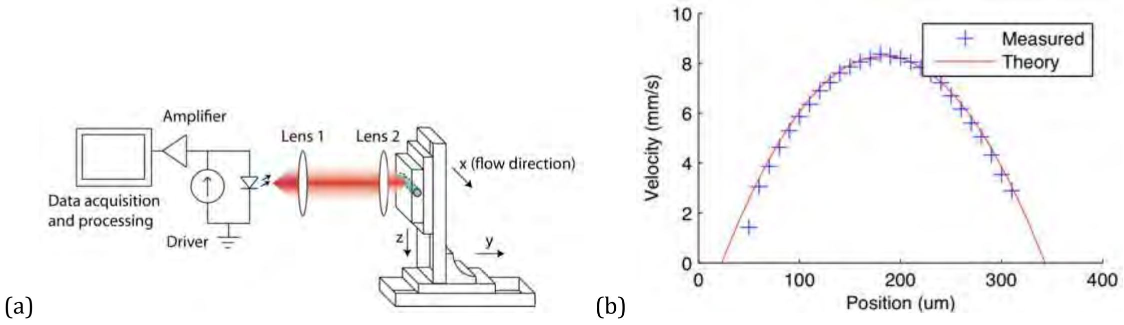

Fig. 20. (a) Diagram of the experimental setup. (b) Theoretical (by Eq. 1.7, with θ=76°) and experimental (10µm step resolution) flow profiles. [31]

Considering the context of potential biomedical application for OFI flowmetry in microvascular research, Campagnolo *et al.* [32], using the same VCSEL setup (now, with the optical head mounted in the translation stage, instead of the flow channel) demonstrated the feasibility of OFI flowmetry in a small rectangular polydimethylsiloxane (PDMS) microchannel of only 20 µm height, 100 µm wide (*Fig. 21a*). The measured flow profile was validated by the profile measured using a dual-slit (DS) technique (*Fig. 21b*). The fluid used was a 0.1% particle suspension of 4 µm latex microsphere, pumped at a low flow rate of 0.1 to 1 µL/min. The maximal flow velocity was measured by the 3dB cut-off frequency method.

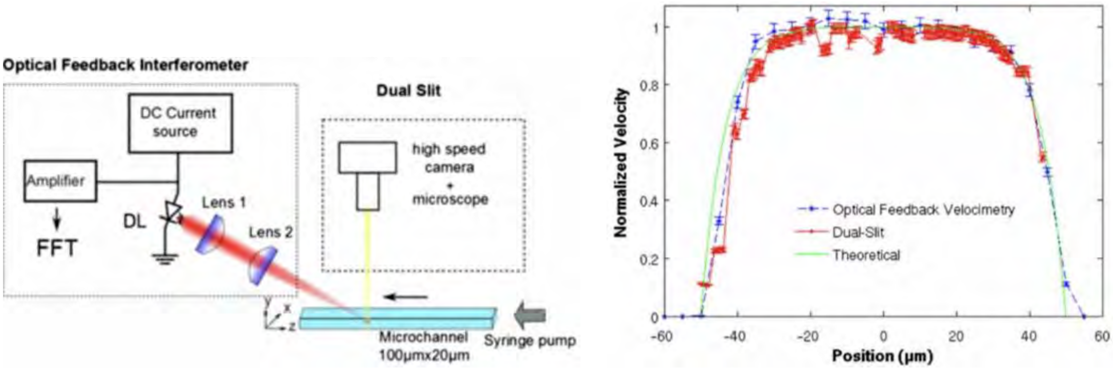

(a) (b)

Fig. 21. (a) Diagram of the experimental setups: OFI (left) and DS (right). (b) Normalized profiles of maximal velocity measured in a rectangular PDMS channel (100 x 20 µm), using OFI (blue dashed curve) and DS (red plotted curve. The theoretical curve (solid green) is added for reference. [32]

Quotb [33] has demonstrated the feasibility to use an OFI sensor (a 785nm laser diode in a single-lens configuration) for flow characterization inside ex-vivo rat aorta (diameter: ≈850µm). The OFI signal was exploited from the built-in photodiode's (PD) current through a transimpedance amplifier. In validation, a fluid composed by a ratio of 10:1 of phosphate buffered solution and milk was pumped in constant flow rate, and a raster 2D Doppler image (25x15, with a pixel resolution of 100 µm) was obtained as illustrated in *Fig. 22*.

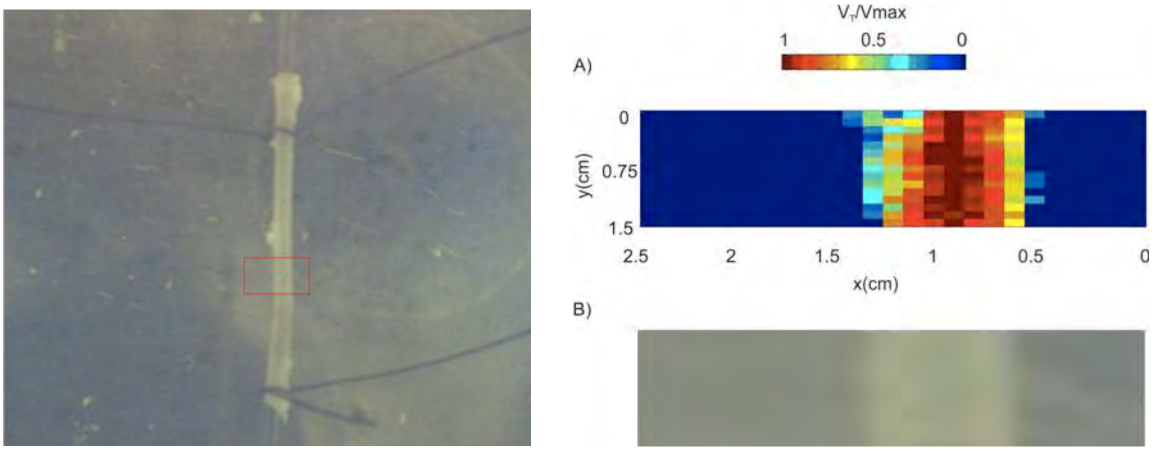

(a) (b)

Fig. 22. (a) Cannulated rat aorta: red rectangle corresponds to OFI scanned area. (b) Rat aorta imaged: A) 2D raster Doppler image of the flow velocity (V_T) normalized by the maximum flow velocity V_{max}, captured by the OFI sensor in a 3-axis translation stage. The pixel intensity corresponds to the maximum Doppler peak. B) raw image of the scanning zone captured by a camera. [33]

Ramirez Miquet [34] has presented an OFI flowmetry sensing using a 785nm laser diode with built-in PD (mounted with single-lens) in a millifluidic configuration for real-time assessment and characterization of non-steady flows, with in-situ calculation of the zeroth order moment of the OFI signal obtained from the PD, allowing to easily evaluate the related periodicity of non-steady flows of a peristaltic pump. This calculation consists on the integration of the amplitude differences in the spectrum (in dB) of a set of OFI signals with and without flow. This process is expressed by

$$M_f = \sum_{f_{min}=0}^{f_{max}=F_s/2} \left| OFI_{flow} - OFI_{no\ flow} \right|$$

where f is the frequency in the spectrum which ranges from 0 to half the sampling frequency (F_s) of the acquisition system, $OFI_{no\ flow}$ is the obtained spectrum when the fluid does not move, OFI_{flow} is the spectrum when the fluid is moving and Mf is a parameter related to the flow variations. Figure 23 reveals the linear trend of relationship between the flow rate and M_f.

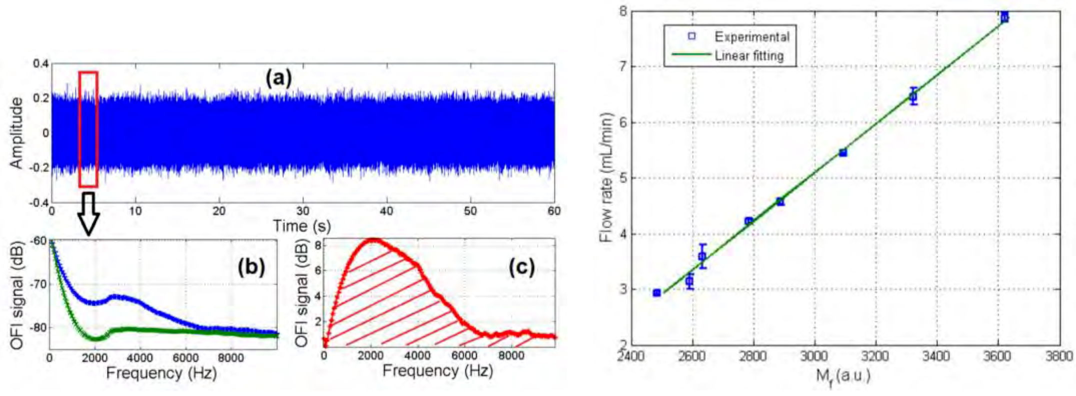

(A) (B)

Fig. 23. (A) Overview of proposed method performing over a continuously acquired time domain OFI signal (a). Spectrums of OFI_{flow} and $OFI_{no\ flow}$ (b) and their difference (c). (B) Linear relationship of Flow rate versus M_f. [34]

Ramirez Miquet [35], using the 785 nm laser diode (with built-in PD) in a single-lens configuration (*Fig. 24a*), has also demonstrated measurement of the flow profile of two viscous immiscible fluids (oil-water) in good agreement with the expected theoretical profile (*Fig. 24b*). This represents a step forward for the OFI sensing in the field of interface flow characterization at complex phase interactions, like on the hydrodynamics of droplets or dispersed flows.

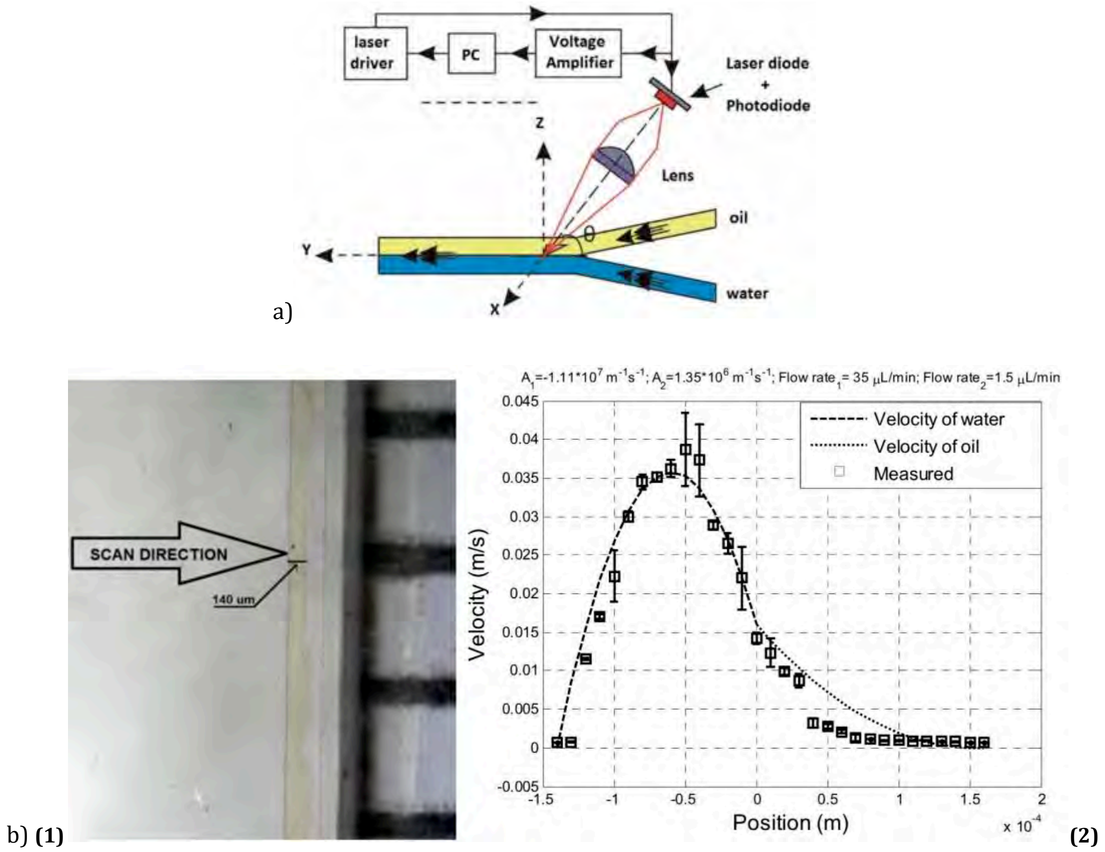

Fig. 24. a) Experimental setup (optical head mounted over a computer-driven 3D-stage) with θ=80°. b) **(1)** Volume occupied by each fluid (oil-water). Betadine was added in water to enhance the contrast between both fluids. **(2)** Both measured (squares with error bars for three measured maximal velocity profiles) and simulated (dashed and dotted lines) reconstructed profiles. [35]

Zhao [36] has presented a new numerical modeling based in Monte Carlo ray-tracing simulation for OFI flowmetry spectrum reproduction, in order to study the optical effect on the OFI signal due to the micro-scale geometry of the channel. This model has permitted the prediction of a second Doppler peak in the spectra for a 100 μm square cross section SU-8 channel, while using a 670nm VCSEL with double-lens configuration. At experimental level, the OFI signal acquired from the built-in photodiode presented a second Doppler peak (*Fig. 25*), as predicted by the model, due to the reflection of the forward scattering by the rear interface of the micro-rector. The experimental validations were performed using a polystyrene spheres suspension at low concentration (5 x 10^6 spheres per mL) pumped at constant flow rate (from 5 μL/min to 50 μL/min).

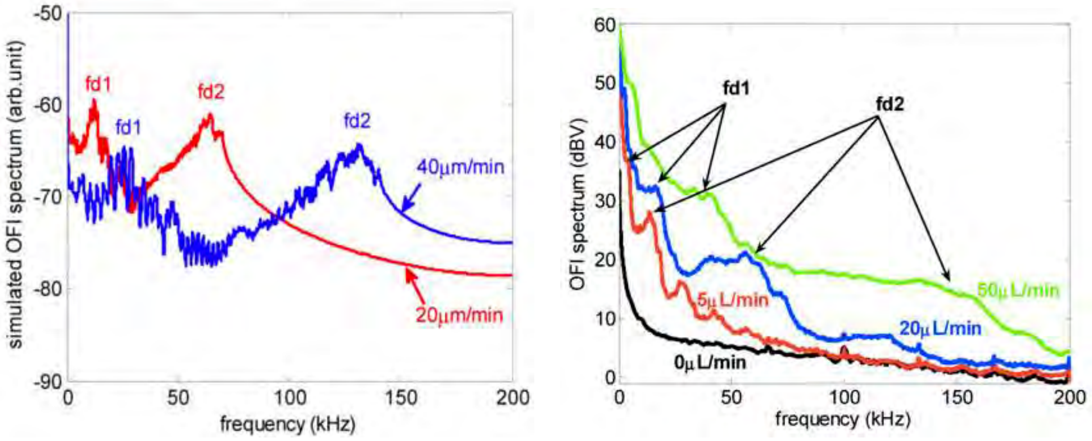

(a) (b)

Fig. 25. a) Simulated OFI power spectra obtained for different flow rates (Q = 20 µL/min in red and 40 µL/min in blue). Two Doppler peaks (fd) are well denoted, where fd1 arises from the forward scattered light reflection on the rear interface, and fd2 corresponds to the maximum velocity. b) Measured OFI spectra at following flow rates: 0 µL/min (black), 5 µL/min (red), 20 µL/min (blue) and 50µL/min (green). [36]

A. Alexandrova [37] has used an OFI sensor to measure fluid velocity of watery suspensions of 1 µm-diameter Titanium Dioxide (TiO_2) spheres in order to evaluate the effect of the seeding particle concentration and also of the fluid flow rate in the measurements. The sensor revealed an accuracy better than 10% for liquid flow speeds up to 1.5 m/s with scattering particle concentration ranging between 0.03%-0.8% w/w. While keeping the same particle concentration, it has been demonstrated that increasing the pumping speed reduces the amplitude of the spectral Doppler peak, broadening the frequency distribution as well. The *Fig. 26a* shows the computed spectra of the OFI signal at a constant liquid velocity of 1.2 m/s, and varying the amount of seeded particles in the pumped suspension. The *Fig. 26b* reveals the related variations of the amplitude and frequency of the spectral Doppler peak. The amplitude of the spectral Doppler peak decreases steadily with decreasing concentration.

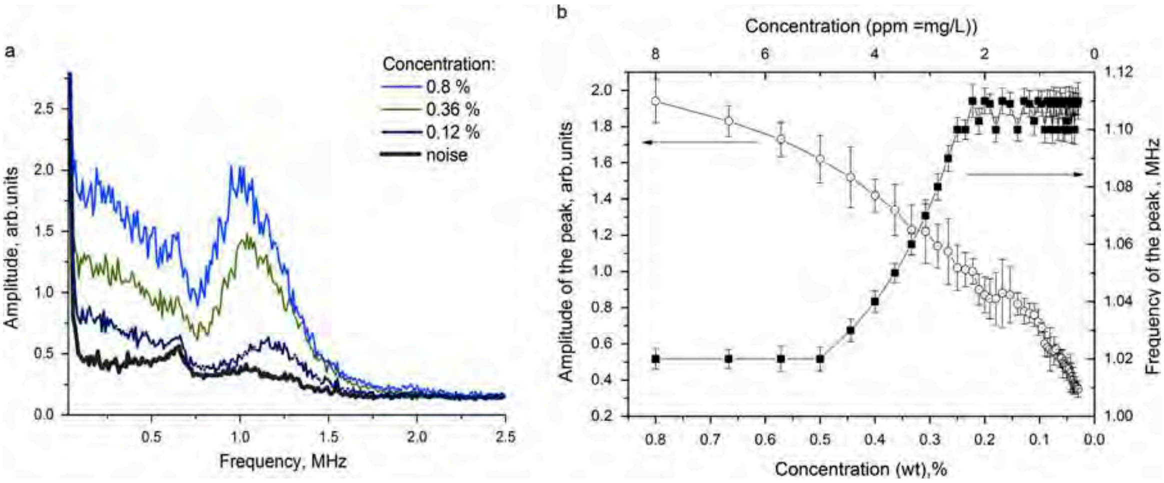

Fig. 26. (a) Computed spectra in experiments with different particle concentrations in water: 0.8%, 0.36% ans 0.12%. (b) Experimental dependence, after subtracting the noise, of the amplitude of the spectrum peak (left axis), and the Doppler peak frequency (right axis), on the particle concentration. [37]

F. Marrazzi [38] has demonstrated that a proper conditioning of the OFI signal related to in-vivo perfusion measurements from human tissues can overcome the usual issue of quantization errors. This can be obtained by first separating the DC part from AC part of the OFI signal, then amplifying only the AC one, and finally recombining both signals before digitalization. This leads to less noisy signal with a smaller standard deviation and thus a higher sensitivity to physiological changes of the perfusion parameters. The approach was validated with in-vivo measurements over the fundus of human eye, successfully presenting a smaller standard deviation than a commercial Laser Doppler flowmeter device.

The Doppler frequency shift approach has been the mostly used, but it is not the unique way to sense flows with the OFI technology.

1.1.3. Speckle approach in OFI

As well as the Doppler approach, the time-varying speckle can be used to measure velocities by OFI, especially for measurement of line-of-sight velocities (velocity projection along the optical axis). [39, 40].

The OFI speckle velocimetry methods are based on the time domain statistics of the dynamic speckle patterns. These methods are usually whether based on counting speckle pulses (generated each time the OFI signal intensity passes above a defined threshold) over the measurement time, in order to obtain a mean speckle frequency in relation with the target velocity; or on the autocorrelation [41] of the OFI signal, as the autocorrelation time (τ_c) of the speckle intensity fluctuations is related to the fluid velocity.

Using a 785 nm laser diode, Ozdemir [42, 43] has shown the capability to apply the OFI speckle sensing approach in flowmetry applications to assess in-vivo blood perfusion (up to 150 mm/s) using both methods, after validations in-vitro (*Fig. 27*). The autocorrelation method has revealed to be better than counting method to discriminate among three blood flow conditions (normal, constricted and enhanced) for in-vivo measurements performed over the skin (along visible blood vessels of the wrist) of healthy volunteers.

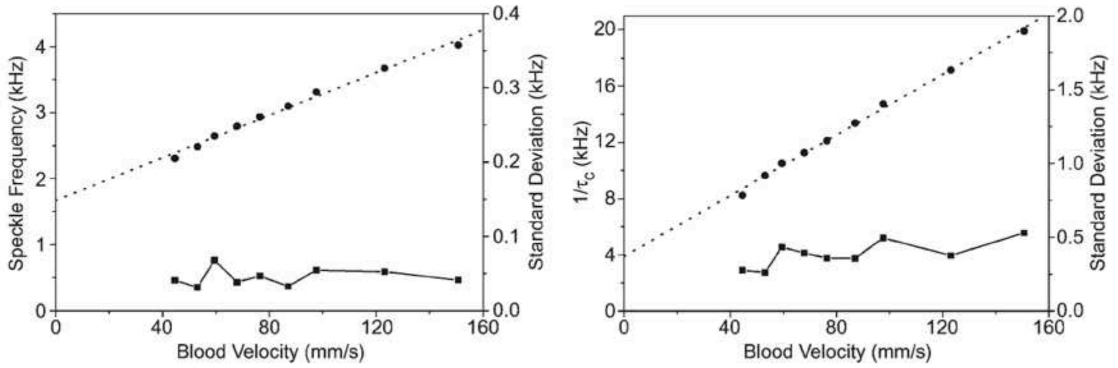

Fig. 27. Results from in-vitro mesurements of 1% blood suspension perfusion in a 2-mm inner diameter transparent capillary by an OFI speckle velocimeter using counting (left graph) and autocorrelation (right graph) methods. The dotted lines represent the best linear fit with 99% correlation to the experimental data. The squares correspond to the measurements standard deviations. [43]

Figueiras [44] has applied an invasive OFI microprobe (with a pigtailed laser diode) directly over the rat brain tissue in order to measure blood perfusion variations in the hippocampus region promoted by intraperitoneal injection of sodium nitrite. The discriminations of the perfusion variations were successfully detected by four signal processing statistical methods, based on time-varying speckle (counting and autocorrelation methods) and spectral based (raw 0th and 1st order moments). The validations, were performed in different animals using two laser wavelengths (785 and 1308 nm) inside the diagnostic window range (600-1600 nm), and the results were successfully compared to a commercial laser Doppler flowmeter device.

In their study Ozdemir *et al.* have highlighted the fact that the OFI speckle detected signal is very dependent on the back-coupled speckle field; the beam spot size [45] on the scatterer; and on the precise adjustment and control of the distance between the laser front facet and the target scatterer, in order to properly resolve the average speckle size back into the laser facet.

Also, the relative velocity measurements based on the autocorrelation method vary accordingly the integration time (Δt) considered [43] in the time-varying speckle computation by autocorrelation. In same way, for the ones based on the counting method, the threshold setting to trigger the pulse train can induce measurement variations affecting the velocity sensing accuracy.

It’s pertinent to mention that the modulation of the laser light by the retro-injected backscattered light from external artefacts and from the target surfaces can induce intensity fluctuations in the speckle signal leading to an offset value in both methods, even at no flow condition, and that such offset varies accordingly to the scattering properties of these artefacts [41].

For these reasons the OFI speckle approach requires considerable calibration to overcome these drawbacks in order to achieve an absolute velocity measurement. But under certain conditions, like for most in-vivo situations, calibrations are unfeasible.

Still on the sensing context of the speckle approach, we should highlight that there is also a strong dependence on the angle (θ) between the laser beam and the vector velocity of the moving target under measurement. The mechanical setup must be set to impose ideally θ = 90° to obtain the best of the speckle effect. When θ ≅ 90°, the intensity fluctuations induced by the speckle effect are predominant, while the Doppler shift tends to zero. In that way, the speckle effect will dominate the dynamics of the laser diode under optical feedback, and the output power modulation will become random [41]. Such random variations in the OFI signal (exploited from the built-in photodiode's current) will be detected as speckle signal, and a time-varying speckle signal can be acquired and computed by autocorrelation while a target moves across the laser sensing volume to measure the related target's velocity.

Although the laser speckle has been studied since the sixties together with the advent of the laser itself, it's only since a few years that the speckle sensing potential has started to be explored on laser diodes under optical feedback. Much of the speckle statistical properties still needs to be understood, especially in the fluidics field. For example, to the best of our knowledge, there isn't yet published work on the evaluation of the impact of the scatterer concentration, with the known signal processing methods.

1.2. The scattering regimes

In the context of a diode laser under optical feedback due to the interaction of the laser beam with flowing particles embedded in the a fluid, the particle concentration is an important element that affects the laser behavior.

When the particle concentration is low enough in a way that adjacent particles are sufficiently away from each other, a single or independent scattering can occur. Then, each photon is scattered by only one translating particle at the time. In other words, such photon suffers a unique Doppler shift before re-entering the laser cavity. In that way, each particle owing a unique velocity is considered as an elementary scattering unit in a macroscopic medium composed of randomly positioned discrete particles.

In order to validate the single scattering hypothesis, theoretical studies [46] have been performed in order to evaluate and identify a clear rule for the definition of the single scattering regime. According to Quirantes [47] and Sudo [48], the effect of interactions between particles near to each other is mostly dependent on the particle size and concentration, showing that the single scattering regime is achieved as long as an interparticle separation equal to four times the particle radii for Quirantes, while for Sudo, the effect of particle interactions becomes significant when the solid volume fraction in a particle suspension is greater than 5%, or the average inter-particle spacing is smaller than the laser wavelength.

In the case of high densities of flowing particles, the photons may be scattered (and thus Doppler shifted) several times by different scatterers before the retro-injection in the laser cavity. This condition is known as the multiple scattering regime, and the resulting OFI output power signal corresponds to a distribution of Doppler shifts, correlated to the backscattering from a plurality of scatterers with multiple Doppler shifts at different relative velocities and different incident angles.

1.3. Laser Diode OFI theory for a multiplicity of single scatterers

Considering the context of a diode laser under optical feedback due to the interaction of the laser beam with flowing particles embedded in a fluid, we recall here the established equations that model the laser diode operation behavior under the feedback condition caused by mutiple scatters.

There are two classical ways to describe the laser diode behavior under optical feedback: the 3-mirror cavity model and the Lang-Kobayash model [49].

In the first one, where the target works as the third mirror, a 2-mirror equivalent cavity can be obtained, from which the laser rate equations can be deduced. So under single scattering regime, summing up all the back-scatterred contributions from each particle as target, we can finally obtain the laser power output under optical feedback.

In the second approach, the optical feedback can be seen as a perturbation of the free running laser mode, and so an extra term can be directly added to the electrical field or photon rate equation representing the contribution of the back-scattered light.

A comparison between both approaches has been considered [50], and it has been demonstrated that although the cavity method is a more exact description, the Lang-Kobayashi model is well suited for low feedback levels and quasi-steady state analysis of the phenomenon.

In the case of microfluidic sensing from particle suspensions in single scattering regime the feedback level is always very low, what justify the use of Lang-Kobayashi method, as proposed by Zakian [51, 52], later reviewed and validated by R. Miquet [53], as we follow here.

The Lang-Kobayashi rate equation of the electric field E propagating inside the laser cavity and that is subject to an external perturbation is here used as base for the modeling approach:

$$\frac{d}{dt}[E(t)\exp(j\omega t)] = \left[j\omega_N + \frac{1}{2}\Gamma G(N - N_{\mathrm{tr}})\right] E(t)\exp(j\omega t) + E_f(t) \tag{1.8}$$

where ω is the laser mode angular frequency; ω_N is the cavity mode angular frequency ($\omega_N = \mathrm{k\pi c}/n_c L_c$ with k an integer; L_c the laser cavity length and n_c the refractive index); Γ stands for the laser mode confinement factor; G is the stimulated emission gain; N is the carrier density; N_{tr} is the carrier density at transparency; and $E_f(t)$ is the external feedback induced perturbation term.

For multiple scatters as target, we must consider the backscattered contribution from each one retro-injected into the laser cavity as:

$$E_f(t) = \sum_i E_{f_i}(t) \tag{1.9}$$

where each $E_{f_i}(t)$ corresponds to:

$$E_{f_i}(t) = \frac{k_i}{\tau_C} E(t-\tau_i)\exp[j(\omega+\omega_{D_i})(t-\tau_i) \tag{1.10}$$

where τ_C is the laser cavity round-trip time of flight ($\tau_C = 2n_C L_C/c$, where c is speed of light); τ_i is the external cavity round-trip time of flight ($\tau_i = 2n_{\mathrm{ext}_i} L_{\mathrm{ext}_i}/c$) for each flowing particle characterized by its own reflectivity (n_{ext_i}), located at a particular distance (L_{ext_i}), and tracking a specific velocity V_i accordingly the flow profile, which induces a Doppler shift ($f_{D_i} = \omega_{D_i}/2\pi$) corresponding to the line-of-sight velocity (particle velocity projection along the optical axis) as $\omega_{D_i} = \omega 2V_i/(c+V_i)$; and k_i is the feedback coupling coefficient for each particle, defined as:

$$k_i = (1-r_2^2)\frac{r_{\mathrm{ext}_i}}{r_2} \tag{1.11}$$

with r_2 the reflectivity of the laser front facet mirror and r_{ext_i} the ratio of the back-scattered power actually retro-injected into the laser cavity over the laser emitted power.

Now considering the approximations of the quasi-steady state regime $[\mathrm{E}(\mathrm{t}-\tau) \sim \mathrm{E}(\mathrm{t})]$, which are feasible due to the fact that the Doppler shift corresponds to a very low frequency regarding to the laser optical frequency, then:

$$\frac{dE(t)}{dt} = \frac{1}{2}\Gamma G(N-N_{\mathrm{tr}})E(t) + \sum_i \frac{k_i}{\tau_C} E(t)\cos(\omega_{D_i} t + \phi_i), \tag{1.12}$$

$$\frac{d\Phi(t)}{dt} = \frac{1}{2}\alpha\Gamma G(N - N_{\mathrm{tr}}) + \sum_i \frac{k_i}{\tau_C} sin\left(\omega_{D_i} t + \phi_i\right), \tag{1.13}$$

$$\frac{dN(t)}{dt} = \frac{I}{qV_a} - G(N - N_{\mathrm{tr}})S - \frac{N}{\tau_N}, \tag{1.14}$$

where ϕ_i is a random phase; Φ is the phase term of the electric field E; α is the linewidth enhancement factor; q is the elementary charge; V_a is the laser active volume; τ_N is the carrier lifetime and S is the photon density which is linked to the electric field amplitude by $\mathrm{S} \propto \mathrm{E} \cdot \mathrm{E}^*$, which allows Eq. (1.12) be rewritten as:

$$\frac{dS(t)}{dt} = G(N - N_{\mathrm{th}})S(t) - \frac{S(t)}{\tau_S} + \sum_i \frac{k_i}{\tau_C} S(t)\cos(\omega_{D_i} t + \phi_i), \tag{1.15}$$

where N_{th} is the carrier density at threshold, and τ_S is the photon lifetime.

Following the very same methodologies as [50, 54] to solve the set of Eq. (1.12)-(1.15) for the quasi-steady state, leads to:

$$\omega_F - \omega_0 = \sqrt{1+\alpha^2} + \sum_i \frac{k_i}{\tau_C} sin[\omega_{D_i} t + \phi_i + \mathrm{atan}(\alpha)], \tag{1.16}$$

$$S_F = S_0 \left[1 + \sum_i \frac{2\tau_S}{\tau_C} k_i \cos(\omega_{D_i} t + \phi_i)\right], \tag{1.17}$$

where ω_F and ω_0 are the laser angular frequency with and without feedback respectively, and S_F and S_0 are the photon densities under similar conditions. So as the laser emitted power variations are proportional to the photon density, we can re-write from Eq. (1.17):

$$P_F = P_0\left[1 + \sum_i m_i \cos(\omega_{D_i} t + \phi_i)\right], \tag{1.18}$$

where m_i corresponds to the modulation index regarding the i$^{\mathrm{th}}$ particle, as $m_i = 2\tau_s k_i / \tau_C$.

It pertinent to mention that despite the Doppler shift ω_{D_i} is function of ω_F, for fluids where the optical feedback is very weak, the fluctuations in the laser frequency can be ignored for the calculation of the optical power variations.

1.4. Motivations of the present thesis

The Doppler OFI technology based in laser diodes has been extensively developed, demonstrating its recent potential to be applied in several fluidics sensing applications. The constant progress of these applications at micrometric scale opens high resolution 2D Doppler imaging for biological and chemical flows, and the capability of single particle detection and velocimetry as well.

That type of compact and embedded sensors is still very promising for a research and industrial field –microfluidics – that is itself a growing domain of activities, at the frontiers of the physics, the chemical science, the biology and the biomedical. The sensors that have been proposed so far are not able to provide further information on the nature of the particles flowing, so the capability of particle characterisation is a major challenge.

Our present research is focused on the implementation, validation and evaluation of the sensing performances of the OFI technology in both chemichal and biomedical fields of applications. The object of the present thesis is the elaboration of a new generation of sensors, that will provide both a high spatial resolution for imaging laminar flows as well as to give further information on the flowing particles concentrations and dimensions, opening a new domain of OFI research in the field of micro and nanoparticles characterizations.

We have chosen the Doppler approach with the evaluation and improvement of the signal processing methods in the spectral domain. Beyond the reasons, drawbacks, risks and limitations already enumerated against the Speckle approach, this method would be also unfeasible to explore potential applications for particle characterization, especially for cytometry, which requires capability of single micro and nanoparticle detection.

We propose a study over the aspects affecting the OFI signal morphology in spectral domain, and the suitable signal processing methods associated to an innovating optical configuration including a diffraction grating to accurately measure the flow velocity at single or multiple scattering regimes, especially considering the complexity of flow velocity measurements handling with different flow rates and concentrations.

We propose the design, validation and evaluation of a 2D Doppler imager based in a single 2-axis beam-steering mirror mounted on a MEMS, taking the full advantage of the compactness offered by the OFI sensing scheme. The compactness of the MEMS mirror allows the design of an embedded imaging system in a compact handheld case that provides quantitative information about the velocity of fluids. A clinical study with patients has been performed for potential application of this system in the biomedical field of skin cancer diagnosis.

The research conducted here open the path to potential applications in the field of particle characterization and cytometry with the development of an innovative technique to detect single micro and nanoparticles in a watery suspension made with polystyrene spheres at very low concentration. We investigate also, for instance, the possibility to detect bigger particles seeded at very low concentration in an aqueous suspension of smaller ones. In this case, the technique can suggest a potential application in the biomedical field for blood clot (thrombus) detection.

Beyond that, while other technologies require manipulation of the fluid, tending towards always smaller volume handling with precise flow and concentration control in order to size particles at macro or nano scale, we propose the use of the OFI technology to quantify the particle size and concentration with fluids.

Chapter references

1. Y. Yeh and H. Z. Cummins. *Localized fluid flow measurements with an he-ne laser spectrometer. Appl. Phys.* **1964**, *Lett 4, pp.* 176-178, 10.1063/1.1753925.
2. J. W. Foreman Jr., E. W. George, and R. D. Lewis. *Measurement of localized flow velocities in gases with a laser Doppler flowmeter*. Appl. Phys. **1965**, *Lett. 7*, 77, 10.1063/1.1754319.
3. J. W. Foreman, R. D. Lewis, J. R. Thornton, and H. J. Watson. *Laser Doppler velocimeter for measurement of localized flow velocities in liquids*. *Proc. IEEE.* **1966**, *vol. 54, no. 3*, *pp.* 424–425, 10.1109/PROC.1966.4732
4. M. J. Rudd. *A laser Doppler velocimeter employing the laser as a mixer-oscillator*. J. Phys. E: Sci. Instrum. **1968**, *vol. 1, no. 7*, *pp*. 723-726.
5. Seko, A., Mitsuhashi, Y., Morikawa, T., Shimada, J. and Sakurai, K. *Selfquenching in semiconductor lasers and its applications in optical memory readout*. Appl. Phys. Lett. **1975**, vol. 27(3), pp. 140-141.
6. J. H. Churnside. *Laser Doppler Velocimetry by Modulating a CO2 Laser with Backscattered Light*. Appl. Opt. **1984**. *vol.* 23, *p.* 61.
7. R. Lang and K. Kobayashi. *External optical feedback effects on semiconductor injection laser properties*. IEEE Journal of Quantum Electronics. **1980**, *vol.* 16, *no.* 3, *pp.* 347-355, 10.1109/JQE.1980.1070479.
8. S. Shinohara, A. Mochizuki, H. Yoshida, and Masao Sumi. *Laser Doppler velocimeter using the self-mixing effect of a semiconductor laser diode*. Appl. Opt. **1986**, *vol.* 25, *pp.* 1417-1419.
9. H. W. Jentink, F. F. M. de Mul, H. E. Suichies, J. G. Aarnoudse, and J. Greve. *Small laser Doppler velocimeter based on the self-mixing effect in a diode laser*. Appl. Opt. **1988**, *vol.* 27, *pp.* 379-385.
10. F. F. M. de Mul, M. H. Koelink, A. L. Weijers, J. Greve, J. G. Aarnoudse, R. Graaff, and A. C. M. Dassel. *Self-mixing laser-Doppler velocimetry of liquid flow and of blood perfusion in tissue*. Appl. Opt. **1992**, *vol.* 31, *pp.* 5844-5851.
11. F. F. De-mul, M. H. Koelink, A. L. Weijers, J. Greve, J. G. Aarnoudse et al., *A semiconductor laser used for direct measurement of the blood perfusion of tissue*, IEEE Transactions on Biomedical Engineering. **1993**, *vol.* 40, *issue* 2, *p.* 208, 10.1109/10.212062
12. R. Bonner and R. Nossal. *Model for laser Doppler measurements of blood flow in tissue*. Appl. Opt. **1981**, *vol.* 20, *pp.* 2097-2107.
13. M. Slot, M. H. Koelink, F. G. Scholten, F. F. M. de Mul, A. L. Weijers, J. Greve, R. Graaf, A. C. M. Dassel, J. G. Aaarnoudse, F. H. B. Tuynman. *Blood flow velocity measurements based on the self-mixing effect in a fiber coupled semiconductor laser: in-vivo and in-vitro measurements*. Med. Biol. Eng. Comput. **1992**, *vol.* 30, *pp.* 441-446.
14. M. H. Koelink, M. Slot, F. F. M. de Mul, J. Greve, R. Graaff, A. C. M. Dassel, and J. G. Aarnoudse. *Laser Doppler velocimeter based on the self-mixing effect in a fiber-coupled semiconductor laser: theory*. Appl. Opt. **1992**, *vol.* 31, *pp.* 3401-3408.
15. M. H. Koelink, M Slot, F. F. de Mul, J. Greve, R. Graaff, A. C. M. Sassel, J. G. Aarnoudse. *Glass-fibre self-mixing diode-laser Doppler velocimeter*. Meas. Sci. Technol. **1992**, *vol.* 3, *p.* 33.
16. M. H. Koelink, F. F. M. de Mul, A. L. Weijers, J. Greve, R. Graaff, A. C. M. Dassel, and J. G. Aarnoudse. *Fiber-coupled self-mixing diode-laser Doppler velocimeter: technical aspects and flow velocity profile disturbances in water and blood flows*. Appl. Opt. **1994**, *vol.* 33, *pp.* 5628-5641.
17. H. Koelink, F.F.M. de Mul, B. Leerkotte, J. Greve, H.W. Jentink, R. Graaff, A.C.M. Dassel, J.G. Aarnoudse. *Signal processing for a laser-Doppler blood perfusion meter*. Signal Processing. **1994**, *vol.* 38, *issue* 21994, *pp.* 239-252, ISSN 0165-1684, 10.1016/0165-1684(94)90143-0.
18. L. Scalise, W. Steenbergen, and F. de Mul. *Self-mixing feedback in a laser diode for intra-arterial optical blood velocimetry*. Appl. Opt. **2001**, *vol.* 40, *pp.* 4608-4615.

19. F. F. M. de Mul, L. Scalise, A. L. Petoukhova, M. V. Herwijnen, P. Moes, and W. Steenbergen. *Glass-fiber self-mixing intra-arterial laser Doppler velocimetry: signal stability and feedback analysis*. Appl. Opt. **2002**, *vol.* 41, *pp.* 658-667.
20. J. Hast, R. A. Myllylä, H. Sorvoja, J. Miettinen. *Arterial pulse shape measurement using self-mixing effect in a diode laser*. Quantum Electron. **2002**, *vol.* 32 (11), *pp.* 975–980.
21. C. M. Zakian, M. R. Dickinson and T. King. *Particle Sizing and flow measurements using self-mixing interferometry with a laser diode*. J. Opt. A: Pure Appl. Opt. **2005**, *vol.* 7, *no.* 6, *p.* 445, 10.1088/1464-4258/7/6/029.
22. C. M. Zakian, M. R. Dickinson, and T. King. *Dynamic light scattering by using self-mixing interferometry with a laser diode*. Appl. Opt. **2006**, *vol.* 45, *pp.* 2240-2245.
23. C. M. Zakian, M. R. Dickinson. Flow measurements through scattering samples using self-mixing interferometry with a laser diode. *Proc. SPIE, Biophotonics and New Therapy Frontiers*. **2006**, *vol.* 6191. 10.1117/12.662518.
24. C. M. Zakian and M. R. Dickinson. Laser Doppler imaging through tissues phantoms by using self-mixing interferometry with a laser diode. *Applied Optics*. **2007**, *vol.* 32, *no.* 19.
25. J. R. Tucker, Y. L. Lim, K. Bertling, A. V. Zvyagin and A. D. Rakić. *Fluid flow rate measurement using the change in laser junction voltage due to the self-mixing effect. 2006 Conference on Optoelectronic and Microelectronic Materials and Devices, Perth, WA*. **2006**, *pp.* 192-195. 10.1109/COMMAD.2006.4429913.
26. J. R. Tucker, J. L. Baque, Y. L. Lim, A. V. Zvyagin, and A. D. Rakić. *Parallel self-mixing imaging system based on an array of vertical-cavity surface-emitting lasers*. Appl. Opt. **2007**, *vol.* 46, *pp.* 6237-6246.
27. Y. L. Lim, R. Kliese, K. Bertling and A. D. Rakić. *Parallel self-mixing flow sensor using monolithic VCSEL array*. 2008 Conference on Optoelectronic and Microelectronic Materials and Devices, Sydney, SA. **2008**, *pp.* 67-70. 10.1109/COMMAD.2008.4802093
28. R. Kliese, Y. L. Lim, E. Stefan, J. Perchoux, S. J. Wilson and A. D. Rakić. *Rapid scanning flow sensor based on the self-mixing effect in a VCSEL*. 2010 Conference on Optoelectronic and Microelectronic Materials and Devices, Canberra, ACT. **2010**, *pp.* 7-8. 10.1109/COMMAD.2010.5699789
29. R. Kliese, Yah Leng Lim, T. Bosch, and A. D. Rakić. *GaN laser self-mixing velocimeter for measuring slow flows*. Opt. Lett. **2010**, *vol.* 35, *pp.* 814-816.
30. M. Nikolić, E. Hicks, Y. L. Lim, K. Bertling, and A. D. Rakić. *Self-mixing laser Doppler flow sensor: an optofluidic implementation*. Appl. Opt. **2013**, *vol.* 52, *pp.* 8128-8133.
31. M. Nikolić et al. *Flow profile measurement in micro-channels using changes in laser junction voltage due to Self-mixing effect*. 2011 IEEE SENSORS Proceedings, Limerick. **2011**, *pp.* 1394-1397. 10.1109/ICSENS.2011.6127217
32. L. Campagnolo, S. Roman, J. Perchoux and S. Lorthois. *A new optical feedback interferometer for measuring red blood cell velocity distributions in individual capillaries: a feasibility study in microchannels*. Comp. Methods in Biomech. and Biomed. Eng. **2012**, *vol.* 15, *pp.* 104-105, 10.1080/10255842.2012.713651.
33. A. Quotb, E. E. Ramírez-Miquet, C. Tronche and J. Perchoux. *Optical Feedback Interferometry sensor for flow characterization inside ex-vivo vessel*. IEEE SENSORS 2014 Proceedings, Valencia. **2014**, *pp.* 362-365. 10.1109/ICSENS.2014.6985009
34. E. E. Ramirez-Miquet, A. L. Arriaga, A. Quotb, O. Sotolongo-Costa and J. Perchoux. *In-situ measurement of non-steady flows using optical feedback interferometry*. 2015 IEEE International Conference on Industrial Technology (ICIT), Seville. **2015**, *pp.* 1469-1473. 10.1109/ICIT.2015.7125304
35. E. E. Ramírez-Miquet, J. Perchoux, K. Loubière, C.Tronche, L.Prat, and O. Sotolongo-Costa. *Optical Feedback Interferometry for Velocity Measurement of Parallel Liquid-Liquid Flows in a Microchannel*. Sensors. **2016**, *vol.* 16, *issue* 8, *p.* 1233. 10.3390/s16081233

36. Y. Zhao, J. Perchoux, L. Campagnolo, T. Camps, R. Atashkhooei, and V. Bardinal. *Optical feedback interferometry for microscale-flow sensing study: numerical simulation and experimental validation*. Opt. Express. **2016**, *vol.* 24, *pp.* 23849-23862.
37. A. Alexandrova and C. P. Welsch. *Laser diode self-mixing technique for liquid velocimetry*. Nuclear Instruments and Methods in Physics Research A. **2016**, *vol.* 830, *pp.* 497-503.
38. F. Marazzi, F. Truffer2, M. Geiser. *Laser Doppler Flowmetry versatile acquisition system with low quantization error*. Journal of Biomedical Engineering and Informatics. **2018**, *vol.* 4, *no.* 1. 10.5430/jbei.v4n1p25.
39. J. David Briers. *Laser Doppler and time-varying speckle: a reconciliation*. J. Opt. Soc. Am. A. **1996**, *vol.* 13, *pp.* 345-350.
40. J. David Briers. *Laser Doppler, speckle and related techniques for blood perfusion mapping and imaging.* Physiol. Meas. **2001**, *vol.* 22, *pp.* 35-66.
41. S. K. Özdemir, S. Ito, S. Shinohara, H. Yoshida, and M. Sumi. *Correlation-based speckle velocimeter with self-mixing interference in a semiconductor laser diode.* Applied Optics. **1999**, *vol.* 38 *no.* 33.
42. S. K. Özdemir, S. Takamiya, S. Ito, and S. Shinohara. *Self-Mixing Laser Speckle Velocimeter for Blood Flow Measurement.* IEEE Transactions on Instrum. and Meas. **2000**, *vol*. 49, *no.* 5.
43. S. K. Özdemir, I. Ohno, S. Shinohara. *A Comparative Study for the Assessment on Blood Flow Measurement Using Self-Mixing Laser Speckle Interferometer.* IEEE Transactions on Instrum. and Meas. **2008**, *vol.* 57, *no.* 2.
44. E. Figueiras, R. Oliveira, C. F. Lourenço, R. Campos, A. Humeau-Heurtier, R. M. Barbosa, J. Laranjinha, L. F. R. Ferreira, and F. F. M. de Mul. *Self-mixing microprobe for monitoring microvascular perfusion in rat brain*. Med. Biol. Eng. Comput. **2013**, *vol.* 51(1-2), *pp.* 103-112.
45. S. K. Ozdemir, S. Takamiya, S. Shinohara, H. Yoshida and M. Sumi. *Speckle velocimeter with a self-mixing laser diode: optimization of measurement system, reproducibility and accuracy of measurements*. Proceedings of the 17th IEEE Instrumentation and Measurement Technology Conference, Baltimore, MD. **2000**, *pp.* 717-722 *vol.* 2. 10.1109/IMTC.2000.848830
46. M. I. Mishchenko, J. W. Hovenier, and D. W. Mackowski. *Single scattering by a small volume element*. J. Opt. Soc. Am. A. **2004**, *vol.* 21, *pp.* 71-87.
47. A. Quirantes, F. Arroyo, and J. Quirantes-Ros. *Multiple Light Scattering by Spherical Particle Systems and Its Dependence on Concentration: A T-Matrix Study*. Journal of Colloid and Interface Science. **2001**, *vol.* 240, issue 1, *pp.* 78-82, ISSN 0021-9797. 10.1006/jcis.2001.7641.
48. S. Sudo, Y. Miyasaka and K. Otsuka. *Quick and easy measurement of particle size of Brownian particles and plankton in water using self-mixing laser.* Optics Express. **2006**, *vol.* 14, *no.* 3.
49. R. Lang and K. Kobayashi. *External optical feedback effects on semiconductor injection laser properties*. IEEE Journal of Quantum Electronics. **1980**, *vol.* 16, *no.* 3, *pp.* 347-355. 10.1109/JQE.1980.1070479
50. D. M. Kane, and K. A Shore. *Unlocking Dynamical Diversity – Optical feedback effects on semiconductor lasers*. Wiley, **2005**.
51. C. Zakian, M. Dickinson, and T. King. *Particle sizing and flow measurement using self-mixing interferometry with a laser diode.* J. Opt. A: Pure Appl. Opt. **2005**, *vol.* 7, *pp.* S445-S452.
52. C. Zakian, M. Dickinson, and T. King. *Dynamic light scattering by using self-mixing interferometry with a laser diode*. Appl. Opt. **2006**, *vol.* 45, *pp.* 2240-2245.
53. E. E. Ramírez-Miquet. *Implementation of Optical Feedback Interferometry for Sensing Applications in Fluidic Systems*. Doctorat de l'Université de Toulouse, INP Toulouse, September 29th 2016.
54. R. Kliese, T. Taimre, A. A. A. Bakar, Y. L. Lim, K. Bertling, M. Nikolić, J. Perchoux, T. Bosch, and A. D. Rakić. *Solving self-mixing equations for arbitrary feedback levels: a concise algorithm*. Appl. Opt. **2014**, *vol.* 53, *pp.* 3723-3736.

CHAPTER 2: OFI flow monitoring

2.1. Context

In the actual context of the microfluidics research and development we can highlight two main domains of applications: the chemical one, that includes micromixers, microreactors and lab-on-chip devices; and the biomedical one, mostly related to microvascular researches and cytometry. Both fields require high accuracy in velocimetry associated to aspects like non-invasiveness and compactness.

Among the Doppler based technologies, since the sixties the Laser Doppler Velocimetry technology has been pushed in the field of biomedical applications [1-8]. However, even if nowadays it reached a high spatial resolution up to 1 µm [9], it is still a bulky, expensive and a complex technology compared to OFI sensing with regards to the requirements of microfluidics applications.

Due to the proper characteristics of the OFI sensing scheme: non-invasiveness, compactness, simplicity, self-alignment and reduced cost, this approach has demonstrated being a promising solution in the microfluidics field, more precisely with velocimetry applications based on Doppler-Fizeau effect [10,11]. Several signal processing methods have been proposed to deal mostly with the measurement of the average Doppler frequency [12-22] corresponding to the velocity measurement in micro-channels. In this context, the spectral morphology of the OFI signal is determinant on the decision regarding the proper signal processing method to be used in order to exploit the flow velocity.

2.2. Signal processing methods

2.2.1. Spectral morphology

The signal processing method to quantify the flow velocity depends strongly of the spectral morphology of the OFI signal which one can be affected by several aspects related with the design of the OFI sensing system and the flow hydrodynamics. In that way, the fluidic channel is actually part of the sensing system, as its shape and dimensions affect the flow profile. Also, the scattering properties, concentration, shape and dimensions of the scattering particles embedded in the flow impact the sensing volume and consequently the spectral morphology of the OFI signal. In other words, the optical configuration, the flow hydrodynamics and the nature of the scatterers define the spectral distribution from which the quantitative velocity value shall be extracted.

The optical system is defined by the laser diode together with the optical arrangement that determines the laser spot size and shape. In flow monitoring applications, the laser spot is generally located at the central axis of the micro-channel, in order to set a measurement volume that covers the hydrodynamic region corresponding to the maximum fluid velocity.

In order to illustrate the relation between the spot size and the spectral morphology of the OFI signal, the Fig. 1b depicts the signals computed for three spot sizes and for a 665 nm VCSEL (Vertical-Cavity Surface-Emitting Laser) which spot shape is expected perfectly circular. The laser spot is always focused at the center of a circular 500 μm micro-channel. The velocity distribution for a constant flow rate with a laminar flow for a Newtonian fluid is depicted by the concentric circles of Fig. 1a.

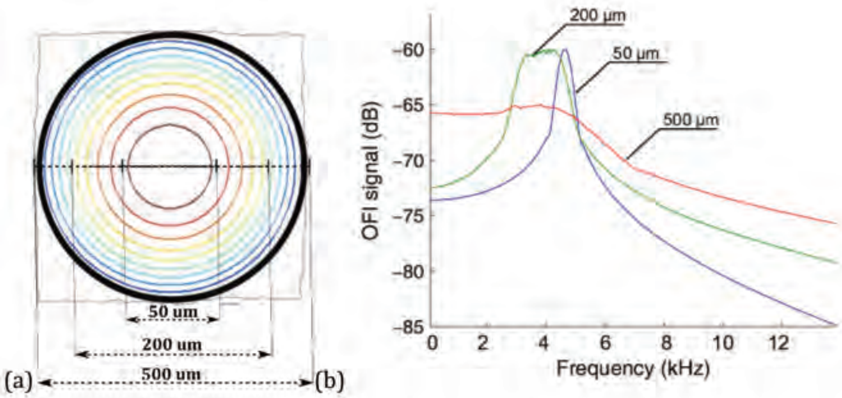

Fig. 1. (a) Axial view of the flow velocity distribution (color scale from blue (low velocity) to red (high velocity)) with three centered VCSEL laser spot sizes represented by black bars covering the velocity distribution for a laminar flow at constant flow rate in a 500µm circular micro-channel (adapted from [23]). (b) OFI signal spectra under single scattering regime based on simulations for three spot sizes (50µm, 200µm and 500µm). [23]

While considering only the single scattering regime, the Doppler shift that affects each photon is due to an interaction with a unique scatterer. Each scatterer considered as a localized scattering center, with a unique local velocity as it travels through the sensing volume. In other words, each scatterer contributes to the OFI signal as a velocity tracker following the velocity distribution. The Fig. 1b shows the simulation results for the OFI signal spectra under single scattering. As we can see, the spectral broadening is proportional to the spot radii.

In the case of a spot size one hundred times smaller than the channel diameter, the OFI spectrum exhibit a Gaussian shape, which peaks is closely related to the maximum velocity. Thus, the signal processing method to determine the maximum flow velocity consists in the detection of the most prominent peak. The detection can be made after computing a Gaussian fitting function of the spectrum.

For the case where the spot size covers the full channel diameter, we observe a wide spectral broadening corresponding to the total velocity distribution. Under such conditions, another approach to extract the velocity information where the maximum velocity is approximated by a cut-off frequency method [1, 21, 22, 31].

In the OFI signal spectral morphology corresponding to the 200 µm spot another signal processing method would be required.

The 1st weighted Moment approximation [9, 11-20, 26, 29] is a more universal approach of spectral analysis to computes the average flow velocity.

The previous simulation of the influence of the sensing volume extension serves to demonstrate that, even considering only the single scattering regime, a unique signal processing method for flowmetry in all three situations would be challenging for a proper velocimetry.

Regarding the flow conditions, they are defined by the hydrodynamics of the channel design and by the pumping system. The scope of our researches is limited to the flowmetry in Newtonian fluids under laminar flow condition, where a fixed flow rate can be controlled by the pumping system. In that way, a theoretical velocity distribution can easily be calculated.

Beyond the fact the optical feedback is affected by the scattering regime; the scattering properties are intrinsic to the laser light interaction with the scatterers embedded in the fluid. The scatterer's optical properties (as reflective and refractive indexes) and the scatterer shape and size [25-27] play a role defining the scattering cross-section related with the laser sensing volume. Also, regarding the signal amplitude, the larger the scatterers size and concentration, the higher they shall be. Thus, with proper experimental conditions, beyond the velocity measurements, the quantifications of particle sizes would be possible.

2.2.2. Cut-off frequency method

The signal processing method for spectra with a flat frequency distribution (Fig. 2) requires to find a cut-off frequency to estimate the maximum Doppler frequency (related to the maximum fluid velocity V_{max} in the probe volume):

$$f_{D_{-3\mathrm{dB}}} = \frac{2nV_{\mathrm{max}}\mathrm{cos}\theta}{\lambda}, \qquad (2.1)$$

where θ is the angle between the laser beam axis and the scatter velocity vector; n is the refractive index of the fluid; and λ is the wavelength of the laser.

The issue with the cut-off frequency method is that the empirical criterion of -3 dB threshold regarding the plateau level is not robust enough, as it can varies significantly with the scatterers concentration [22] while the sensing volume dimension may have an influence [9].

The estimation of the maximum Doppler frequency can be automatized but such implementation is not trivial and the results presented in the following were obtained manually.

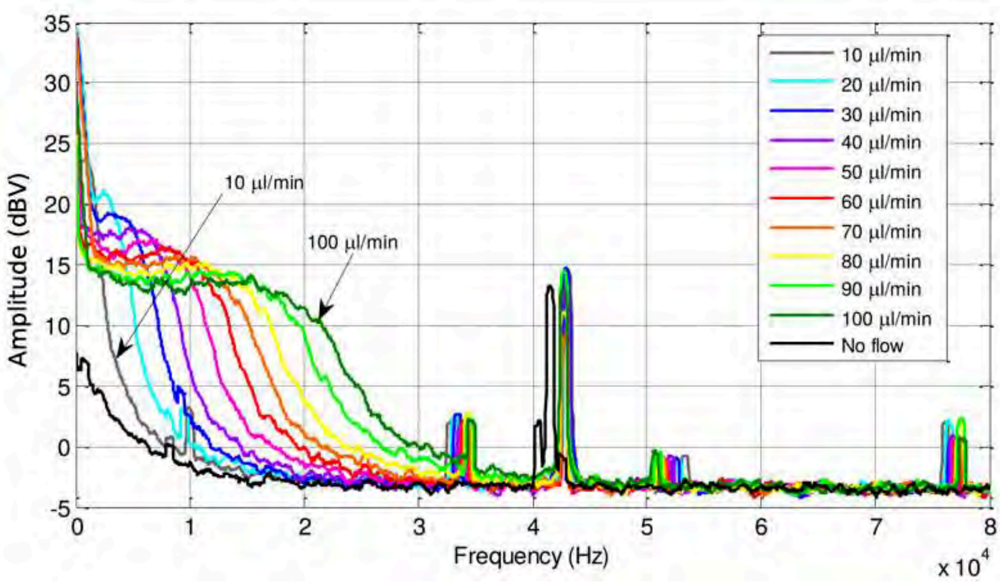

Fig. 2. OFI signal power spectra for various flow rates with 2% w/w milk dilution in water [20].

2.2.3. Peak detection method

Regarding the signal processing method for spectra presenting a peak, the procedure consists in finding the most prominent point. It has been implemented using Matlab's *findpeaks* function. The Doppler frequency is related to the maximum fluid velocity V_{max} in the probe volume as in Eq. 2.2.

$$f_{D_{\mathrm{peak}}} = \frac{2nV_{\mathrm{max}}\cos\theta}{\lambda}, \qquad (2.2)$$

For a proper prominence detection in each spectrum, the contribution of the Doppler signal is isolated by subtraction of a reference spectrum corresponding to sensor signal without any flow (measurement into the void channel). The remaining spectrum is set in logarithm scale and smoothed using Savitzky-Golay filter, and the most prominent peak is detected as illustrated in *Fig. 3*.

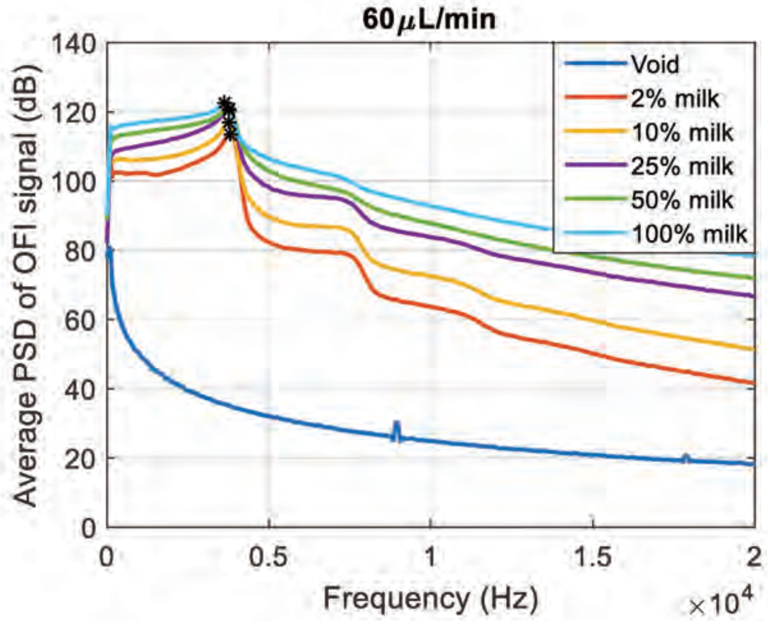

Fig. 3. Smoothed average spectra of thirty consecutive measurements of OFI signal power at 60 μL/min for five milk concentrations, depicted with the most prominent points detected by the algorithm implemented in MATLAB script.

2.2.4. Moment method

For the OFI spectra exhibiting a slow decay (Fig. 4), the interpretation is that the Doppler frequency distribution corresponds to random velocities resulting from multiple scattering due to the high density of scatters inside the sensing volume. In that way the spectral distribution contains a statistical distribution of Doppler frequencies, and a statistical approach is required.

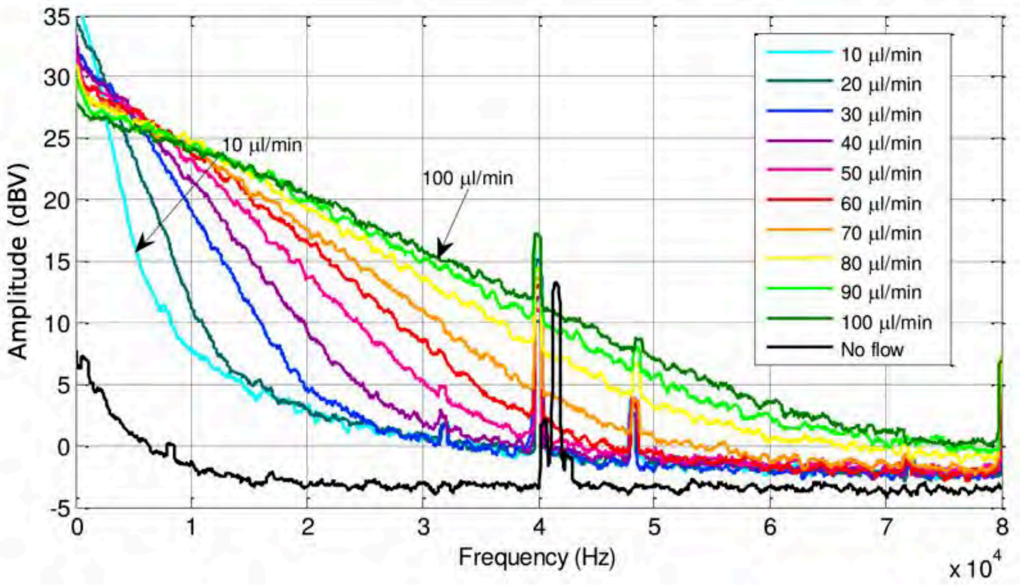

Fig. 4. OFI signal power spectra for various flow rates with 100% milk solution [20].

From each spectrum calculated, similarly than for the peak detection method, a subtraction of the reference spectrum (measured for the empty channel) is computed. The resulting spectrum is squared to correspond to the power spectral density (PSD).

The average Doppler frequency ($\overline{f_D}$) is derived from the 1st weighted raw moment (explained in the Chapter 1) as

$$\overline{f_D} = \frac{M_1}{M_0} = \frac{\int_{fmin}^{fmax} f.P(f)df}{\int_{fmin}^{fmax} P(f)df}\,, \tag{2.2}$$

where M_1 is the 1st order raw moment; M_0 is the 0-order raw moment; f_{min} and f_{max} set the spectral frequency range; and $P(f)$ is the amplitude of the power spectral density (PSD).

de Mul et al. [13] describe that M_0 (the integration of the OFI power spectrum) is proportional to the number of Doppler scatterers and M_1 is proportional to that scatterers number times the averaged velocity.

In this chapter we will perform flow monitoring using two different optical schemes. One is based on a single lens producing a poorly focused beam and a large sensing volume, the other using a double lens for sharper focusing and tight sensing volume extension. For each case, the three different signal processing methods will be evaluated for several scatterer concentrations, from single to multiple scattering regimes.

2.3. Materials and methods

2.3.1. Fluidic channels

The fluidic channels used in this study consist of a single duct made with polydimehylsiloxane (PDMS), which is an organic polymer with low cost and manufacturing simplicity. PDMS is hydrophobic, so water (or glycerol, for example) doesn't deform the flowchannel or leak from it. Due to these characteristics PDMS is widely used in microfluidics domain to easily prototype the conception of different designs, including complex hydrodynamic applications involving even design in multiple layers [35]. The manufacturing process of the fluidic of our channels is fully described in Appendix 1.

The actual dimension have been characterized to bea rectangular section of 600 µm x 270 µm (W x H) with a length of 350 mm.

In order to ensure that the measurement will be performed in the laminar regime of the flow, the laser sensing volume must be placed away of the entrance region. This hydrodynamic entry length [36-38] is given approximately by: $L_h \cong 0.05ReD$, where Re is the Reynolds Number and D is the pipe diameter for a circular channel. In case of a rectangular duct, D is given by a hydrodynamic diameter (D_h) according $D_h = \frac{2ab}{a+b}$, where a is the duct's height and b *is* its width. For our rectangular channel, L_h has been calculated to be 71.4 µm away from the inlet. Thus, sensing operates in a region where the velocity profile is expected to be fully developed, following the *Hagen-Poiseuille* velocity profile for a Newtonian fluid.

Another pertinent aspect on the hydrodynamic characterization of this PDMS rectangular duct is the maximum-to-average velocity ratio k that is roughly 1.96 [39]. As the average velocity corresponds to Q/A (where Q is the volumetric flow rate and A is the duct cross section area), so we can obtain the theoretical maximum velocity (kQ/A) using the pumping flow rate.

Figure 5 displays the theoretical velocity profiles calculated according [39] (pp. 197-198, equations 335-338).

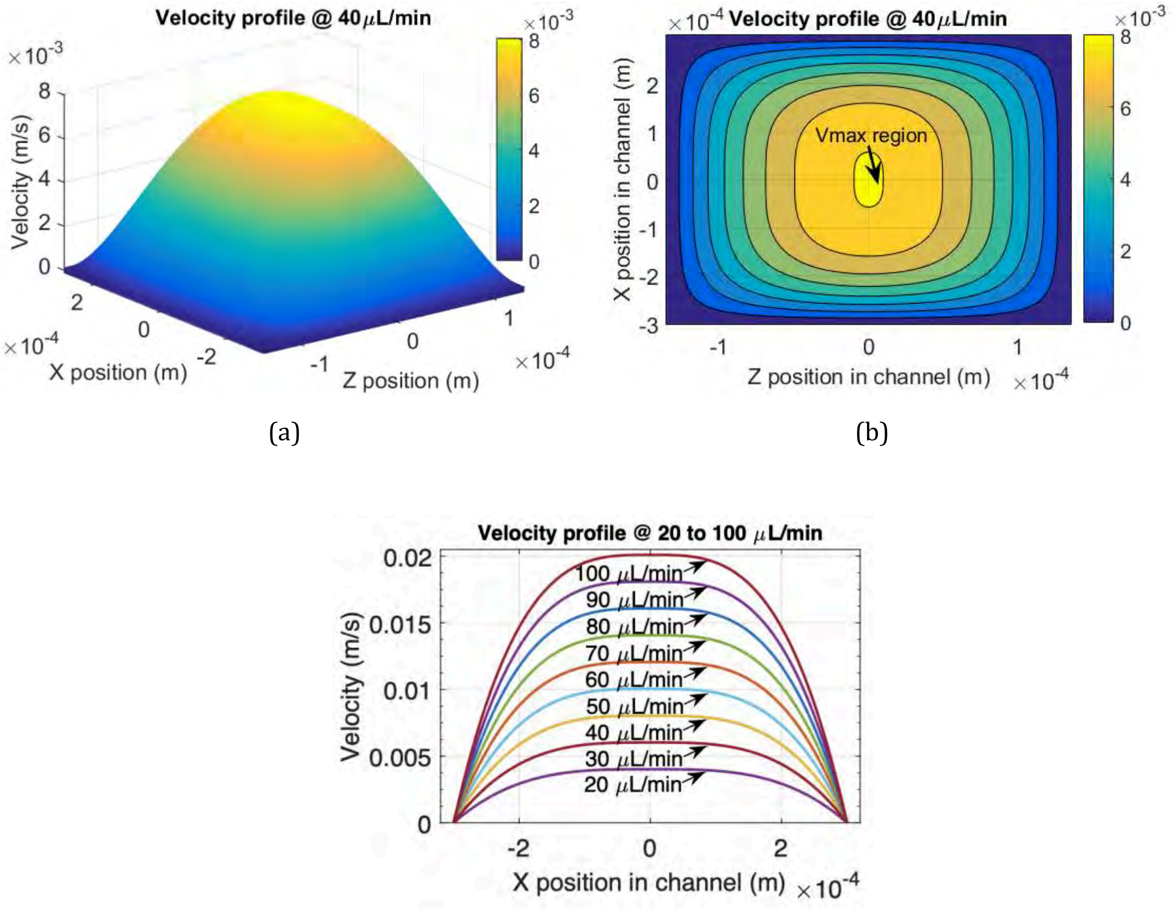

(a) (b)

(c)

Fig. 5. Velocity profile in the 600µm x 270 µm PDMS channel. (a) 3D velocity profile at 40µL/min. (b) Velocity profile as 2D intensity graph depicting the maximum velocity (v_{max}) region at 40µL/min (c) 2D velocity profiles at nine flow rates from 20 to 100 µL/min.

A circular cross-section PDMS channel has been used as well. Its manufacturing is simpler, requiring simply to put an optical fiber with the desired diameter through a support mold filled with the mixed elastomer to cure in ambient temperature during 24h. Then the fiber is pulled off after the curing. In that way, a 320-μm diameter channel (230 mm long) was made which maximum-to-average velocity ratio (*k*) is equal to 2. And for the related experiments, the calculated hydrodynamic entrance region corresponds to 42.24μm.

2.3.2. Single lens scheme

The single lens configuration is the most commonly used in OFI sensing published papers. It has the great advantage of simplicity and compactness but a poor focusing sharpness. In this section we present an evaluation of the signal processing method for this optical configuration as depicted in *Fig. 6*.

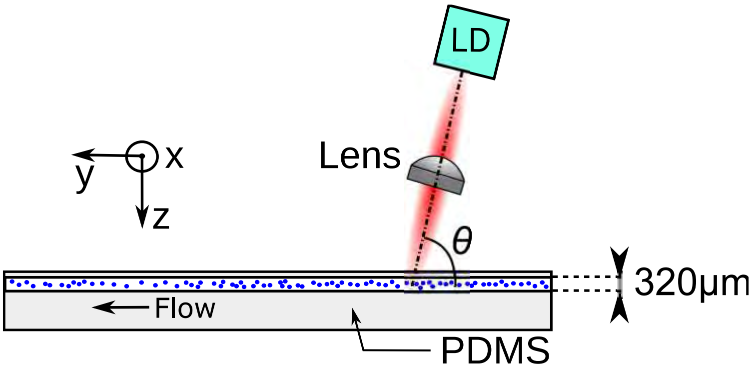

Fig. 6. Single lens experimental setup with θ=80.5° (adapted from [20]).

The experimental setup is composed of a laser diode (LD – Thorlabs L785P090) lasing at a wavelength of 785 nm, a focusing lens (Thorlabs C240-TME-B) placed at twice its focal length in order to focus the laser beam at the center of the 320 μm-diameter circular PDMS micro-channel. The optical axis is tilted by 80.5° with respect to the flow direction.

The incertitude on the incidence angle θ is a major issue in the determination of the maximum or the local flow velocity. This uncertainty is due to mechanical alignment control difficulties, intrinsic non-orthogonality of the laser beam since the packaging itself and/or from the mounting of the optical configurations. Thus, beforehand this set of experiment, a calibration was performed at a known flow rate, in order to determine through Eq. 2.1 the actual value of θ to be considered.

The whole OFI sensor is mounted on a 3-axis linear stage (Zaber Tech. T-LSM050A) enabling micrometric accuracy of displacement in *xyz* directions which ensure to set the focus point in the center of the channel, and away of the entrance region. Then the sensing operates in a region where the velocity profile is expected to be fully developed, properly fitting the *Hagen-Poiseuille* velocity profile for a Newtonian fluid.

The output laser power is monitored by the photodiode integrated in the laser package, and the OFI signal is acquired through a transimpedance amplifier. Sampling and storage of this signal is done by an A/D acquisition board (National Instruments BNC-2110) connected to a PC.

Regarding the OFI signal acquisitions, a Labview VI (including embedded MATLAB signal processing scripts) was designed to store the frequency spectrum in linear amplitude of the consecutive measurements for each flow rate at a given concentration, in order to evaluate the standard deviation of the estimated maximum Doppler frequency.

At each measurement ten consecutive frames of 8192 samples are acquired and the calculated spectrum is the average of the ten consecutive spectra. The determination of the Doppler frequency is done in a post-processing step although.

The mother solution used in the present work is full milk, as milk presents a high scattering coefficient and low absorption, while being an easy solution to obtain with high repeatability thanks to industrial production. Also it is a suitable optical phantom [33, 34] for blood, as the optical properties of milk's lipid cells are similar to the red blood cells, which are the main scatters tracing the blood perfusion velocity in laser flowmetry for biomedical applications.

For matter of accuracy regarding the actual refractive index of the fluid to be used in calculations, including the precise determination of the theoretical Doppler angle due to Snell-Descartes refraction, we have measured the refractive index for each dilution using a fibre optic Fresnel ratio meter [38]. The following values for *n* were obtained: 1.33 for 2% milk; 1.33 for 10%; 1.34 for 25%; 1.35 for 50%; and 1.35 for full milk. As the measured variations doesn't have an important impact on the determination of the Doppler frequency, for matter of simplicity we have considered a mean value of 1.34 for *n*.

The liquid is pumped with a 10mL syringe linear pump (Harvard Apparatus Pico 11 Plus) in 10 different flow rates from 10 µL/min to 100 µL/min, for each bovine milk concentrations from 100% to 2% v/v after dilution in demineralized water.

The morphology of the signal spectra doesn't reveal a well-defined Doppler peak, not even under the single scattering regime. Instead, as we can see in Fig. 7, it shows either a flat frequency distribution from 0Hz to roughly the maximum achievable Doppler frequency shift or a slow decay from low to higher frequencies, as it reaches a scatterer density high enough to characterize a multiple scattering regime.

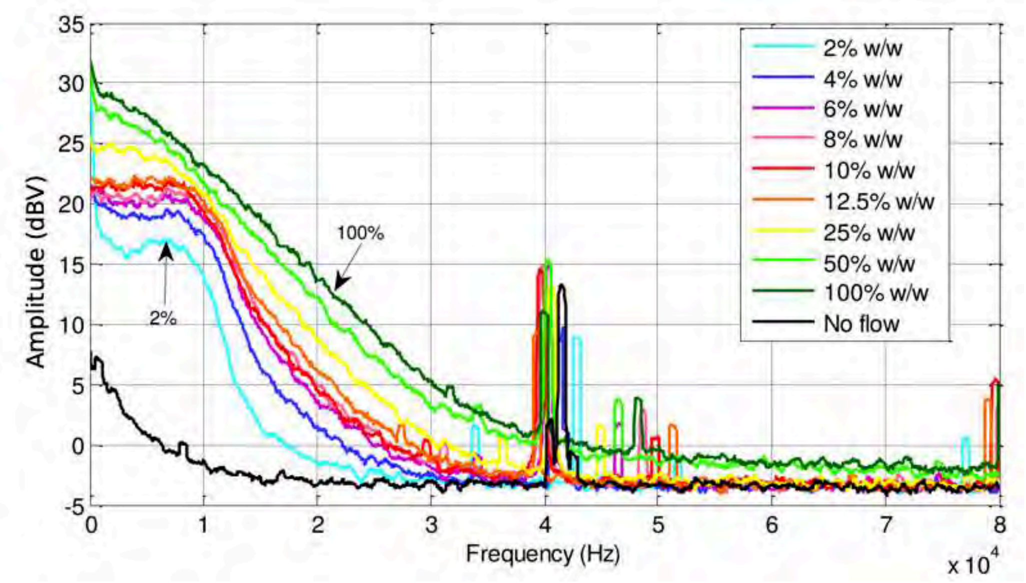

Fig. 7. OFI signal power spectra varying the milk concentration while keeping the flow rate at 50μL/min [20].

In the absence of any prominent peak in the spectra, both the cutoff frequency and the weighted moment methods were evaluated in all 9 milk concentrations across 10 flow rates. Fig. 8a shows the relative error for cutoff and weighted moment methods, averaged over the whole flow-rate range. With similar approach, Fig. 8b reveals the evolution of the standard deviation versus the scatter concentration.

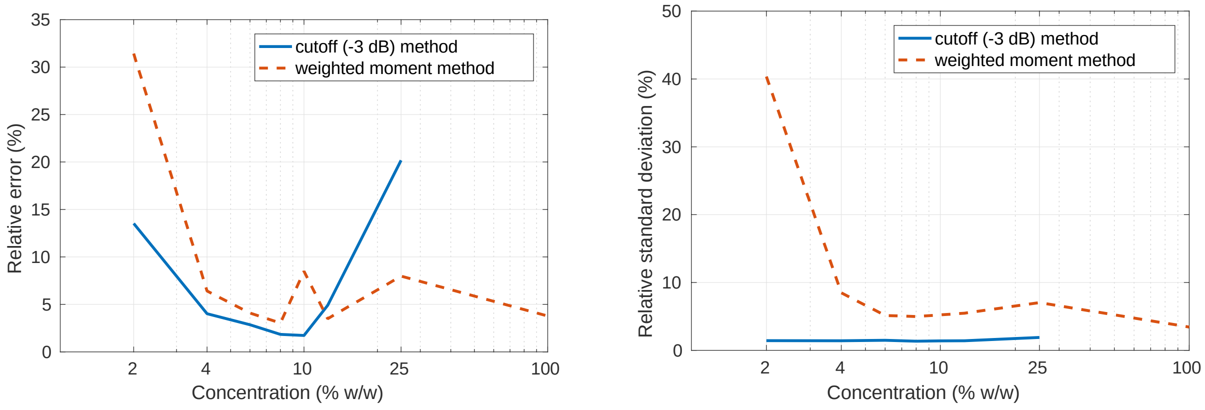

(a) (b)

Fig. 8. (a) Relative error and (b) relative standard deviation of the cut-off frequency (blue solid line) and the weighted moment (red dashed line) methods regarding the expected theoretical value, versus the milk concentration ratio by averaging the values measured for each flow rate [20].

As we can see in Fig. 8, the cut-off frequency method revealed to be reliable and robust for the OFI spectra presenting a flat distribution (up to 25% milk concentration) with mean relative error below 5% for the milk concentrations between 4 to 12.5%. The statistical Moment method showed to be inaccurate to estimate the average velocity at low milk concentrations (below 4%), but presented a good standard deviation (below 10%) for the velocity measurements from 4% to full milk concentrations.

2.3.3. Double lens scheme

The optical configuration of our 2 lenses OFI sensing scheme will be based on a collimating and a focusing lens. This configuration is expected to improve the SNR by increasing the power density in a reduced sensing volume and improving the back-scattered light collection as the focusing lens is closer to the target.

We evaluate the signal processing method based on spectral detection of the maximum Doppler peak [2, 31] to estimate the maximum fluid velocity. To the best of our knowledge, this method was never evaluated against the impact of the scatter concentration, especially under the multiple scattering regime.

Regarding the hydrodynamic flow conditioning, now we'll use the rectangular (600µm x 270µm) PDMS fluidic channel for our OFI sensing system. As compared to the cylindrical channel, this channel offers a wider region corresponding to the maximum velocity and thus simplifies the lateral alignment of the laser beam. The Fig. 9 illustrates the elements used in the experimental setup. The optical part of the OFI sensor is formed by a laser diode with a monitoring photodiode embedded in-package; a collimating lens (Thorlabs C660TME-C); and a focusing lens (Thorlabs LA1951-C).

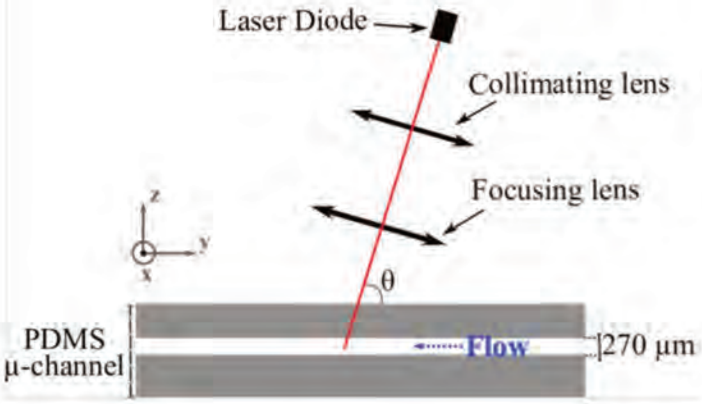

Fig. 9. Double lens experimental setup (θ=80°).

The laser diode is a DFB emitting at 1310nm with both longitudinal and transverse single mode emission (Thorlabs L1310P5DFB); it is driven by a custom-made driver that sets the laser at the nominal power of 5mW. From now on, sampling and storage of the signal is done by another version of acquisition board (National Instruments NI-6361 USB) connected to a PC, and each measurement is obtained by the mean of twenty *pwelch* spectra (2^{17} points, with no overlapping windows of 2^{13} samples, with a sampling rate of 500 kHz).

The angle θ was set to 80°. The whole OFI sensor is mounted on a 2-axis linear stage (Zaber Tech. T-LSM100A with step resolution of 47.625nm) enabling a micrometric accuracy of displacement in *x* and *z* directions during the procedure which ensure to set the focus points in the center of the channel.

Peak detection method

In each recorded spectrum, after a truncation at 20 kHz, the contribution of the Doppler signal is isolated by subtraction of a reference spectrum corresponding to the OFI signal without any flow (measurement into the void channel). Eventually the remaining spectrum in logarithm scale is smoothed using Savitzky-Golay filter, and the most prominent peak is detected.

Fig. 10 shows the average of the computed spectra at (a) 30 µL/min and (b) 100 µL/min. The spectrum related to no flow (void) is indicated for reference. The * mark locates the most prominent point, roughly corresponding to the maximum Doppler frequency shift in the laser focal point.

As we can easily perceive, the SNR obtained with the double lens configuration is much higher than the one from the single lens. This is due to a sharper focalization which implicates in a higher power density, and consequently more optical feedback power retro-injected. We can even perceive the presence of two harmonics.

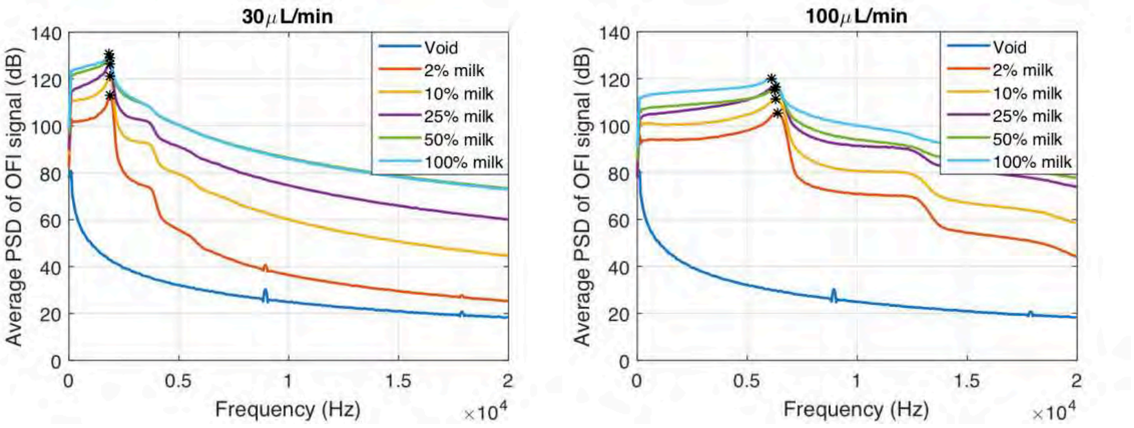

(a)

(b)

Fig. 10. Average of computed spectra for (a) 30 μL/min and (b) 100 μL/min for five milk concentrations, depicted with the most prominent point detected by the algorithm implemented in MATLAB script.

Fig. 11 depicts the average of computed spectra for all nine flow rates for 4 different milk concentration ratios. As we can easily see, it is very feasible to apply the peak detection method in all flow rates at all five milk concentrations.

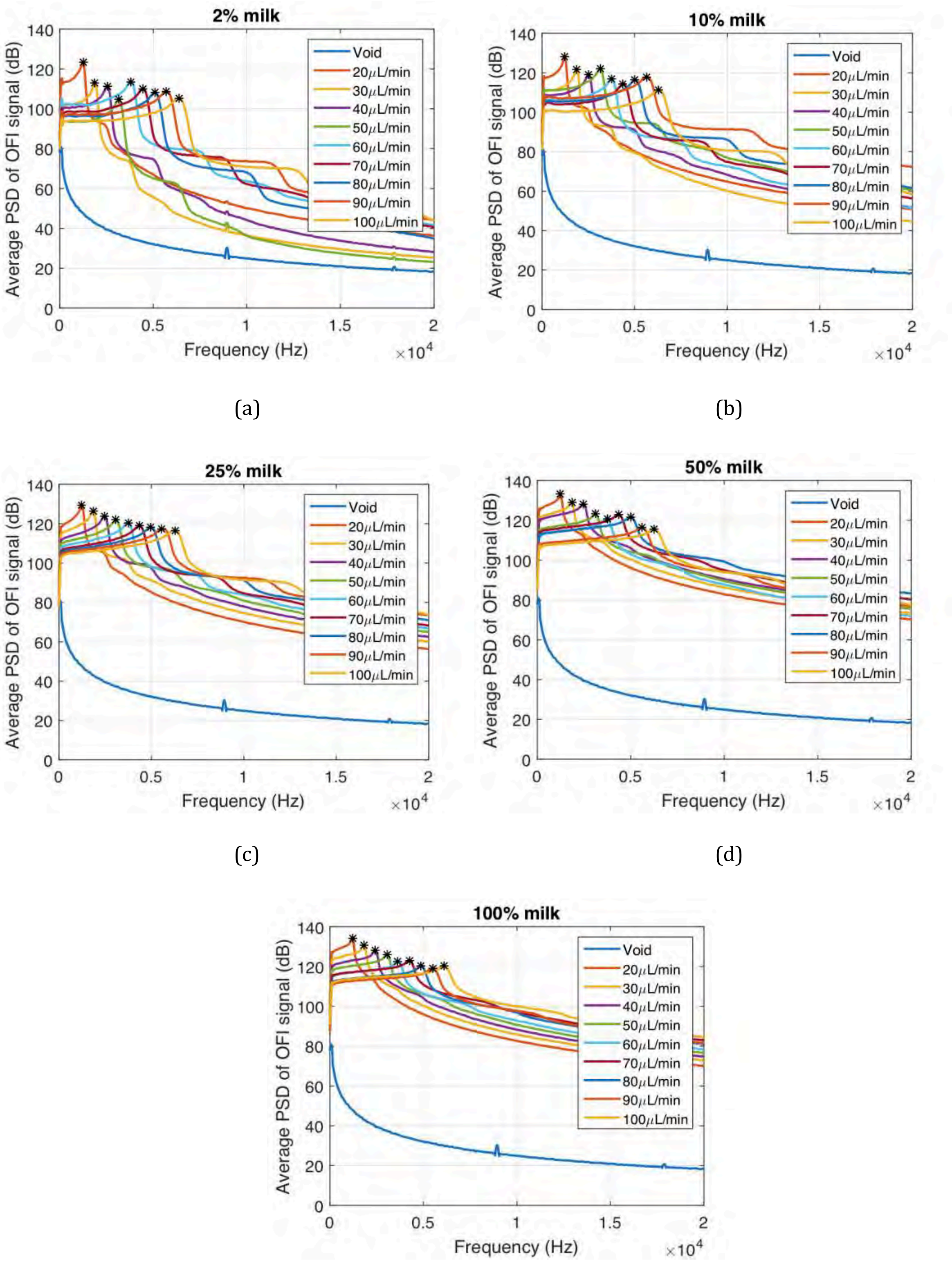

(a) (b) (c) (d) (e)

Fig. 11. Average of computed spectra across all flow rates for (a) 2%, (b) 10%, (c) 25%, (d) 50% and (e) 100% milk, depicted with the most prominent point detected by the algorithm implemented in MATLAB script.

Regarding the validation of the maximum velocity measurements, the Fig.12 shows the results for minimum and maximum milk concentrations across the nine flow rates. The solid green line is traced according the theoretical maximum-to-average velocity ratio, while the values marked by the dots the average of the thirty consecutive measurements obtained by the equation Eq. 2.1 at each flow rate. The error bars represent the standard deviation of these measurements.

The results of the present method fit very properly the linear trend of the expected maximum velocity in all five milk concentrations at all nine flow rates, thus proving that the peak dectection method – when observable – is a valid technique of velocimetry at both single and multiple scattering regimes.

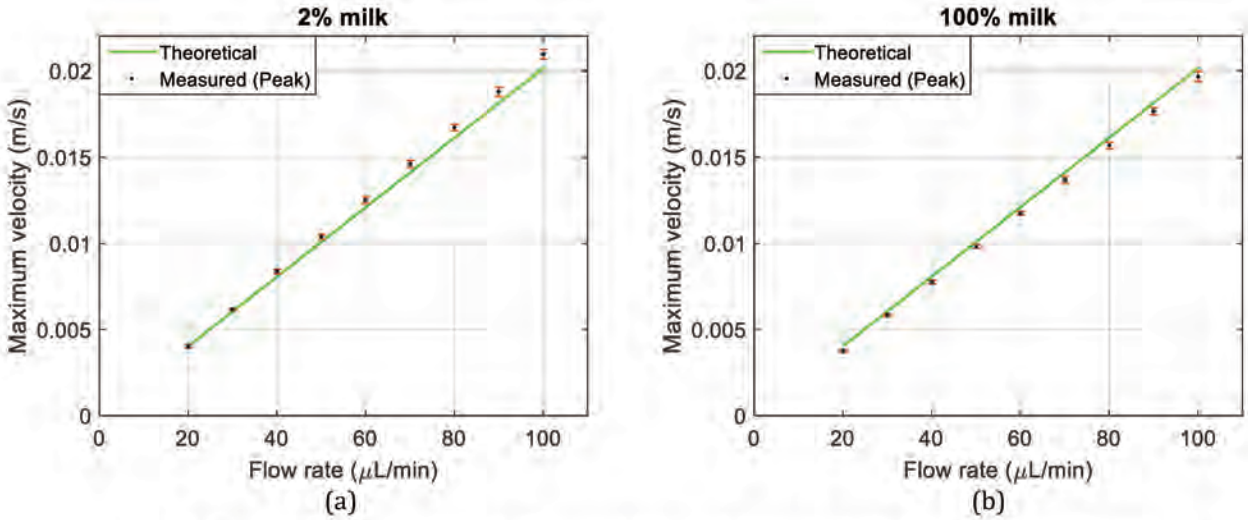

(a) (b)

Fig. 12. Maximum velocities versus the flow rates (the solid green line indicates the expected theoretical values obtained from the maximum-to-average velocity ratio across the nine flow rates) for the (a) 2% and (b) 100% milk concentrations. The dots show the related maximum velocities (v_{max}) calculated by the Eq. 2.1 (with $\theta \approx 81.4°$ obtained from calibration, and f_{Dmax} measured by the maximum Doppler peak frequency detection method). Errors bars indicate the standard deviation from the 30 consecutive measurements.

Fig. 13a reveals the relative error (solid line) and the relative standard deviation (dashed line) as average value from all nine flow rates, across all five milk concentrations. Fig. 13b presents them in same way, but as average from all five milk concentrations, across all nine flow rates. The mean value of relative errors is 1.98%, while the mean value of relative standard deviation is 1.37%.

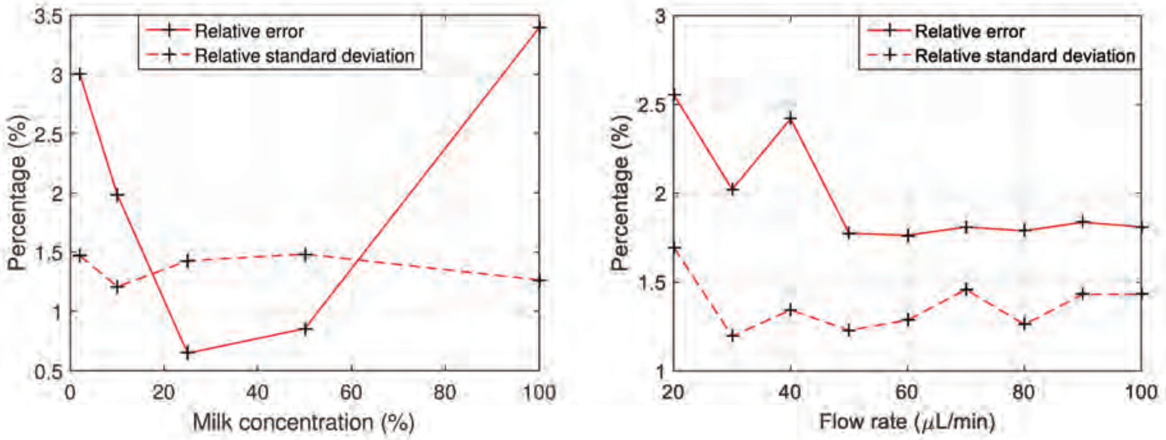

(a) (b)

Fig. 13. Relative error (solid) and relative standard deviation (dashed) related with the expected values from Eq. 2.1 with θ=81.4° (from calibration), (a) versus milk concentration by the average of values obtained from all nine flow rates, and (b) versus flow rate by the mean of measurements of all five concentrations

Moment method

The zeroth order moment is indeed an universal approach to evaluate the spectral energy of the signal, and the first weighted moment is intended to find the average of a distribution of Doppler frequencies. In that way, while the zeroth order moment computation should cover the whole spectrum comprising all amplitudes, an important parameter in the computation of the first weighted moment is the proper definition of the frequency range ($f_{\min}$ and $f_{\max}$), covering only the range of concerned frequencies.

Thus, we should highlight that such spectral truncation plays as a major role in the resulting average frequency. The frequency range chosen was $f_{\min}$ = 0Hz and

$f_{\max}$ = 20kHz, covering the Doppler peak and the two related harmonics for the spectrum corresponding to the highest concentration and flow rate.

As we have already explained, the 1st weighted moment always corresponds to the mean flow velocity in the laser sensing volume. In the double lens configurations the sensing volume is too sharp, so we have observed that the 1st weighted moment becomes an approximation of the Doppler frequency peak, corresponding to a measurement of the maximum flow velocity.

Regarding the validation of the velocity measurements by the Moment method, the Fig. 14 shows the results for the minimum and maximum milk concentrations across the nine flow rates. The solid green line is traced according the expected theoretical values of the maximum Doppler frequencies obtained by the Eq. 2.1, while the values marked by the dots the average of the thirty consecutive measurements obtained by the 1st Moment method at each flow rate. The error bars represent the standard deviation of such measurements. The results of the present method fit mostly a linear trend but with a noticeable deviation from the theoretical maximum Doppler frequencies.

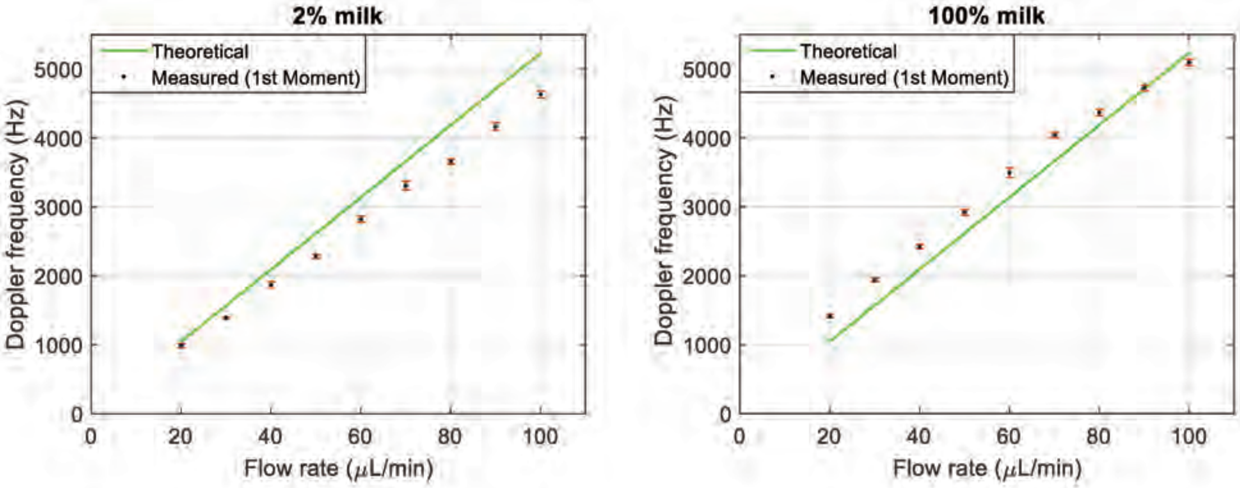

(a) (b)

Fig. 14. Maximum Doppler frequencies versus the flow rates (the solid green line indicates the expected theoretical values for the maximum Doppler frequencies obtained from the Eq. 2.1 across the nine flow rates) for (a) 2% and (b) 100%, milk concentrations. The dots show the related Doppler frequencies measured by the 1st Moment computations. Errors bars indicate the standard deviation from the 30 consecutive measurements.

Figure 15a shows the relative error for the computation without truncation (solid line) and with truncation (dashed line) as average value from all nine flow rates, across all five milk concentrations. Fig. 15b presents them in the same way, but as average from all five milk concentrations, across all nine flow rates. Without truncation the mean value of relative error is 29.52%, while with truncation it lowers to 10.29%.

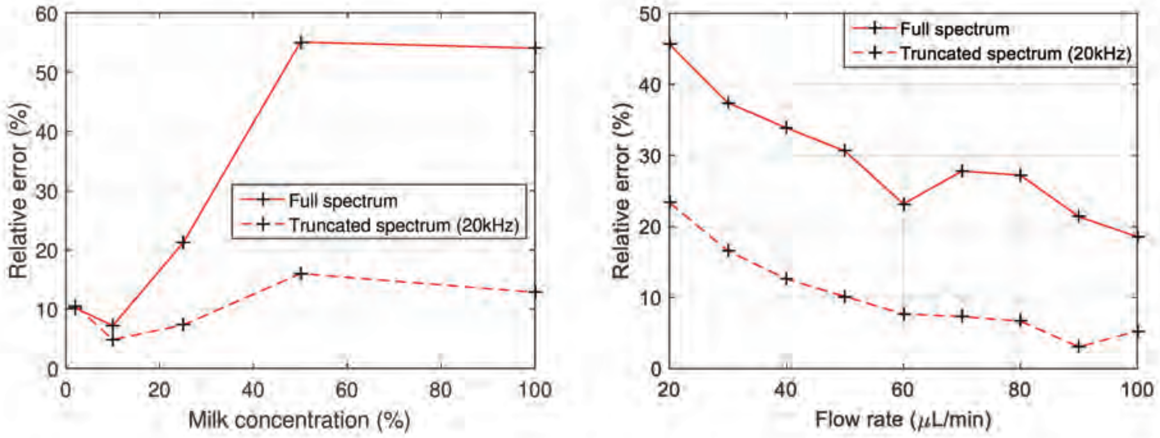

(a) (b)

Fig. 15. Relative error for the computation without truncation (solid) and with truncation (dashed) related with the maximum Doppler frequency values from Eq. 2.1, (a) versus milk concentration by the average of values obtained from all nine flow rates, and (b) versus flow rate by the mean of measurements of all five concentrations.

Figure 16a shows the relative standard deviation for the computation without truncation (solid line) and with truncation (dashed line) as average value from all nine flow rates, across all five milk concentrations. Fig. 16b presents them in same way, but as average from all five milk concentrations, across all nine flow rates. Without truncation the mean value of standard deviation is 3.48%, while with truncation the mean value of relative standard deviation is 1.95%.

In that way, from now on, we will refer to the moment method only with truncation at 20kHz.

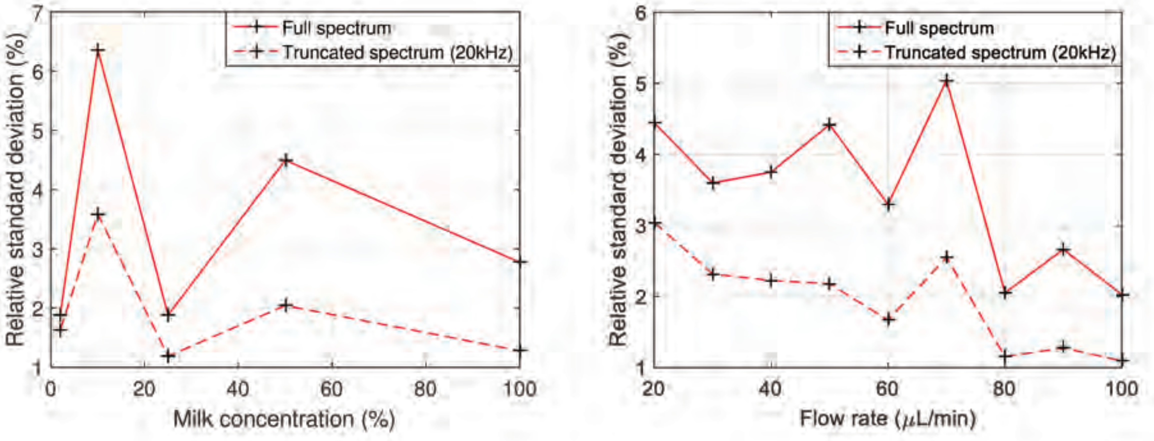

(a) (b)

Fig. 16. Relative standard deviation for the computation without truncation (solid) and with truncation (dashed) related with the maximum Doppler frequency values from Eq. 2.1, (a) versus milk concentration by the average of values obtained from all nine flow rates, and (b) versus flow rate by the mean of measurements of all five concentrations

Discussion

In the present double lens configuration, we have deployed the OFI sensing technique to microfluidics with a novel approach for spectral Doppler peak detection. This implementation is capable to measure the fluid's maximum velocity in a microscale channel with low relative error and standard deviation, at both single and multiple scattering regimes. Although requesting a calibration due to the remaining incertitude on the Doppler angle, this approach allied to the maximum Doppler peak detection method represents a major improvement of robustness regarding the classical singles lens configuration.

The Fig. 17 describes the evolution of the relative error for both signal processing methods: moment and peak, against milk concentrations (Fig. 17a); and against flow rates (Fig. 17b). In all cases the peak method offers smaller error. The mean value of relative errors (over all concentrations and flow rate) is 1.98% with the peak method against 9.01% with the moment method, implicating a degradation by 7.03% when using the moment method.

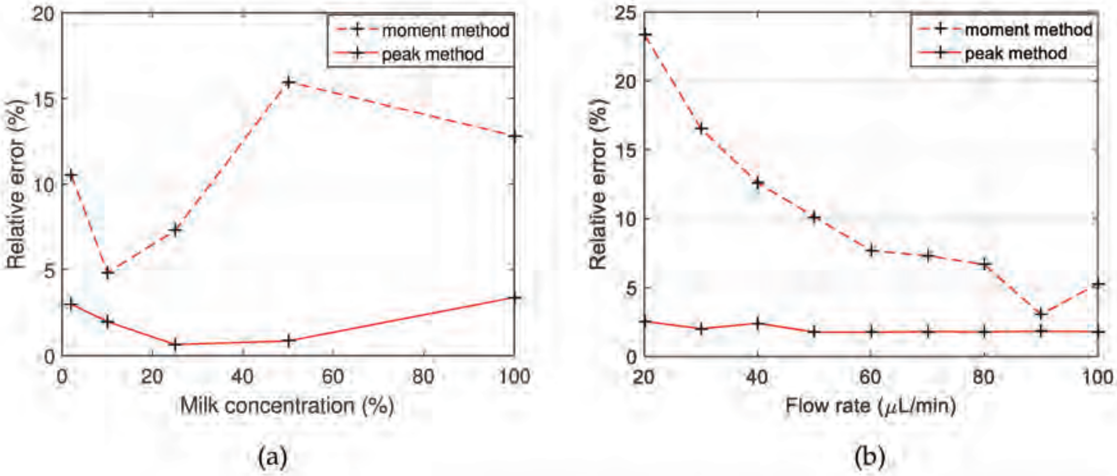

Fig. 17. Relative error of the moment method (dashed line) and peak method (solid line) related with the expected value from equation 2.1. (a) versus milk concentrations by the average of values obtained from all nine flow rates (b) versus flow rate by averaging the values got from all five milk concentrations.

The evaluation of the relative standard deviation for both signal processing methods is shown in the Fig. 18. Fig. 18a presents it against milk concentration, while Fig. 18b against the fluid's flow rate. By them, we realize that the peak method is capable to reach a smaller relative standard deviation in the very most of the cases. The mean value of relative standard deviations is 1.37% with peak method against 1.95% with the moment method, implicating a degradation by 0.58% when using the moment method.

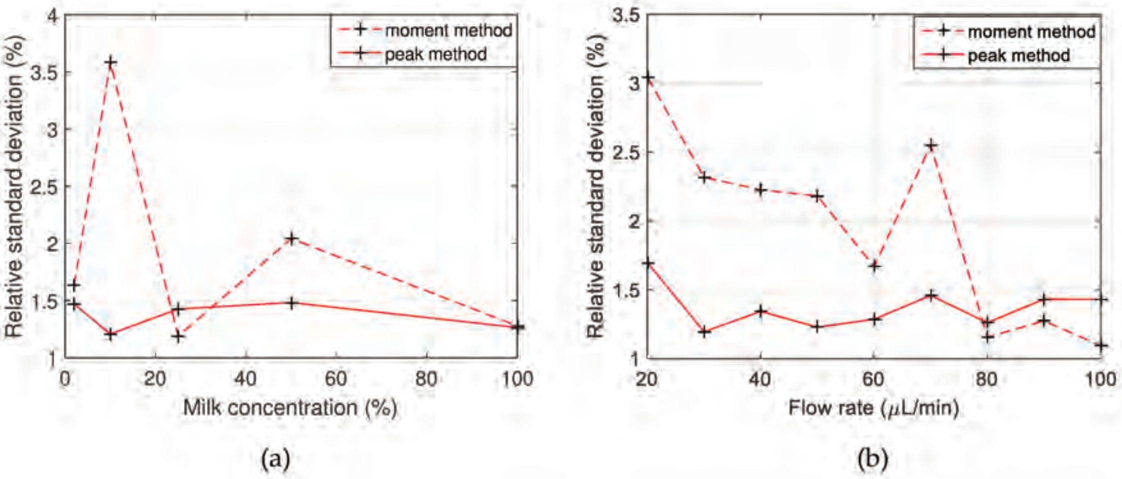

Fig. 18. Relative standard deviation of the moment method (dashed line) and peak method (solid line) related with the expected value from equation 2.1. (a) versus milk concentrations by the average of values obtained from all nine flow rates (b) versus flow rate by averaging the values got from all five milk concentrations.

2.3.4. Double lens with transmission grating

We demonstrate that an improvement of the robustness and reliability of precision Optical Feedback Flowmetry is possible by adding a diffraction grating in the double lens optical configuration.

Authors have presented OFI sensor that uses a use of reflective grating for a displacement sensor with direction discrimination [28] but, to the best of our knowledge it is the first time that a transmission grating is used in an OFI sensing.

Together with a dedicated algorithm for automated evaluation of the flow velocity measuring the maximum Doppler frequency (corresponding to the maximum velocity in the microchannel), the use of the grating improves the robustness of the sensing, mainly by removing the incertitude on the light incidence angle [29]. Allied to the benefits of a double lens configuration, this innovative approach by the grating use also improves the reliability of precision in the velocity measurement, for both single and multiple scattering regimes.

Fig. 19 illustrates the materials used in the OFI sensing experimental setup. The OFI sensor is constituted by the laser diode which includes a monitoring photodiode embedded in-package; a collimating lens (ThorlabsC660TME-C), a near-infrared transmission (NIR) transmission grating (Thorlabs GTI25-03A, 31.7° groove blaze angle, 300 grooves/mm) and a focusing lens (Thorlabs LA1951-C). It is biased by a custom driver that imposes a nominal power of 5 mW.

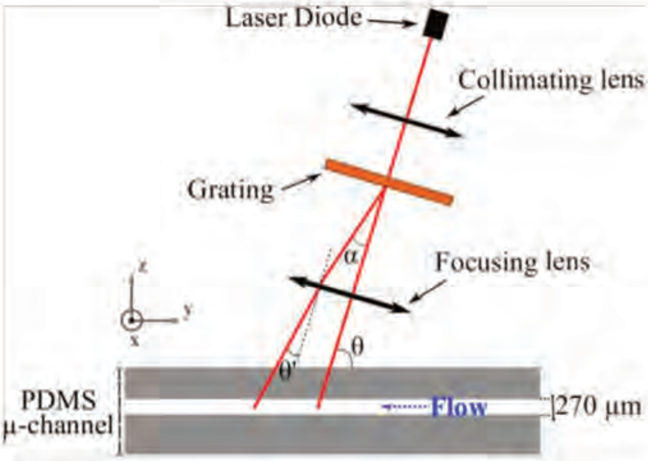

Fig. 19. Principle of operation of the OFI flowmeter including beam separation through transmission gratings.

The experimental incident angle θ was set to 80° with the uncertainty discussed previously. The micro-channel is the PDMS rectangular duct described before. It is fixed horizontally on a Thorlabs PRO1/M high-precision rotation mount that enables (with a resolution of 5 arcmin) to set the channel in good alignment with the line passing through the center of the two laser beams.

As we can see in Eq. 2.1, the relationship between the velocity and Doppler frequency is fully dependent of the fluid refractive index, the laser wavelength and the angle θ. The laser being a monochromatic light source with known or measurable wavelength, and the refractive index of each carrying fluid with a refractometer at the very same laser wavelength; so we can consider the biggest incertitude of measurement comes from θ, which usually is mechanically set in the OFI sensing setup.

Adding a transmission grating in the optical configuration, splits the laser beam in two propagation beams with different propagation directions. This approach, as it shall produce two different Doppler shifts enables velocity measurements that do not require knowledge of the initial incident angle θ.

The grating used here produces two major beams (denoted 0 and +1) of similar power which propagation direction realize an angle θ', while a third beam (-1) propagates with significantly less power. In that way, in our measurement arrangement (Fig. 20), a collimated laser beam passes across the grating and the two induced beams are then focused in the central axis of a flow-channel. In such condition we are able to detect two Doppler peaks in the spectra of the OFI signals.

From Eq. 2.1 and with θ' fixed by the optical configuration, the maximum velocity in the channel can be calculated as follows:

$$f_0 = \frac{2nV_{max}\cos\theta}{\lambda} \ , \tag{2.3}$$

$$f_{+1} = \frac{2nV_{max}\cos(\theta + \theta')}{\lambda} \ , \tag{2.4}$$

thus through the ratio f_{+1}/f_0 :

$$V_{max} = \frac{\lambda f_0}{2n \sin\left[\arctan\left(\frac{\sin\theta'}{\frac{f_{+1}}{f_0} - \cos\theta'}\right)\right]} \ , \tag{2.5}$$

In the first step of the experimental process, the different forward powers ratio for each beam have been measured to be 42% and 29% for the 0 and +1 beams respectively while only 11% was measured for the -1 beam.

Considering the fact of using a transmission grating in an optical feedback configuration is a fully innovative approach, we have performed a characterization setup to measure the feedback powers regarding each diffracted beam. The Fig. 20 illustrates such setup.

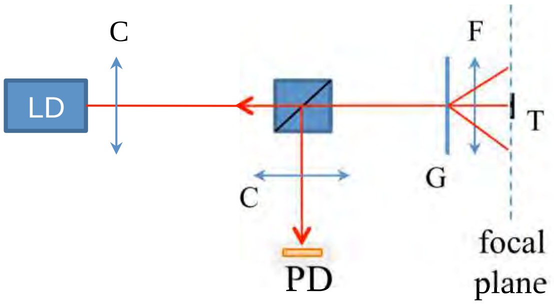

Fig. 20. Experimental setup for the transmission grating characterization regarding the feedback power. (C and F stand respectively for collimating and focusing lens, G for grating, T for target, PD for photodetector)

The 1310nm laser diode (LD), the collimating (C) and focal (F) lens, and the transmission grating (G) are the same ones to be used in the OFI sensor. The target (T) is a reflective tape, and we have set it in a 3-axis linear stage with micrometric step resolution in order to place it on the focal planes of each diffracted beam. We have used a Ge photodetector (PD – Thorlabs SC122) connected to an optical power meter (Thorlabs PM100D) to measure the optical feedback power through a 50:50 1100-1600 nm beam splitter cube (Thorlabs CM1-BS015).

At the nominal lasing power (5 mW), the different feedback powers for each beam have been measured to be 146µW and 11.58µW for the 0 and +1 beams respectively while only 3.25 µW was measured for the -1 beam. So the power ratio between the 0 and +1 beams is ≈20dB.

At the laser wavelength, considering orthogonal incidence on the grating, the related calculated angle α in Fig. 19 is equal to arcsin(λ/3.3µm) = 23.4°. Ray tracing simulations calculated an angle θ' of 11.1°, in good agreement with measurements.

The Fig. 21 shows the average of computed spectra for the five milk concentrations at two different flow rates. The spectrum related to none flow (*void*) is indicated as a reference. The * mark locates the most prominent point corresponding roughly to f_0, while the **x** mark locates the 2nd most prominent point corresponding roughly to f_{+1}. For a constant flow rate, these two points remain stable for the five milk concentrations.

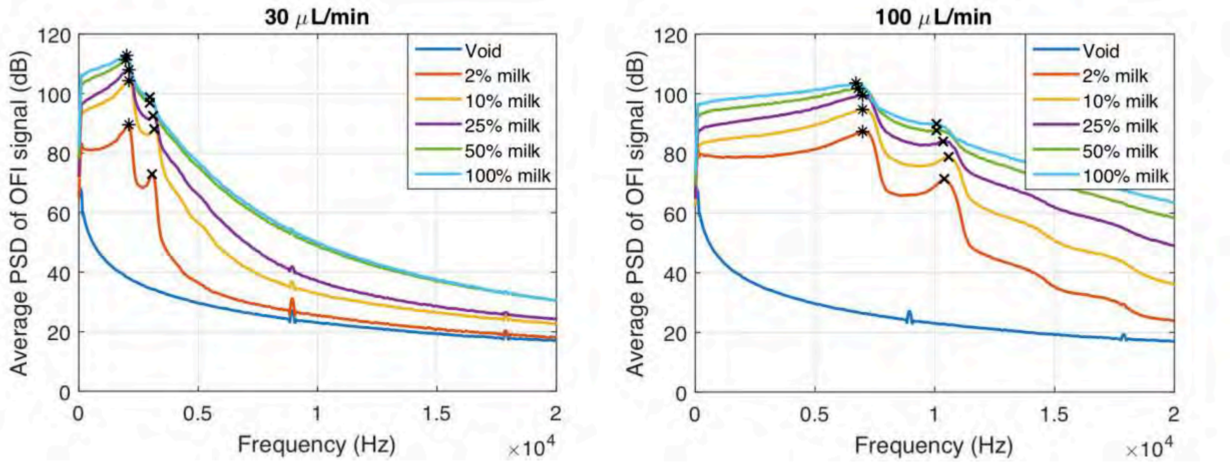

(a)

(b)

Fig. 21. Average of computed spectra at (a) 30 μL/min and (b) 100μL/min for each milk concentration depicted with the 2 most prominent points detected by the algorithm implemented in MATLAB script.

The Fig. 22 depicts the average of computed spectra for all nine flow rates for each milk concentration ratio.

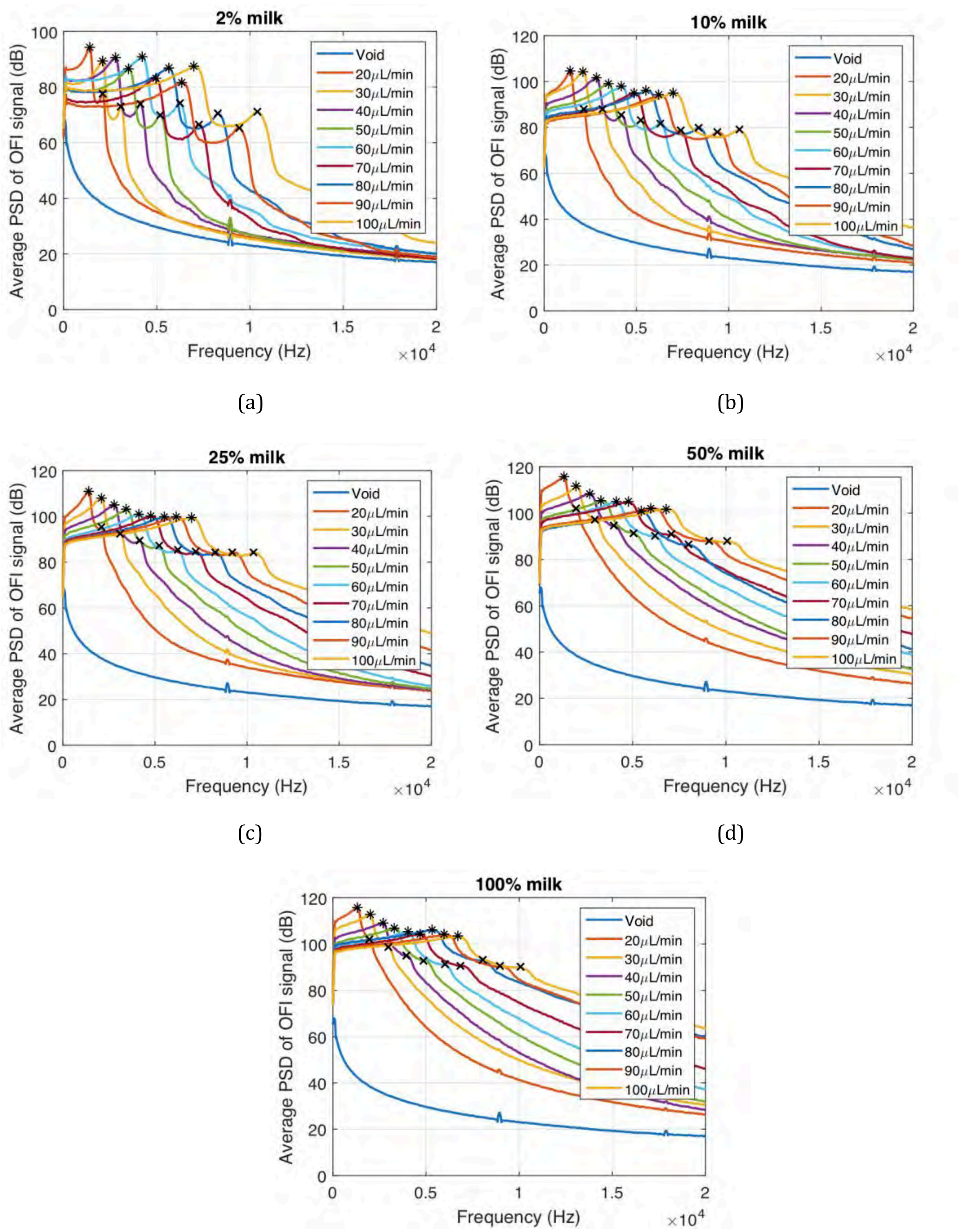

(a) (b) (c) (d) (e)

Fig. 22. Average of computed spectra across all flow rates for (a) 2%, (b) 10% (c) 50% and (d) 100% milk, depicted with the 2 most prominent points detected by the algorithm implemented in MATLAB script.

Peak detection method

Regarding the validation of the maximum velocity measurements by the maximum Doppler peaks detection method, the Fig. 23 shows the results for the minimum and maximum milk concentrations across the nine flow rates. The solid green line is traced according the theoretical maximum-to-average velocity ratio, while the dots indicate the average of the 30 consecutive measurements obtained by the Eq. 2.5 at each flow rate. The error bars represent the standard deviation of such measurements.

The results of the present method fit very properly the linear trend of the maximum velocity in all five milk concentrations at all nine flow rates, what demonstrates the peak detection method in this configuration is an efficient technique of velocimetry at both single and multiple scattering regimes.

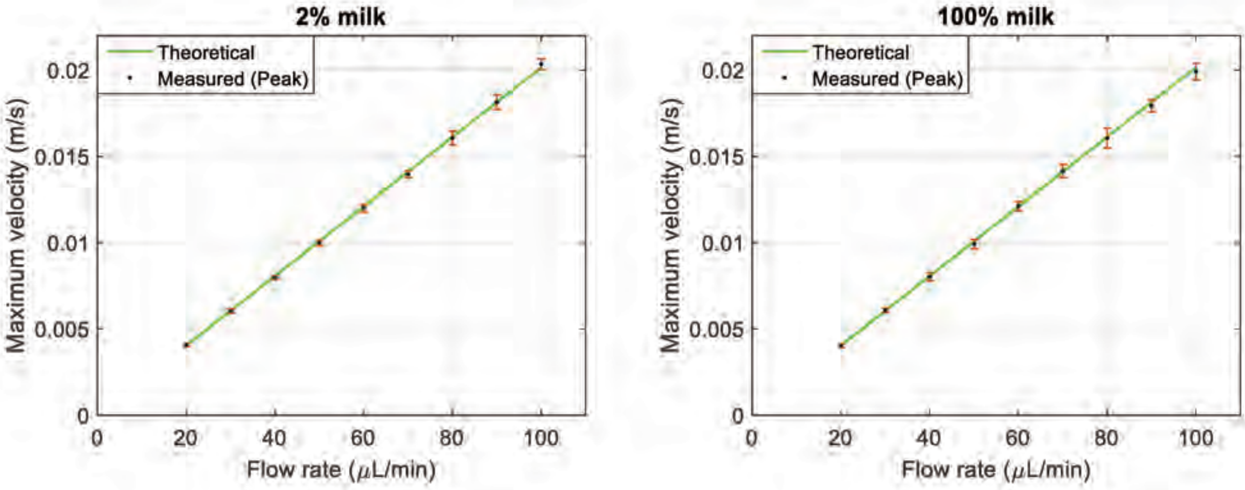

(a) (b)

Fig. 23. Maximum velocity (the solid green line indicates the expected theoretical values obtained from the maximum-to-average velocity ratio) across the nine flow rates for (a) 2% and (b) 100%, milk concentrations. The dots show the related average among the maximum velocities calculated by the Eq. 2.5 (with $\theta' \approx 4.7°$ obtained from grating characterization) at each flow rate. Errors bars indicate the standard deviation from the 30 consecutive measurements.

Fig. 24a reveals the relative error (solid line) and the relative standard deviation (dashed line) as average value from all nine flow rates, across all five milk concentrations. Fig. 24b presents them in same way, but as average from all five milk concentrations, across all nine flow rates. The mean value of relative errors is 0.73%, while the mean value of relative standard deviation is 2.52%.

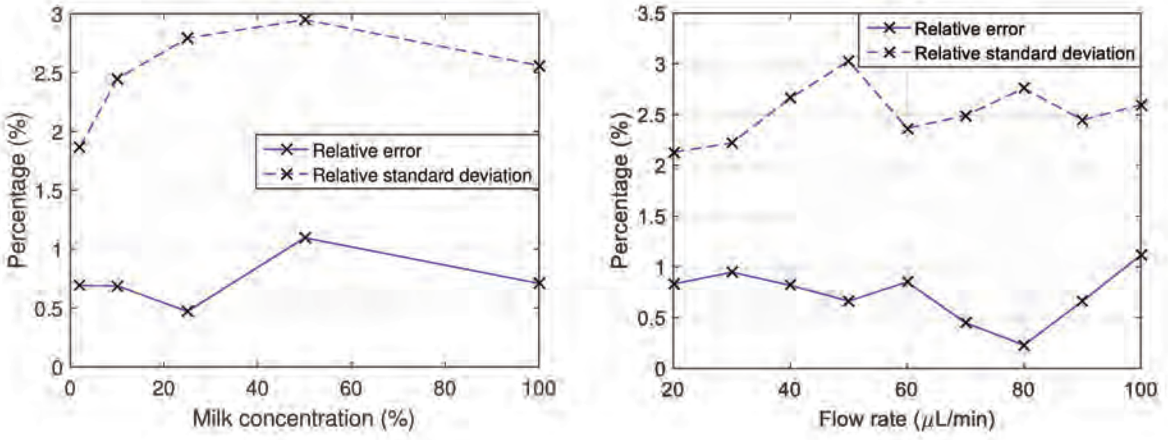

(a) (b)

Fig. 24. Relative error (solid) and relative standard deviation (dashed) related with the expected values from Eq. 2.5 with $\theta' \approx 4.7°$ obtained from grating characterization, (a) versus milk concentration by the average of values obtained from all nine flow rates, and (b) versus flow rate by the mean of measurements of all five concentrations.

Moment method

Regarding the validation of the velocity measurements by the Moment method, we have found that the weighted 1st Moment computation gives us an approximation regarding the 2nd Doppler frequency peak, which corresponds to the maximum velocity related to the optical feedback from the 1st order diffracted beam. The Fig. 25 shows the results for the minimum and maximum milk concentrations across the nine flow rates. The solid green line is traced according the theoretical maximum Doppler frequency corresponding to the 2nd Doppler peak accordingly to Eq. 2.4, while the dots indicate the average of the 30 consecutive measurements obtained by the 1st weighted Moment computation at each flow rate. The error bars represent the standard deviation of such measurements.

Except some increasing absolute deviation directly proportional to the flow rate for 2% milk, the results of the present method fit well the linear trend of the Doppler frequency corresponding to the 2nd Doppler peak in all milk concentrations (with some concerns for full milk as well) at all nine flow rates.

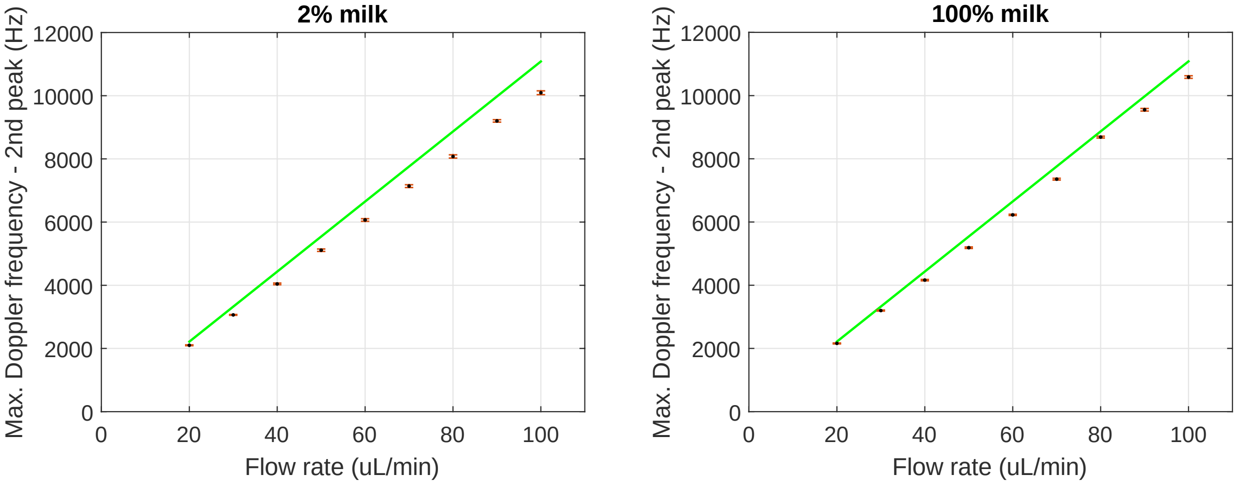

(a) (b)

Fig. 25. Maximum velocity (the solid green line indicates the expected theoretical values obtained from theoretical maximum Doppler frequency corresponding to the 2nd Doppler peak accordingly Eq. 2.4) across the nine flow rates for the five milk concentrations: (a) 2%, (b) 10%, (c) 25%, (d) 50% and (e) 100%. The dots show the related 1st weighted Moment computation at each flow rate. Errors bars indicate the standard deviation from the 30 consecutive measurements.

Fig. 26a reveals the relative error (solid line) and the relative standard deviation (dashed line) as average value from all nine flow rates, across all five milk concentrations. Fig. 26b presents them in same way, but as average from all five milk concentrations, across all nine flow rates. The mean value of relative errors is 3.92%, while the mean value of relative standard deviation is 0.59%.

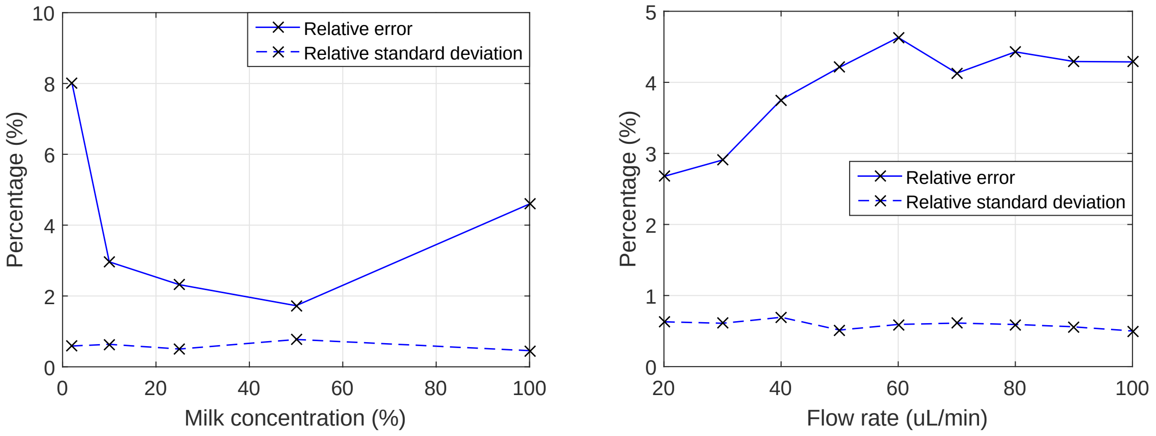

(a) (b)

Fig. 26. Relative error (solid) and relative standard deviation (dashed) related with the expected values from the maximum Doppler frequency regarding the 2nd spectral peak (Eq. 2.4), (a) versus milk concentration by the average of values obtained from all nine flow rates, and (b) versus flow rate by the mean of measurements of all five concentrations

2.4. Conclusion

Among the three optical configurations, the one based on a double lens configuration with a transmission grating is the best one, as allied to the peak detection method it reaches the smallest mean relative error with a workable relative standard deviation since single to multiple scattering regimes. It represents a very new solution to estimate the maximum fluid flow velocity using the Optical Feedback Interferometry sensing technique.

As they present a stable spectral morphology from single to multiple scattering, the double lens configuration and the double lens configuration with grating are more robust than the single lens configuration which spectral morphology tends to change depending on the scatterer concentration.

The table 2.1 indicates the mean relative errors and the mean standard deviations for the Moment and Peak methods from the double lens configurations.

	Double lens configuration		Double lens configuration with grating	
	Moment method	Peak method	Moment method	Peak method
Mean relative standard deviation	1.95 %	1.98 %	0.59 %	2.52 %
Mean relative error	9.01 %	1.37 %	3.92 %	0.73 %

Table 2.1. Mean relative errors and mean relative standard deviations for the Moment and Peak methods from the double lens configuration and from the double lens configuration with grating.

Both optical configurations, together with the peak method, represent very robust techniques in the scope of microfluidics velocimetry, especially because they are able to reach low relative error and standard deviation at the full range, since single to multiple scattering regimes; representing visible improvements regarding the single lens configuration.

Attesting the superiority of the double lens configuration with grating, allied to the peak method as signal processing, the Fig.27 describes the evolution of the relative error against milk concentrations (Fig. 27a), and against flow rates (Fig. 27b).

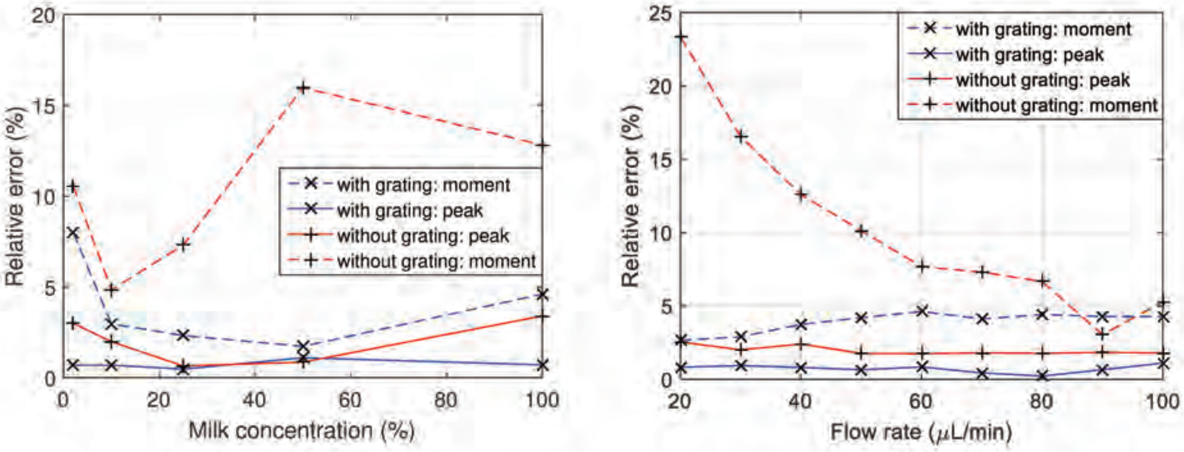

(a) (b)

Fig. 27. Relative error of the setup with grating (blue lines: dashed and solid, for moment and peak methods, respectively) and without grating (red lines: dashed and solid, for moment and peak methods, respectively) related with the expected value from equations 2.5 and 2.1, respectively. (a) versus milk concentrations by the average of values obtained from all nine flow rates (b) versus flow rate by averaging the values got from all five milk concentrations.

The overall evaluation of the relative standard deviation is shown in the Fig.28. Fig. 28a presents it against milk concentration, while Fig. 28b against the fluid's flow rate. The double lens configuration with grating allied to the moment method is capable to reach the smaller relative standard deviation.

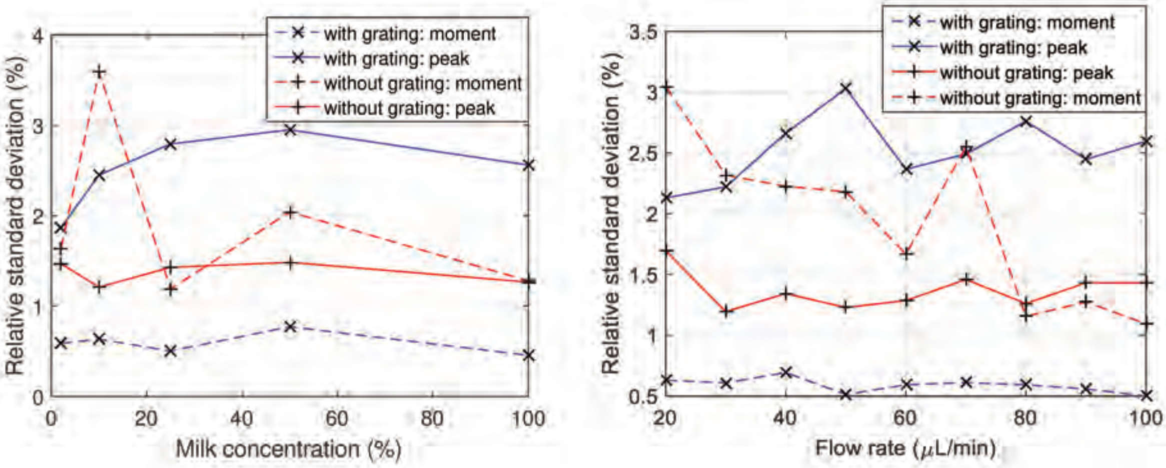

(a) (b)

Fig. 28. Relative standard deviations of the setup with grating (blue lines: dashed and solid, for moment and peak methods, respectively) and without grating (red lines: dashed and solid, for moment and peak methods, respectively) related with the expected value from equations 2.5 and 2.1, respectively. (a) versus milk concentrations by the average of values obtained from all nine flow rates (b) versus flow rate by averaging the values got from all five milk concentrations.

While using the peak method, despite the increasing of the relative standard deviation, besides the important improvement at the relative error, the major additional benefit in using the double lens configuration with grating is that the measurement is not anymore sensitive to any knowledge of the incidence angle.

In a further extension of this study, a custom Binary Optical Elements (BOEs) [40, 41] could be integrated as a top layer over future micro-channel design. Such BOE could replace the focal lens and the grating, and the opportunity of customization could enable the setting of an optimal diffraction angle and eventually improve the feedback power ratio as the usual transmission gratings are designed for forward transmission applications.

Chapter references

1. C. Riva, B. Ross, and G. B. Benedek, Laser Doppler measurements of blood flow in capillary tubes and retinal arteries. *Invest. Ophthalmol.* **1972**, *vol. 11, no. 11*, 936–944.
2. M. D. Stern. In vivo evaluation of microcirculation by coherent light scattering. *Nature*. **1975**, *vol.* 254, *pp.* 56-58.
3. J. Oldengarm, A. H. van Krieken, and H. W. van der Klooster. Velocity profile measurements in a liquid film flow using the laser Doppler technique. *Journal of Physics E: Scientific Instruments*. **1975**, *vol.* 8, *no.* 3.
4. A. P. Shepherd, P. A. Oberg. Laser-Doppler Blood Flowmetry; Springer, **1990**, ISBN: 9781441947451. 10.1007/978-1-4757-2083-9.
5. G. Michelson, B. Schmauss. Two-dimensional mapping of the perfusion of the retina and optic nerve head. *British Journal of Ophthalmology*. **1995**, *vol.* 79, *pp.* 1126-1132.
6. J. D. Briers. Laser doppler, speckle and related techniques for blood perfusion mapping and imaging. *Physiological Measurement*. **2001**, *vol.* 22, *pp.* R35-R66.
7. I. Fredriksson, C. Fors and J. Johansson. Laser Doppler Flowmetry - a Theoretical Framework. Depart. of Biomed. Eng., Linköping University. **2007**.
8. V. Rajan, B. Varghese, T. G. van Leeuwen, et al. Review of methodological developments in laser Doppler flowmetry. *Lasers Med. Sci.***2009**, *vol.* 24, *no.* 2, *pp.* 269-283. 10.1007/s10103-007-0524-0.
9. E. E. Ramirez-Miquet, Implementation of Optical Feedback Interferometry for Sensing Applications in Fluidic Systems. PhD thesis, Université de Toulouse, France, September 29th, 2016.
10. L. Campagnolo, M. Nikolić, J. Perchoux, et al. Flow profile measurement in microchannel using the optical feedback interferometry sensing technique. *Microfluid Nanofluid*. **2013**, *vol.* 14, pp. 113-119, 10.1007/s10404-012-1029-0.
11. S. Donati, and M. Norgia, Self-mixing interferometry for biomedical signal sensing, *IEEE J Selec. Top. Quantom Elec.*,**2014**, *Vol 20 no. 2*.
12. F. de Mul, M. Koelink, A Weijers, J. Greve, J. Aarnoudse, R. Graaff, A Dassel, Self-mixing laser-doppler velocimetry of liquid flow and of blood perfusion in tissue, *Appl. Opt.***1992**, *vol. 31 issue 27*, 5844–5851, 10.1364/AO.31.005844.
13. F. F. M. de Mul, M. H. Koelink, A. L. Weijers, J. Greve, J. G. Aarnoudse, R. Graaff, and A. C. M. Dassel. A semiconductor laser used for direct measurement of the blood perfusion of tissue.*IEEE transactions on biomedical engineering*. **1993**, *vol.* 40, *no.* 2.
14. R. Bonner and R. Nossal. Model for laser Doppler measurements of blood flow in tissue, *Appl. Opt.***1981**, *vol.* 20, *pp.* 2097-2107.
15. C. Zakian and M. Dickinson. Laser Doppler imaging through tissues phantoms by using self-mixing interferometry with a laser diode. *Applied Optics*. **2007**, *vol.* 32, *no.* 19.
16. J. R. Tucker, J. L. Baque, Y. L. Lim, A. V. Zvyagin, and A. D. Rakic. Parallel self-mixing imaging system based on an array of vertical-cavity surface-emitting lasers.*Applied Optics*.**2007**, *vol.* 46, *no.* 25.
17. M. Norgia, A. Pesatori, and L. Rovati. Optical Flowmeter for Blood Extracorporeal Circulators. *IEEE*. **2009**, 10.1109/IMTC.2009.5168741.
18. M. Norgia, A. Pesatori, and L. Rovati. Self-mixing Laser Doppler: a Model for Extracorporeal Blood Flow Measurement.*IEEE*, **2010**.
19. E. E. Ramírez-Miquet, J. Perchoux, R. da Costa Moreira, R., Y. Zhao, A. Luna-Arriaga, C. Tronche, and O. Sotolongo-Costa. Optical Feedback Interferometry: from Basics to Applications of Laser Flowmetry. RevistaCubana de Física [Online], **2017**, *vol.* 34, *no.* 1, *pp.* 48-57.

20. R. Atashkhooei, E. E. Ramírez-Miquet, R. da Costa Moreira, A. Quotb, S. Royo and J. Perchoux. Optical Feedback Flowmetry: Impact of Particle Concentration on the Signal Processing Method. *IEEE Sensors Journal.* **2018**, *vol.* 18, *no.* 4, *pp.* 1457-1463.10.1109/JSEN.2017.2781902
21. M. Nikolić, D. P. Jovanović, Y. L. Lim, K. Bertling, T. Taimre, and A. D. Rakić. Approach to frequency estimation in self-mixing interferometry: Multiple signal classification. *Appl. Opt.***2013**, *vol.* 52, *no.* 14, *pp.* 3345–3350.
22. M. Nikolić, Y. L. Lim, K. Bertling, T. Taimre, and A. D. Rakić. Multiple signal classification for self-mixing flowmetry. *Appl. Opt.***2015**, *vol.* 54, *pp.* 2193-2198.
23. L. CAMPAGNOLO, Optical feedback interferometry sensing technique for flow measurements in microchannels. PhD thesis, Université de Toulouse, France, February 12th, **2013**.
24. A. Mowla et al. Effect of the optical system on the Doppler spectrumin laser-feedback interferometry. *Appl. Opt.***2015**, *vol.* 54, *no.* 1, *pp.* 18–26.
25. C. Zakian, M. Dickinson and T. King. Particle sizing and flow measurement using self-mixing interferometry with a laser diode. *Journal of Optics A: Pure and Applied Optics*. **2005**, *vol.* 7, *no.*6.
26. C. M. Zakian, M. R. Dickinson. Flow measurements through scattering samples using self-mixing interferometry with a laser diode.*Proc. SPIE, Biophotonics and New Therapy Frontiers*. **2006**, *vol.* 6191. 10.1117/12.662518.
27. S. Sudo, Y. Miyasaka, K. Nemoto, K. Kamikariya, and K. Otsuka. Detection of small particles in fluid flow using a self-mixing laser.*Opt. Express*. **2007**, *vol.* 15, *pp.* 8135-8145.
28. D. Guo, M. Wang, and H. Hao. Self-mixing grating interferometer: theoretical analysis and experimental observations. Proc. SPIE, Interferometry XVIII. **2016**, *vol.* 9960. 10.1117/12.2239519.
29. W. Huang, H. Gui, L. Lu, J. Xie, H. Ming, D. He, H. Wang, and T. Zhao. Effect of angle of incidence on self-mixing laser dopplervelocimeter and optimization of the system. *Optics Communications*. **2007**, *vol.* 281, *pp.* 1662-1667.
30. J. Perchoux, A. Quotb, R. Atashkhooei, F.J. Azcona, E.E. Ramírez-Miquet, O. Bernal, A. Jha, A. Luna-Arriaga, C. Yanez, J. Caum, T. Bosch, and S.Royo. Current Developments on Optical Feedback Interferometry as an All-Optical Sensor for Biomedical Applications. Sensors. **2016**, *vol.* 16, *issue* 5, *article* 694, 10.3390/s16050694.
31. L. Rovati, S. Cattini, and N. Palanisamy. Measurement of the fluid velocity profile using a self-mixing superluminescent diode. *Meas. Sci. Tech.***2011**, *vol.*22, *no.* 2.
32. L. Campagnolo, S. Roman, J. Perchoux and S. Lorthois. A new optical feedback interferometer for measuring red blood cell velocity distributions in individual capillaries: a feasibility study in microchannels. Computer Methods in Biomechanics and Biomedical Engineering. **2012**, *vol.* 15, *no. sup.* 1, *pp.* 104-105. 10.1080/10255842.2012.713651.
33. T. Binzoni, A. Torricelli, R. Giust, B. Sanguinetti, P. Bernhard, and L. Spinelli. Bone tissue phantoms for optical flow meters at large interrupted spacing generated by 3D-stereolithography. *Biomed. Opt. Express.* **2014**, *vol.*5, *pp.* 2715-2725.
34. R. Lohwasser and G. Soelkner. Experimental and theoretical laser-Doppler frequency spectra of a tissue like model of a human head with capillaries. *Appl. Opt.***1999**, *vol.*38, *pp.* 2128-2137.
35. N. Sundararajan, M. S. Pio, L. P. Lee and A. A. Berlin. Three-dimensional hydrodynamic focusing in polydimethylsiloxane (PDMS) microchannels. *Journal of Microelectromechanical Systems*. **2004**, *vol.* 13, *no.* 4, *pp.* 559-567.10.1109/JMEMS.2004.832196
36. J. A. Schetz and A. E. Fuhs. *Fundamentals of fluid mechanics*. Wiley. **1999**. ISBN: 9780471348566.
37. S. Kakac, R. K. Shah, and W. Aung, *Handbook of Single Phase Convective Heat Transfer*, Wiley. **1987**, ISBN: 9780471817024.
38. W. M. Kays, M. E. Crawford. Convective heat and mass transfer. McGraw-Hill. 1993, ISBN: 9780070337213.

39. R. K. Shah and A. L. London. *Laminar flow forced convection in ducts*. Academic Press. **1978**, ch. VII, *pp.* 197-198, *eqs.* 335-338. ISBN: 9781483191300.
40. J. Zhao and Z. You. Using binary optical elements (BOEs) to generate rectangular spots for illumination in micro flow cytometer. *Biomicrofluidics*, 2016, *vol. 10*, p. 054111. 10.1063/1.4963010
41. J. Zhao and Z. You. Combining Microfluidic Chip and Binary Optical Element for Flow Cytometry, Proceedings of IEEE SENSORS 2016, Orlando, FL, USA. 30 Oct.-3 Nov. 2016.10.1109/ICSENS.2016.7808676.

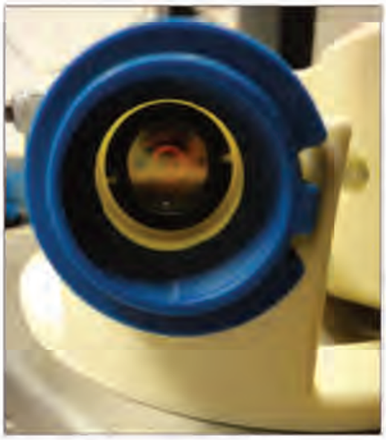

CHAPTER 3 : OFI 2D Doppler imagers

3.1. Context

High resolution velocimetry imaging is of high importance for many applications in the microfluidics field.

The existing velocimetry technologies based on the Doppler effect (*Laser Doppler Velocimetry, Planar Doppler Velocimetry, Optical Doppler Coherence Tomography, Ultrasound*) or imaging (*Particle Tracking Velocimetry, Particle Image Velocimetry, Micro-Particle Image Velocimetry, Dual-slit method*) techniques are bulky, complex and high-cost.

Taking advantage of the features of the OFI technology, some initial OFI scanning solutions [1-4] have been proposed where the scanning system is usually done by moving the whole OFI sensing system (optics and electronics) across two orthogonal directions. As we will see in our implementation of this approach introduced here, such technique provides good results, but the scanning time and the compactness have to be revised due to the big and heavy mechanical systems that are deployed. Also, these implementations have been limited to laboratory demonstration on mechanically damped optical tables. Then they require not only an important physical space, but also a long scanning time as the movement of the whole system usually includes a considerable time of steadiness between each acquisition (each pixel) in order to avoid too unwanted interferences related to the mechanical movement.

In the perspective to overcome these issues, we present a new embedded OFI Doppler flow imager that has been realized using a 2-axis beam-steering mirror mounted on a Micro-Electro-Mechanical System (MEMS), thus taking the full advantage of the compactness offered by the OFI sensing scheme. The great novelty of this latest solution is the use of a fast and steady MEMS mirror for 2D scanning. The compactness of the MEMS mirror allows designing an embedded imaging system in a compact handheld case that provides quantitative information about the velocity on fluids at the micro-scale. The system developed during this PhD is able to reach a spatial imaging resolution up to 5 µm.

The main objective of the imaging systems designed in this study concerns the Doppler flowmetry for biomedical application, especially related to microvascular researches. In particular, the MEMS based version was designed in the context of the Diagnoptics project (sponsored by the European Commission), dedicated to provide an innovative non-invasive technique in the diagnosis of skin cancer through the fusion of several imaging methods (multi-spectral, 3D photography and OFI Doppler imaging). The purpose of the OFI Doppler imager was then the imaging of subcutaneous blood vascularization in the vicinity of the lesion.

The goal is to obtain a quantitative information related to the blood perfusion beneath a skin tumor. According to the dermatologists specialized in the skin cancer diagnosis, the malignancy of a tumor is reflected by an increasing in its surrounding vascularization (Angiogenesis). For example, there are twice as many blood vessels in a primary malignant melanoma than in a benign one [5, 6] (*Fig. 1).* In that way, this equipment could assist the doctors in a more precise and precocious diagnosis before an excision decision, supplying the practitioner with significant information to discern the nature of the skin tumor.

Fig. 1. Illustration of the vascularization beneath a malignant melanoma.

Assessing information about the blood flow beneath a skin tumor looking for a prognosis using an OFI imager, the main concern is the low level of backscattered light as the skin diffuses the light, thus deviating most of the backscattered light away from the original optical path. In other words, a photon is not directly reflected by a single particle in the flow but suffers from multiple reflections in the amorphous medium before being re-injected into the laser cavity. Moreover, the particle (Red Blood Cells – RBC – and others) density in human blood is high enough so that the multiple scattering regime arises (*id est* several Doppler shifts due to consecutive scatterings by particles occurs for a single photon). In that way, the acquired OFI signal includes a whole spectrum of frequencies (spread Doppler frequency shift) from which the determination of the flow is complex to obtain (see Chapter 2).

Also, beyond that, the complexity to achieve a stable enough *in vivo* sample is a real challenge, which comprises the coherent sensing capability. In short, while dealing with *in vivo* measurements, several instabilities arise affecting the measurement conditions. The main cause of signal disturbance comes from the fact that an OFI sensor is very sensible to variations in the sensor-target distance (*id est*, the external laser's cavity length, from the three-mirror model) that induce undesired fringes to the Doppler ones generated by the blood flow. Despite the efforts to limit unwanted movements, a previous signal conditioning is required for an appropriate signal processing.

The signal processing implemented to exploit the sensing information has been based on the spectral analysis of OFI signals in the case of the multiple scattering regime. The average Doppler frequency ($\overline{f_D}$) is derived from the 1st weighted moment (see Chapter 2 and [7-12]) as

$$\overline{f_D} = \frac{M_1}{M_0} = \frac{\int_{fmin}^{fmax} f.P(f)df}{\int_{fmin}^{fmax} P(f)df}\,, \qquad (3.1)$$

Where M_1 is the 1st order moment; M_0 is the 0th order moment; f_{min} and f_{max} set the spectral frequency range; and $P(f)$ is the amplitude of the power spectral density (PSD). Also, the raw moment of 0th and 1st order have been used as a parameter to discriminate high vascularisation densities from lower ones.

In order to demonstrate the feasibility of blood flow measurements *in vivo* our very first *in vivo* trial [13] was performed over an optical table for two different skin areas of each of the individuals that agreed to serve as “guinea pig” (GP). One of the areas is said “irritated”, and the other one is qualified as “normal”, both are located on the GP forearms. The irritation is realized by the application of a camphor-based cream that enhance the vascularization in less than 5 min and for roughly 30 minutes. The camphor cream causes localized vasodilatation (giving a feeling of warmth) and after a few minutes, it is possible to visually observe that the skin looks redder (see *Fig. 2*).

The laser was chosen for being suitable for such OFI sensor intended to biomedical application. It is a DFB laser diode (Mitsubishi ML725B11), which wavelength (1310 nm) at the nominal power (5 mW) is considered human eye safe. Regarding the optical configuration, only a single lens is used to focus the laser beam.

The optical feedback signal is obtained through the built-in photodiode current, which is first amplified by a transimpedance amplifier (gain 105dB), and then filtered with a bandpass filter [40Hz, 80kHz] to improve the SNR. It is then fed through a DAC card (NI USB-6251) as the OFI signal for analysis in a PC using Matlab scripts.

Four different people have volunteered as GP. For each area and each GP, the M_0 was calculated over one acquisition performed at a fixed position. The results show that, even if the M_0 value varies among the 4 persons, we obtain always a higher value for the irritated area as compared to the not treated area of the same person.

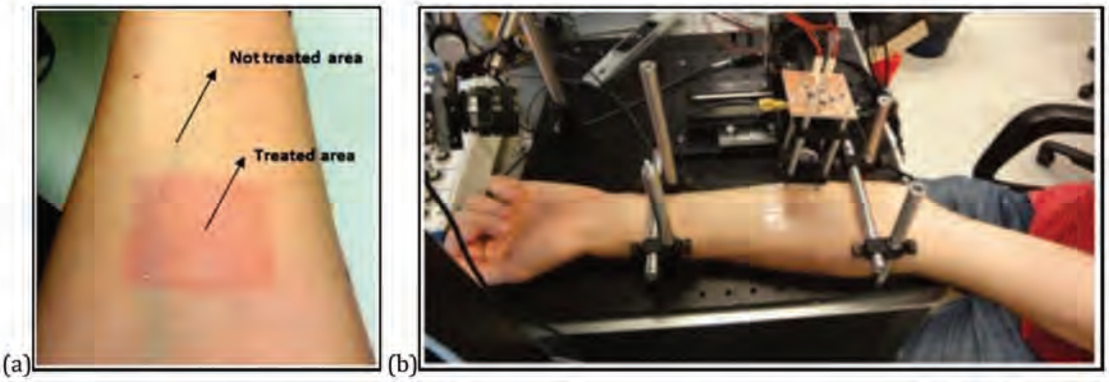

Fig. 2. (a) Photography showing the vascularization enhancement in the red area, due to the application of a camphor-based cream. [13] (b) Photography of the experimental setup over an optical table. [13]

The results of this study have been the base of the first device that was used in the context of the Diagnoptics project. We have designed a one-point sensor for the observation of skin vascularization that was tested on actual patients of the Hospital Clinic of Barcelona. The device presented in *Fig. 3* embeds all the technical features of the one tested on table, in a compact packaging with batteries allowing for handheld operation with a trigger button for the acquisition. A very basic image (3 x 3 pixels) has been realized by the practitioner in a jointly defined protocol.

Fig. 3. Handheld part of the 1-shot OFI system for single point acquisition.

As the OFI sensors have shown encouraging results for flowmetry in microfluidics, the next step of the project has been to design a functional prototype of a 2D imager of the blood flow in a human skin.

3.2. Translation stages scanning system

The scanning system used in the initial researches of our microfluidics group had been based in the use of a 2 or 3-axis linear translation stage (Zaber Tech.) with a micrometric displacement accuracy.

In this approach, the whole OFI sensing system (optics and electronics) is mechanically hold in the Zaber translation mount and set on an optical table.

The sensor used in this study is the single point OFI that depicted previously (*Fig. 3*). It is assembled with the two translation stages (ZaberTech. T-LSM050A and T-LSM100A) displayed orthogonally as shown in *Fig. 4*. The control of the translation stage movements is implemented in the Labview VI that manage the acquisition.

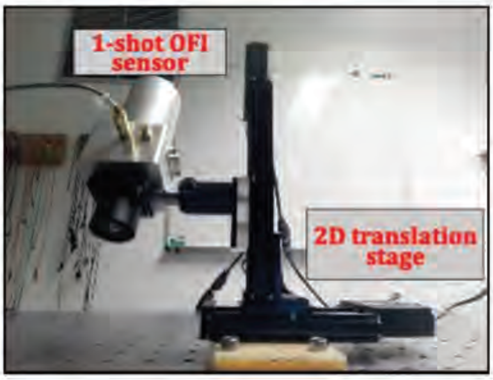

Fig. 4. Photography of the 2D scanning OFI setup over an optical table.

The purpose of this intermediary step towards the embedded 2D scanning system was to determine the specific issues arising while producing an image from the single point OFI measurement system. The main parameter that impact the measurement quality is the inertia of the moving object which induce vibration type fringes in the OFI signal. Thus, an interval is set after the end of each step displacement and before the related OFI signal acquisition. However, this delay highly increases the scanning time and after empirical tests the minimum feasible value of 500 ms for the waiting time has been considered as a fair trade-off hopping that the use of the MEMs mirror will help improving this parameter.

However, contrary to the single point OFI measurement, the 2D imager cannot be in direct contact with the patient skin and the patient movement induces external cavity variations that produce interferences in the sensor signal. It has been necessary to develop an algorithm for signal conditioning. It is described in *Fig. 5*.

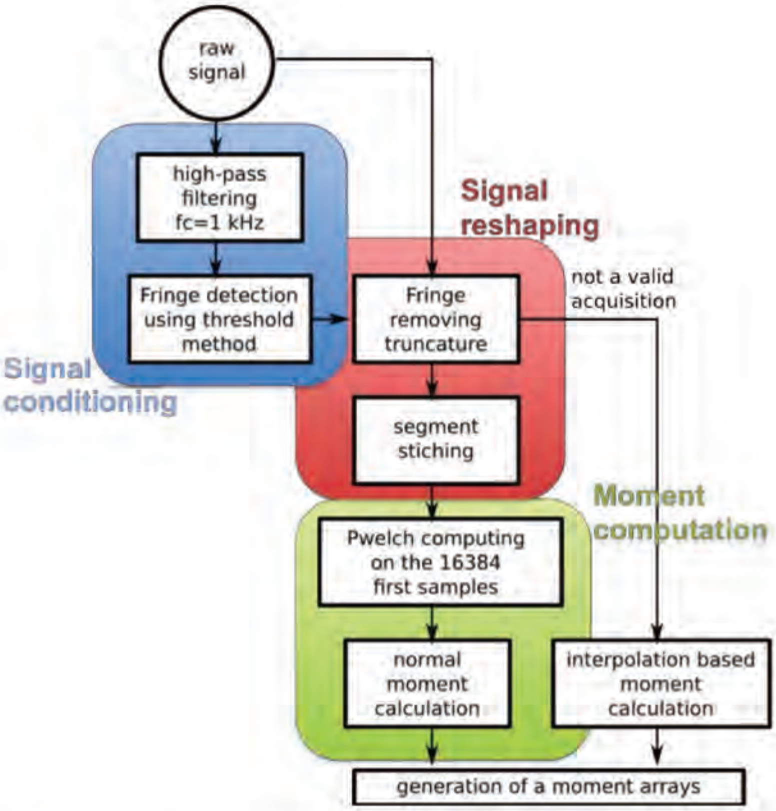

Fig.5. Block diagram of signal conditioning and processing for *in vivo* raw data.

Once the raw data from the scanning is acquired, the signal conditioning algorithm is performed, pixel by pixel. Firstly, the raw data is filtered with a high-pass filter with cut-off frequency, set to 1 kHz, removes the stronger low frequency disturbances (most of the energy of the vibration induced fringes). The remaining fringes are directly eliminated using an amplitude threshold on the filtered signal. Each time the signal amplitude gets higher than the threshold (as illustrated by *Fig. 6*), a segment of a fixed number of samples before and after the violation are removed and the signal is reconstructed by stitching the remaining segments by forcing the first value after and the last before the removed part to be equal. This "stiching" limits the presence of high frequency energy in the spectrum. *Fig. 6* presents the raw signal and the filtered signal with the threshold. The gray zone are the ones to be removed and only the white ones are kept.

In cases the unwanted fringes would completely pollute the signal, a fixed minimum number of samples is set at 16384 remaining samples and for further estimation of the moment, all conditioned acquisitions are truncated to have 16384 samples only. In case a pixel data is too strongly affected by vibrations, if it has less than 16384 remaining samples, it is not considered. In that case, the Moment values of such pixel will be obtained by averaging the values of the previous and following pixels.

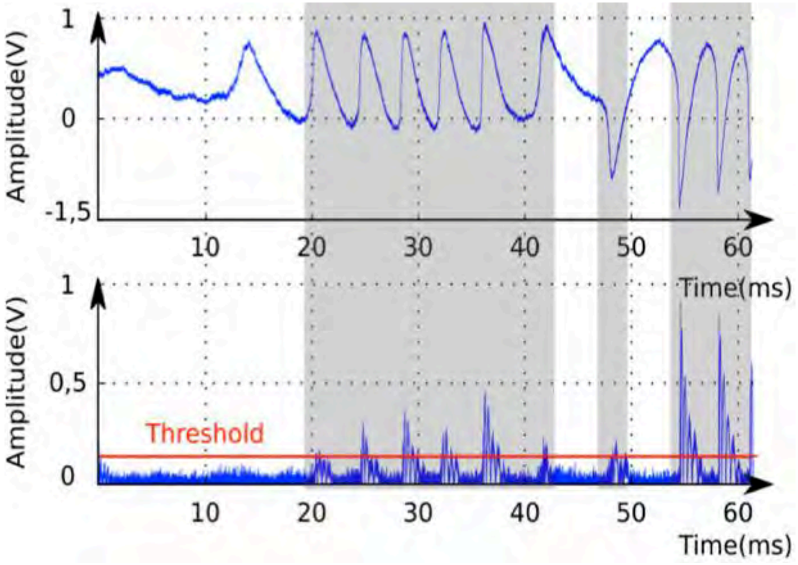

Fig. 6. An example of 61440 samples acquired at 1MHz sampling rate for 1 pixel presenting strong vibrations that cross the threshold after filtering. Raw data (graph above), filtered data by 1kHz high-pass filter (graph below) and amplitude threshold (red line) The gray zones correspond to the samples to be eliminated due to the signal conditioning.

Both the high pass filter cut-off frequency and the threshold values were estimated empirically. The threshold value depends principally on the signal amplitude and so on the feedback level. This one being very variable from a laser to another and from a patient to the other, eventually it will have to be optimized according the experimental conditions.

Several validations *ex vivo* and *in vivo* were performed. In *Fig. 7*, four-line rasterizations (100 pixels, with 75 µm of scanning resolution) starting at different points have been performed. Through the results, based on the computation of the 1st Moment in the range of 2-22kHz, parabolic flow profiles (*Fig. 7b, 7c* and *7d*) suggest the vein presence, which is not the case for *Fig. 7e*.

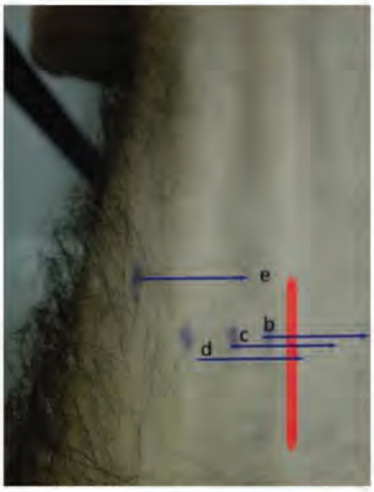

(a)

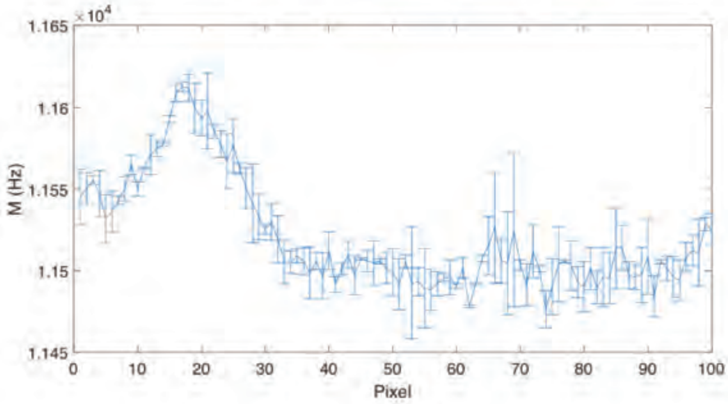

(b)

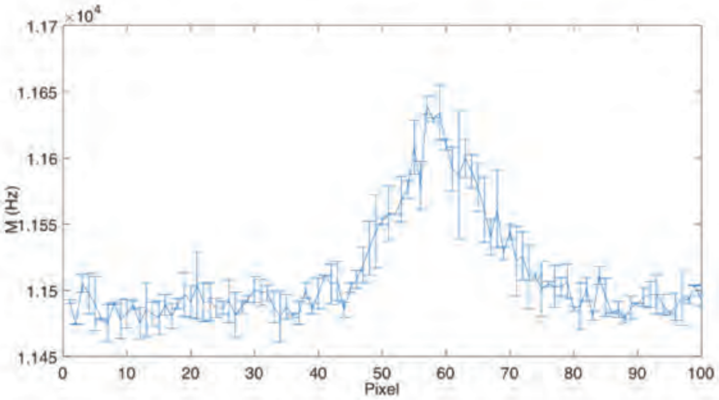

(c)

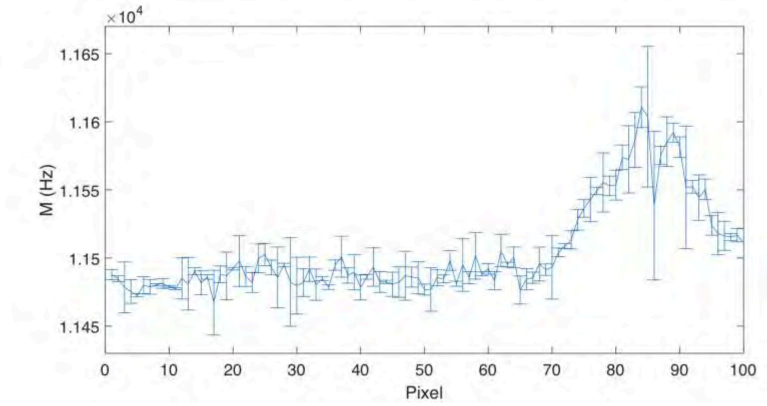

(d)

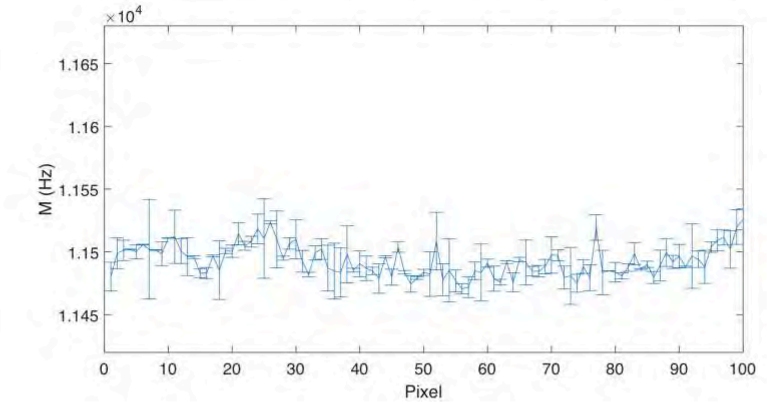

(e)

Fig. 7. Four linear rasterizations around a superficial radic vein visible by naked eye. (a) The four scanned zones are roughly delimited by arrows with letters corresponding respectively to the 1st Moment graphs: (b), (c), (d) and (e). In (b), (c) and (d) parabolic flow profiles suggests the vein presence, while in (e) the scanned zone is apparently away the vein presence.

In *Fig. 8* we can see a 2D Doppler image obtained by computation of the M_o ($f_{\min}$=2 kHz and $f_{\max}$=22 kHz) over 50 x 10 pixels scanned with a resolution of 150 µm. The image corresponds to the blood flow in a Y shape of a visible subcutaneous vein of a human hand.

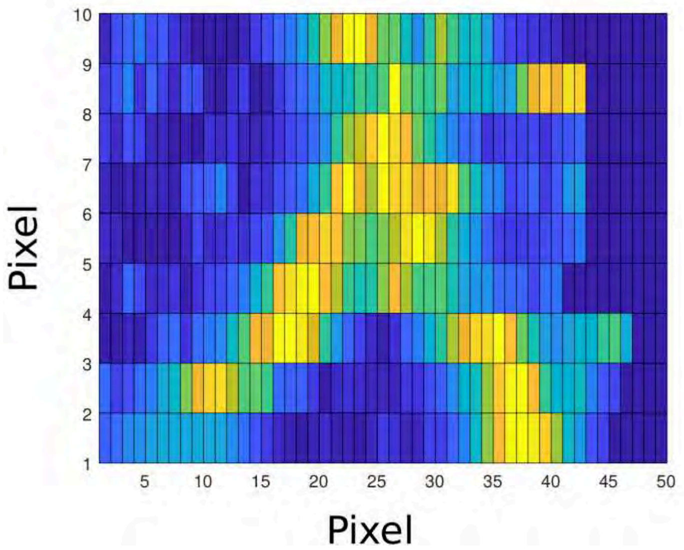

Fig. 8. 2D Doppler image (50 x 10 pixels) of blood perfusion from a Y shape subcutaneous vein of human hand.

3.3. 2D MEMS micro-mirror beam steering system

3.3.1 Description of the sensor arrangement

As described in the context section, the core issues with translation stage scanning system are their bulkiness and the required time for damping mechanical vibration after each displacement. A MEMs based beam steering system shall by nature solve both issues. As a counterpart, the beam steering system comes with a more complex optical alignment. While the previous optical configuration used only one lens for focusing the laser beam, in order to enable the scanning feature with a circular MEMS mirror, a double lens configuration was chosen as the laser beam is first collimated towards the mobile mirror by the first lens, and then a second lens focuses the beam on the flow to be measured. The lens dimensioning was based on geometric approximations in order to result in a 2 mm diameter collimated beam and a maximum scanning area of 20 mm x 20 mm. So based on the worst case laser beam divergence of 30° from ML725B11F datasheet, and the angular range of -5° to +5° from the X/Y MEMS steering mirror specifications, the following lenses were specified: C660TME-C (f=2.97 mm) collimating lens and AC254-060-C-ML (f=60 mm) focusing lens. The clear aperture (22.8mm) of the focusing lens limits the maximum scanning area of the system, so being defined with a margin, up to 20 mm x 20 mm.

The OFI embedded device represented in the *Fig. 9a* has been designed to be able to provide a 2D image with quantitative information of the local velocity in microfluidics applications. The hardware solution of the system was designed and packaged in two parts (*Fig. 9a*): the handheld part (*Fig. 11a*) that includes the OFI sensor itself with the complete optical solution, the laser, and the PCB with the laser driver and the OFI signal conditioning (transimpedance amplifier and filter) circuits (*Fig. 9c*); and the base, that provide power supply and interface the handheld sensing system with the PC. The base (*Fig. 9b*) includes an ADC acquisition card (National Instruments NI-6361 USB OEM) with an interface board for glue logic (CMOS/TTL) and cabling. The handheld and base devices are connected through a 1.5 m 14-wire cable.

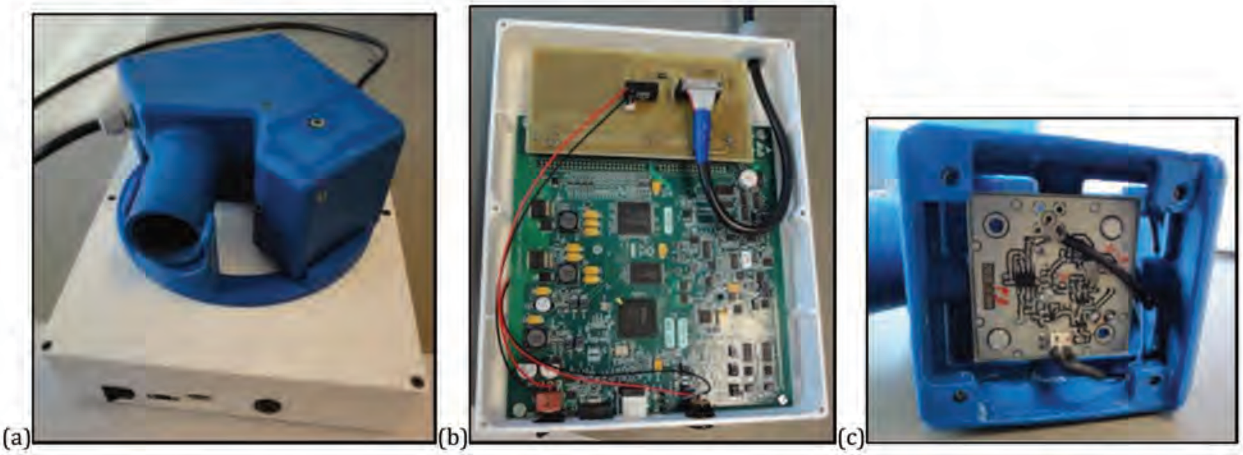

Fig. 9. (a) Photography of a prototype of the handheld imager and its base (both cases made in a 3D printer). (b) Photography inside the imager base showing the ADC and interface cards. (c) Photography showing the custom Laser driver board including the transimpedance amplifier and filtering circuits.

The system embedded in the handheld part of the sensor (*Fig. 11a*) is detailed in *Fig. 10*. It is constituted of: a DFB laser diode (Mitsubishi ML725B11) lasing at λ=1310 nm, with a built-in monitoring photodiode; a PCB (*Fig. 9c*) with a custom-made laser driver and a transimpedance amplifier (gain of 119 dB) including band-pass filter (82 Hz to 46 kHz). The collimating lens (Thorlabs C660TME-C) is placed in front of the laser to fit and keep the beam width along the optical path and inside the circular aluminum coated mirror (Mirrorcle S4417) of diameter 4.2 mm. A 1-inch focusing lens (Thorlabs AC254-060-C-ML) is placed at its working distance from the target to focus the beam, so the maximum possible area to scan is limited by the clear aperture (22.8 mm) of this lens.

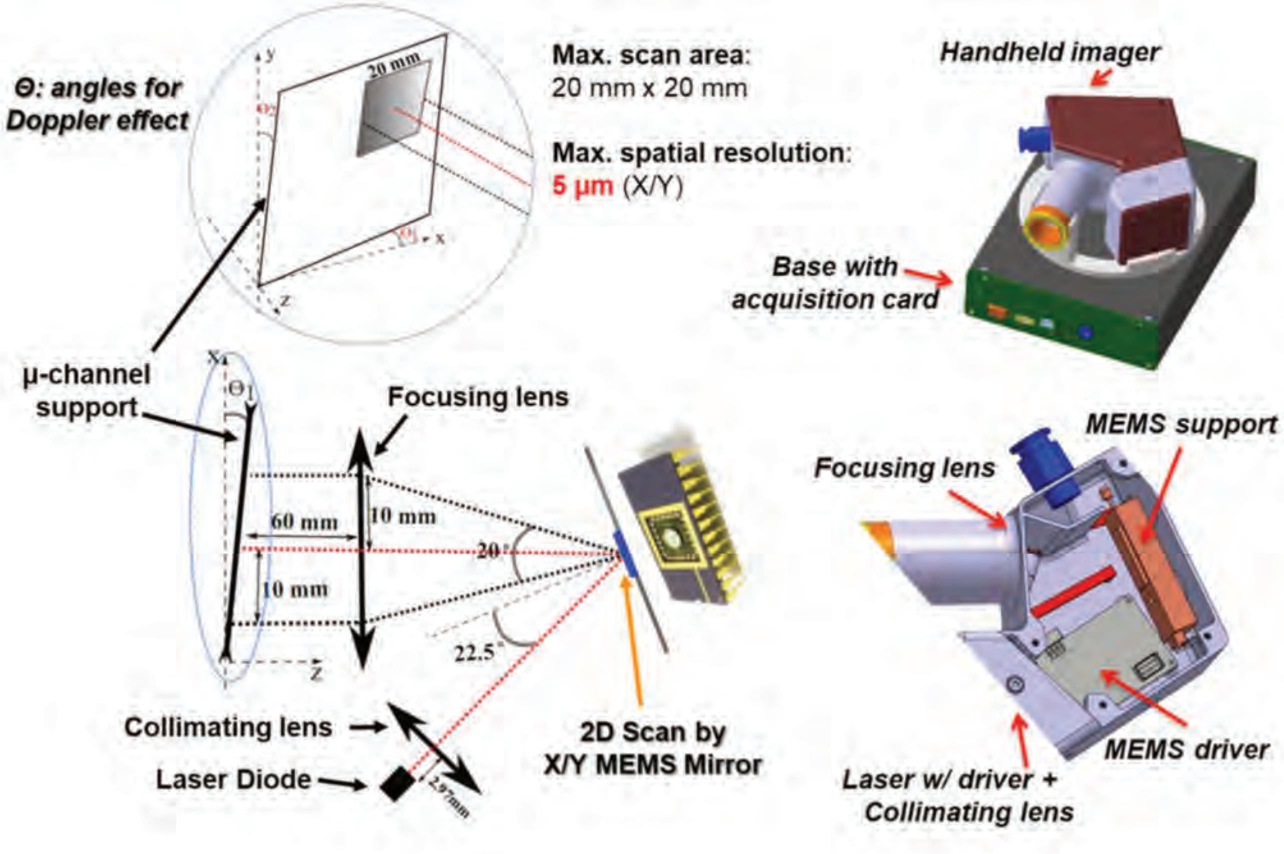

Fig. 10. 2D scanning system embedded in the handheld part. The red dot line indicates the laser path with the mirror centered at X=Y=0°. The two others in black indicate the path in the extremes of the angular range of the mirror.

The MEMS mirror is packaged in a DIP24 actuator with C-coated protection glass. It is designed for an angle of incidence of 22.5° to the normal (with a tolerance of +/-10°). The DIP24 package is mounted on a PCB that realize the interface with the ADC MEMS driver (BDQ PicoAmp 4.475-100 HVA 790-B) as we can see in the *Fig. 11b.*

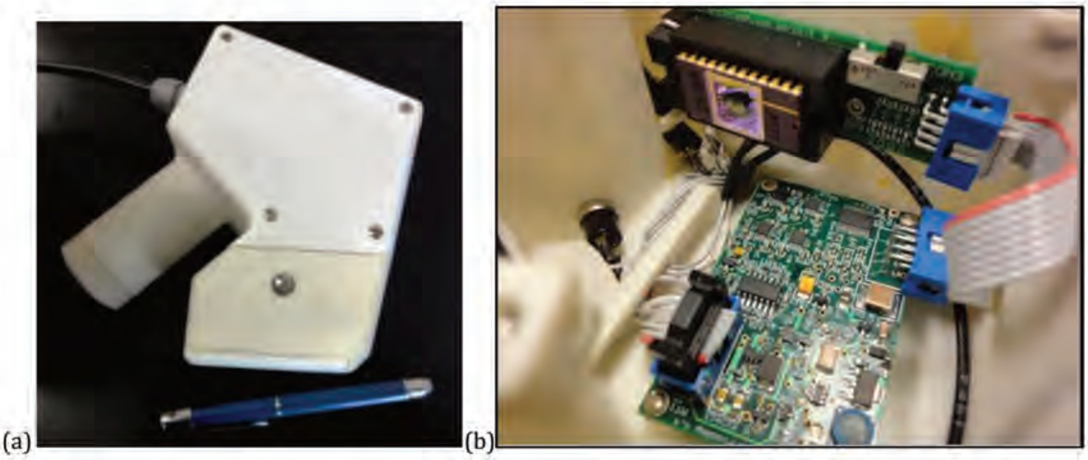

Fig.11. (a) Photography of the 1st prototype for the handheld part (made on a 3D printer). (b)Photography inside the handheld part showing the MEMS mirror system.

The MEMS beam steering mirror perform a steering angle range from -5° to +5° in each direction (X/Y), for driving voltages from to -10V to +10V at the analog inputs of its driver board. The MEMS commands are generated by the ADC card through a dedicated Labview VI. This VI includes appropriate procedures to start and to shut down the MEMS system, and generates the MEMS's driver clock.

The scanning resolution is limited by the minimum voltage step (5 mV) achievable at the ADC output leading to a minimum step angle of 0.0025°. With our optical system, this angle step implies a resolution of 5 μm on the target. A graphical user interface (GUI) allows to configure the rasterization parameters.

The main parameters that limit the scanning speed are: the time of acquisition for each pixel and the interval between each acquisition. This latest was set according to the MEMS mirror datasheet at 50 ms to ensure that the mirror is fully steady before starting the acquisition. Then the MEMS mirror contributes for an improvement on that factor, being able to reach a good feasibility while being, much faster than the linear translation stage scanning system (500 ms).

Beyond that interval, the time of acquisition is affected by the sampling rate (set at 1 MHz) of the acquisition card, and the number of samples (set at 409.600) for each pixel.

3.3.2. Ex-vivo experiments

In order to validate the proper operation and the reliability of the information acquired by the sensor, a first experiment was performed with a transparent plastic (polyurethane) tube of 500 µm inner diameter as the target. The tube is set at the sensor working distance, with the angles of the micro-channel support set at θ_1=0° and θ_2=7.5° (see *Fig. 12a*). The handheld part and micro-channel support are fixed on a mechanically damped optical table. The fluid injected in the tube by a syringe pump (Harvard Apparatus Pico 11 Plus) is full milk as it is considered a valid blood phantom.

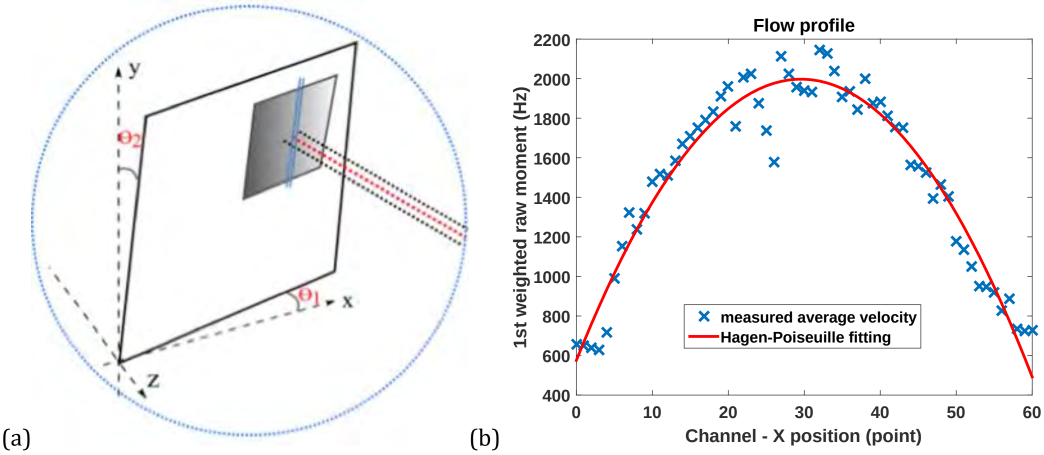

Fig. 12. (a) Illustration of a2D scanning to exploit the flow profile in a plastic circular tube (blue) placed vertically in a support set withθ_1=0° and θ_2=6°(b) Flow profile resulted from a 2D scanning of 60 x 3 points (with 61440 samples/point acquired at 1MHz; f_{min} = 250 Hz and f_{max} = 20 kHz for $\overline{f_D}$).

For the acquisition of the flow profile, 3 lines (at different Y locations) of 60 points (along the X) have been scanned across the channel with X/Y resolutions of

8.33 µm. The *Fig. 12b* shows the measured (mean of the 3 lines) flow profile for the milk pumped at a constant flow rate of 50 µL/min. It reveals a laminar flow regime fitting well the Hagen-Poiseuille profile [2-3] for a Newtonian fluid.

For a laminar flow, the velocity profile in a circular channel is parabolic, with the velocity increasing from zero at the wall to a maximum value at the center according the expression [3]:

$$V\ (r) = V_{\max}\left(1 - \frac{r^2}{R^2}\right),$$

where $V_{\max}$ is the velocity at the center of the channel. r is the radial position, and R is the inner radius of the channel.

The theoretical value for mean velocity (V_{mean}) corresponds to Q/A, where Q is the volumetric flow rate and A is the duct cross section area. For a circular duct, $V_{\text{mean}} = V_{\max}/2$.

For each point (pixel), we can assess the average velocity (V_{avg}) across the sensing volume as:

$$V_{avg} = \frac{\lambda \overline{f_D}}{2n sin(\theta)}$$

where $\overline{f_D}$ is the average Doppler frequency computed from the signal spectrum through the 1st weighted moment; θ is the angle between the laser beam axis and the normal to the target velocity vector; n is the refractive index of the fluid (1.354 for full milk at 1310nm); and λ is the wavelength of the laser (1310 nm). Such V_{avg} in center of the channel should be approximate to V_{mean}.

In a second experiment, to evaluate the imaging performance, a full 300x50 pixels image is acquired in order to qualify the scanning resolution capability and to validate the related trade-off with the scanning time. For this setup, a 100 µm square micro-channel (*Fig. 13a*) made in SU8-photoresist using photolithography was designed. The angles of the micro-channel support with regards to the normal plane to the laser beam are: θ_1=3° and θ_2=7.5° (*Fig. 12a*), as both are necessary in order to obtain the Doppler effect across the curved sections of the serpentines depicted in (Fig. 13b).

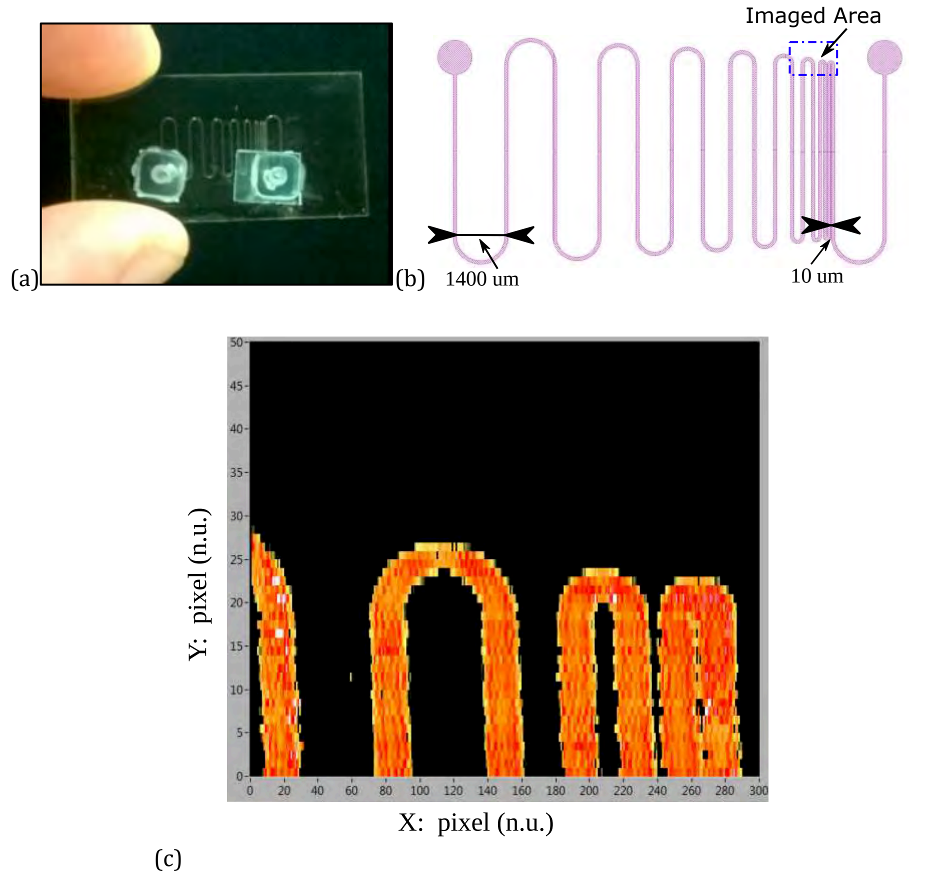

Fig. 13. (a) Photo of the 100 µm square micro-channel with serpentines. (b) CAD design for the square 100µm micro-channel done with CLEWin5. (c) 2D Doppler image (300x50 pixels) of a part of the serpentine 100 square micro-channel. On this X resolution (~5.8 µm), the channel width corresponds roughly to 20 pixels, so ~116 µm.

Figure 13c shows the 2D Doppler image of a part of the serpentine where full milk is pumped at a flow rate of 10 µL/min. The scanning resolution in the X direction is ~5.8 µm, and ~25 µm in the Y direction. These values were chosen to show the minimal spatial resolution in X but with a larger step in Y not to compromise too much the scanning time.

As can be seen on *Fig. 13b*, the imager is able to discriminate the different channels until the very last step of the serpentine where the gap between each channel is only 10 µm.

The scanning of the 15.000 pixels for this Doppler image took 185 minutes. Although it is not an issue for these *in* vitro experiments considering the full automation of the system, it is clearly a critical issue for *in* vivo measurement where patient may feel quite uncomfortable 3 hours long test. The trade-off for a feasible minimum number of samples is to be defined since a lower number limits the quality of the measurement.

Keeping the same acquisition parameters, the *Fig. 14* shows a scanning for a larger area (now below on the right), covering 20.000 pixels (200x100) with a resolution in X of ~19µm, and in Y of 52 µm. The scanning of this Doppler image took now 247 minutes. Although the constant pumping flow rate, in a wider scanning area a visible contrast arises on the amplitude intensity along Y due to θ_2=7.5° which sets the micro-channel out from the focal plane along the Y axe.

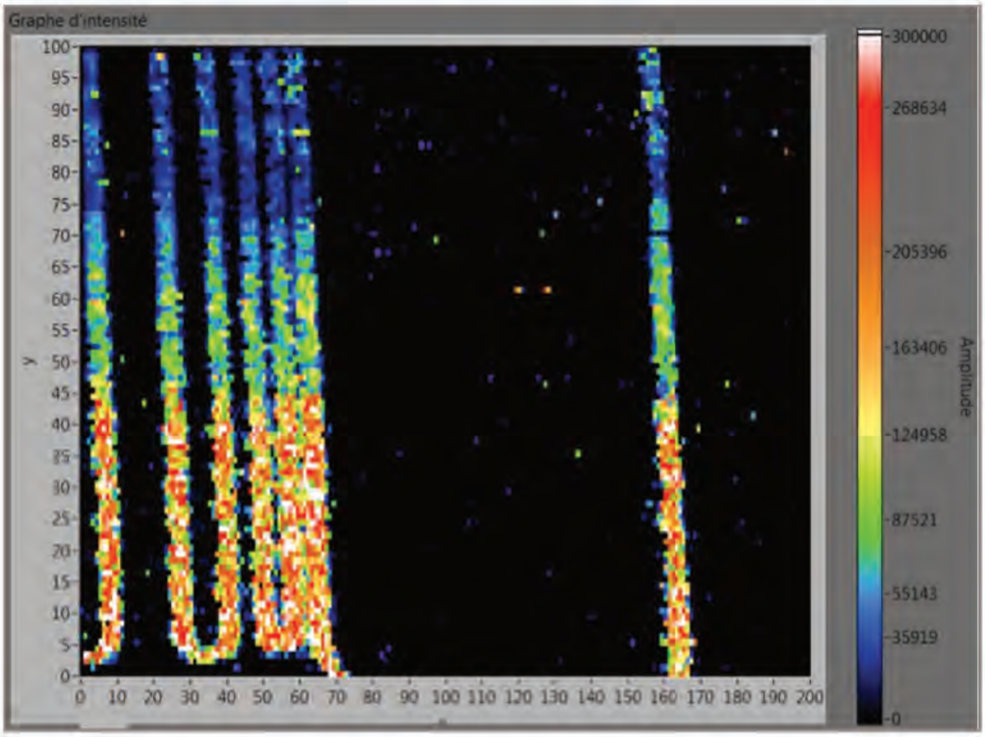

Fig. 14. 2D Doppler image (200x100 pixels) of a part of the 100µm square channel. On this X resolution (~19µm), the channel width corresponds roughly to 6 pixels, so ~114 µm.

The initial number of samples was initially chosen for the single point OFI sensor mounted on translation stages, for which the delay between each displacement was the main parameter causing slow acquisition of images. However, with the beam steering system, the time of the acquisition of each pixel itself has become problematic.

In order to evaluate the lower limit for which the number of samples in the acquisition is acceptable we have tested several solutions and tried to observe the degradation of the computed image. With a number of samples by pixel of 102.400, (*Fig. 15),* we start to lose the capability to discern the expected increasing of the average velocity around the center of the channel.

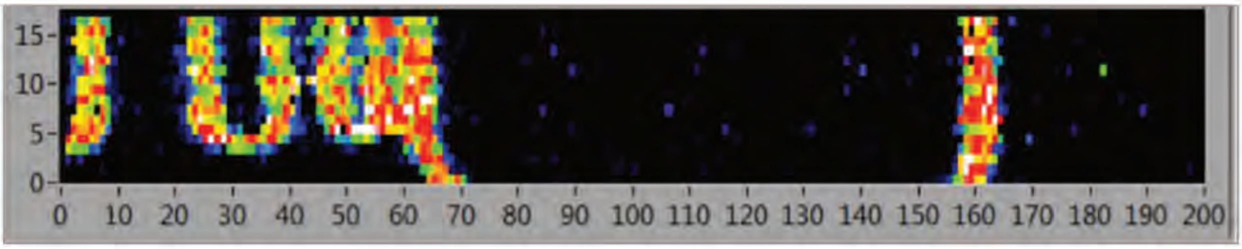

Fig. 15. 2D Doppler image with 102.400 samples/pixel, so a scanning time estimated around 4x faster.

In *Fig. 16*, with only 20.480 samples/pixel, we can see a very poor image quality where we start to compromise the sensor ability to detect the channels of the serpentine with low spacing.

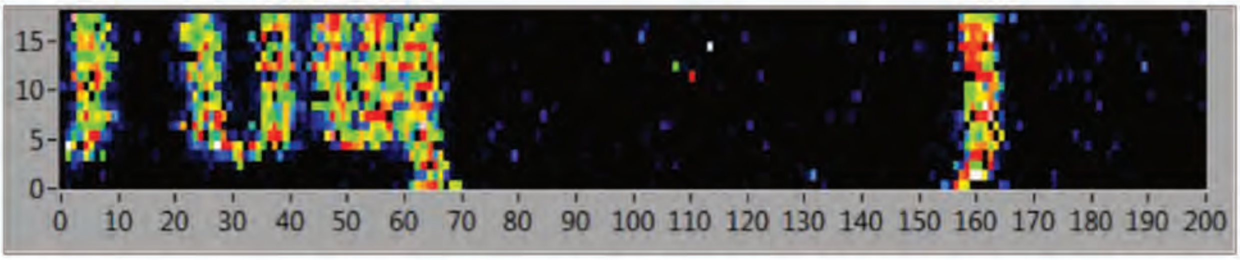

Fig. 16. 2D Doppler image with 20480 samples/pixel, so a scanning time estimated around 20x faster.

From these ex vivo evaluations, we have decided to keep the acquisition of 409.600 samples by pixel at 1Mhz sampling rate for in vivo cases.

3.3.3. In vivo experiments

The *Fig. 17* illustrates the arrangement for *in vivo* application of the imager. The *Fig. 17a* shows the metallic ring to be placed over the patient skin surrounding a target tumour. This ring, that was common to all Diagnoptics imagers offers several functionalities: a lock enables the proper plugging of the handheld part, offering mechanical stability, it serves as a positioning reference for the scanning. An extra ring is screwed on the sensor package that ensure that once plugged, the laser spot will be focused exactly on the plan corresponding to the skin surface. The ring is attached to the skin thanks to a circular double side sticker (photography in *Fig. 18*) with a central hole of 15 mm diameter.

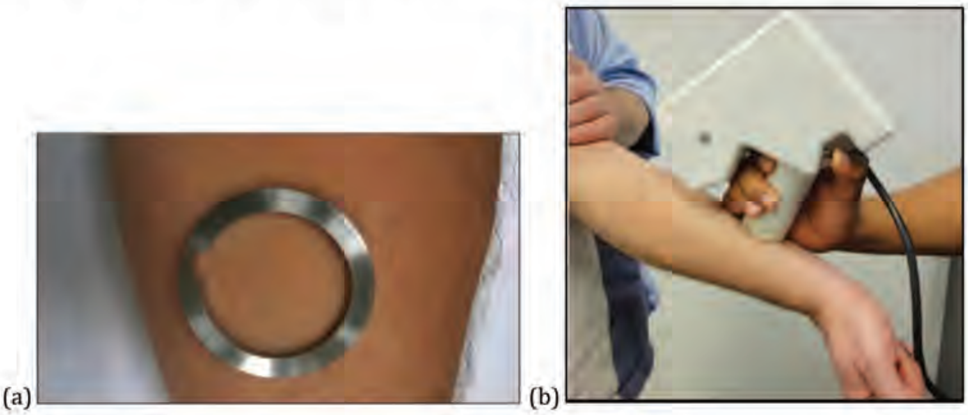

Fig. 17. (a) Photography of the metallic ring placed over the skin. (b) Photography of the handheld part placed over the forearm of a patient in order to assess the blood perfusion of a vein.

A pushbutton (*Fig. 17b*) triggers the scanning, and the data acquired are saved in the PC for post-analysis.

The *scanning time* is an important concern, as it should be the faster as possible to guarantee enough comfort for the practitioner and even more for the patient. Beyond the comfort aspect, for a better quality of data acquisition, minimizing the exposure to mechanical instabilities due to stronger movements on handling due to fatigue. After discussions with the practitioners, the trade-off chosen in the context of the Diagnoptics project is to set 2 minutes as the maximum scanning time.

As we have defined the following requirements for the rasterization: 409600 samples/pixel (as considered fair enough from the *ex vivo* validations) at 1MHz sampling rate, with the specified 50 ms delay between each pixel acquisition; the image is to be formed by 15x15 pixels. Under these conditions, a total number of 225 pixels gives a total scanning time (around 1' 45'') which respects the project requirement.

Path folder measurements: F:\Labview Fev_2016\Drivers instuments du labo\Antonio lu Adam Raul Diagnoptics\programmes exploitables\scan 2D micro miroir\labviewProj

patient name: patienTest

Lesion type given: lesionTest

POSITION IN_X: 14

POSITION IN_Y: 14

Fig. 18. In vivo version of the Graphical user interface of the Labview VI implemented to drive the 2D scanning, and also to acquire and to save the scanned raw data.

Another constraint of the Diagnoptics project was the image size with a minimum requirement of 8 mm x 8 mm. We have set it to 10 mm x 10 mm, as illustrated in the photography included in the GUI (*Fig. 17*). The X/Y resolution is then equal to 0.67 mm, very far from the sensor resolution which cannot be used to produce similar detailed imaged as have been shown in the *ex vivo* experiments. Thus, considering the fact that low scanning resolution would make unfeasible contrast evaluations from scanned images, after discussions with the doctors involved in the Diagnoptics project, we have agreed to perform a statistical approach over the whole rasterization to try to evaluate the blood perfusion beneath the skin.

Beyond the trade-off between the number of pixels against the scanning time, we should mention the memory limitation. As to reduce the time of acquisition and then achieve the required timing, the data must be kept in the RAM memory of the PC until the end of the full scanning since the transfer to the hard drive is very time consuming.

3.3.4. Results and discussion

Emulation of the vascularization

Using the handheld 2D scanning we could successfully validate the assessment of blood perfusion ratio by application of the camphor-cream.

For the present experimental validation, the human skin region chosen was the back of the GP, as such skin region doesn't present any visible superficial vein. As discussed previously, the goal is to be able to catch an "image" of the superficial micro-vascularization for each scanned skin region. The *Fig. 19* shows the red skin region with vascularization stimulated by camphor-cream application.

Fig. 19. Photography of the back arm regions scanned: treated (red, after application of camphor-based cream) and normal skin regions.

In the present context, the zeroth order Moment (M_0) will be proportional to the number of red blood cells (as main Doppler scattering particles) tracking the blood perfusion. After each scanning the average M_0 of all pixels scanned was calculated for each region. The mean M_0 ratio (treated skin over normal one) obtained was 2.2% in 4 measurements (0.93%, 3.81%, 2.4% and 1.68%) in different places of the respective regions. In other words, an average excess of M_0 of 2.2% for the red skin as compared to the normal skin.

Clinical study

Among the researchers involved in the Diagnoptics project, we counted with the participation of two teams of doctors, specialists in skin cancer. One was the Hospital Clinic of Barcelona, Spain; and the other was the Policlinico of Modena, Italy. Two complete 2D OFI imager systems were sent to the respective Hospital teams to collect *in vivo* raw data collected from lesions of actual patients.

Due to the fact that the 2D Doppler imager from Barcelona returned misaligned, we have considered that the measurement performed there were not suitable for any evaluation of the method and we'll consider here only the analysis from the raw data acquired at Modena. The medical protocol stated that three kinds of skin lesions have been analyzed: malignant basal cell carcinomas (32 different cases), malignant melanomas (27 cases) and benign melanocytic nevi (105 cases).

Considering the huge amount of data acquired, the processing and the analysis is still on going. Also, in the context of the Diagnoptics project, no information was provided about the evolutional phase of each tumor considering the angiogenesis since no biopsy was performed on the lesion tested. For example, although the number of erythrocytes (RBC cells) in a given tissue area is eventually increased in a tumor, their flow velocity can be markedly decreased. So a study of criteria considering the way of tumor develops for each kind of lesion must be carefully evaluated, in order that M_0 parameter can be really helpful as an additional element contributing to enhance a proper excision decision.

Due to that, we cannot be fully sure of the feasibility of our method used, and we present here the promising preliminary results obtained.

In agreement with the doctors, we have decided to consider the hypothesis that the skin lesions are small as compared to the shooting zone, and that they're always well centralized in the ring. In that way, in the interpretation of the results we consider as *central area*, the quantitative information corresponding to the 5 x 5 pixels central square among the 15 x 15 pixels of the whole scanned data (225 pixels in total).

The results from the computation of M_0 obtained for each kind of lesion are shown in *Fig. 20a*. The blue diamonds represent the average M_0 values corresponding to the 25 pixels from the *central area*. The green squares represent the average M_0 values from all pixels. The *Fig. 20a* reveals that M_0 is higher in average for both BCC (basal cell carcinoma) and MLM (malignant melanoma) as compared to the Nevus type of lesion. Also, M_0 in the central area is higher in average for both MLM and BCC (not for NEVUS).

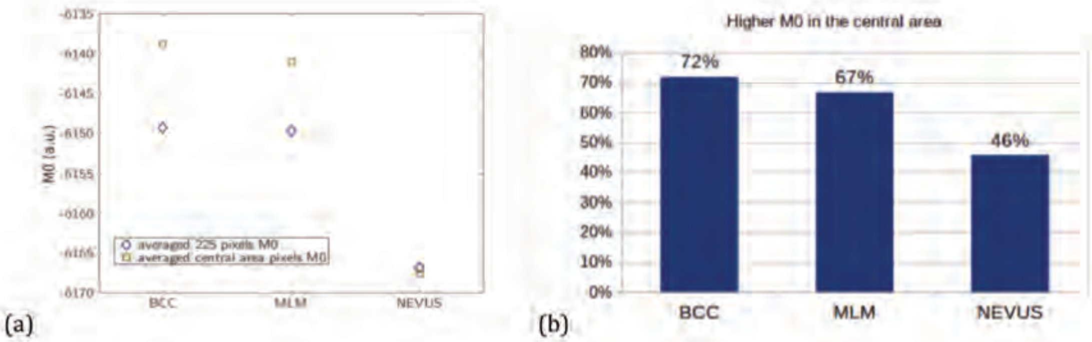

Fig. 20. (a) For each type of skin lesion: M_0 values averaged for the *central area* (green squares) and for all pixels (blue diamonds). (b) For each skin lesion kind: sample ratio for higher M_0 in the *central area*.

The *Fig. 20b* shows the sample ratio for a higher M_0 in the central area as compared to the surrounding area (remaining pixels). Then the average M_0 for the central area M_0 is significantly higher than the surrounding for BCC (72%) and MLM (67%).

For our present experimental context, M_0 should be proportional to the blood vascularization beneath the skin.

The cross relation with the results from the other non-invasive techniques developed in the Diagnoptics project (color, pattern, thickness, shape, dimension) is still judged essential for a reasonable excision decision.

In the context skin cancer, this 2D OFI imager suggests to offer additional information in the differential diagnosis of some skin lesions, what is promising and supports the continuation of the researches. Eventually it can give a better parameter by increasing the resolution, as it's designed to reach enough high resolution (up to 5 µm), despite the increasing of scanning time beyond the 2 min requirement.

3.4. Conclusion

In this chapter we have presented the evolution of feasibility of the non-invasive OFI sensing technique to realize Doppler images for flowmetry applications in microfluidics field. In this context, our work culminates with an innovating device based on the association of the OFI sensor with a two-axis point-to-point beam-steering mirror demonstrating the design of an OFI 2D Doppler imager that is extremely compact. Regarding the state of the art on OFI embedded sensors for flowmetry, this device presents an important improvement for its compactness and its scanning time despite this characteristic is still to be improved.

Regarding the signal processing, the Moment method is a promising approach to exploit the fluidic perfusion information That approach has been validated in ex vivo, in vitro and in vivo conditions. Also, some important advances were achieved on enhancing the robustness against mechanical noises due to inherent movements of in vivo targets, but still, improvements must be done in the related signal conditioning when the measurement is performed while handling the imager.

Chapter references

1. R. Kliese, Y. L. Lim, E. Stefan, J. Perchoux, S. J. Wilson, and A. D. Rakić. Rapid scanning flow sensor based on the self-mixing effect in a VCSEL. Conference on Optoelectronic and Microelectronic Materials and Devices, Canberra, ACT, **2010**, *pp.* 7-8.
2. L. Campagnolo, M. Nikolić, J. Perchoux, et al. Flow profile measurement in microchannel using the optical feedback interferometry sensing technique. *Microfluid Nanofluid.* **2013**, *vol.* 14, pp. 113-119, 10.1007/s10404-012-1029-0.
3. L. CAMPAGNOLO, Optical feedback interferometry sensing technique for flow measurements in microchannels. PhD thesis, Université de Toulouse, France, February 12th, **2013**.
4. A. Quotb, E. E. Ramírez-Miquet, C. Tronche, and J. Perchoux, Optical Feedback Interferometry sensor for flow characterization inside ex-vivo vessel. *IEEE.* **2014**, pp. 362–365, 10.1109/ICSENS.2014.6985009.
5. M. Stücker, I. Horstmann, C. Nüchel, A. Röchling, K. Hoffmann, and P. Altmeyer. *Blood flow compared in benign melanocytic naevi, malignant melanomas and basal cell carcinomas*. Clinical and Experimental Dermatology. **1999**, *vol.* 24, *issue* 2, *pp.* 107-111.
6. R. Choe, M. E. Putt, P. M. Carlile, T. Durduran, J. M. Giammarco, D. R. Busch, K. Won Jung, B. J. Czerniecki, J. Tchou, M. D. Feldman, C. Mies, M. A. Rosen, M. D. Schnall, A. DeMichele, and A. G. Yodh. Optically Measured Microvascular Blood Flow Contrast of Malignant Breast Tumors. *PLOS ONE. **2014**, vol.* 9, *issue* 6.
7. R. Bonner and R. Nossal. Model for laser Doppler measurements of blood flow in tissue, *Appl. Opt.***1981**, *vol.* 20, *pp.* 2097-2107.
8. F. de Mul, M. Koelink, A.L. Weijers, J. Greve, J. Aarnoudse, R. Graaff, and A. C. M. Dassel. Self-mixing laser-doppler velocimetry of liquid flow and of blood perfusion in tissue, *Appl. Opt.***1992**, *vol. 31, issue 27*, 5844–5851, 10.1364/AO.31.005844.
9. F.F.M. de Mul, M. H. Koelink, A. L. Weijers, J. Greve, J. G. Aarnoudse, R. Graaff, and A. C. M. Dassel. A semiconductor laser used for direct measurement of the blood perfusion of tissue. *IEEE transactions on biomedical engineering*. **1993**, *vol.* 40, *no.* 2.
10. C. Zakian and M. Dickinson. Laser Doppler imaging through tissues phantoms by using self-mixing interferometry with a laser diode. *Applied Optics*. **2007**, *vol.* 32, *no.* 19.
11. M. Norgia, A. Pesatori, and L. Rovati. Optical Flowmeter for Blood Extracorporeal Circulators. *IEEE*. **2009**, 10.1109/IMTC.2009.5168741.
12. J. R. Tucker, J. L. Baque, Y. L. Lim, A. V. Zvyagin, and A. D. Rakic. Parallel self-mixing imaging system based on an array of vertical-cavity surface-emitting lasers. *Applied Optics*.**2007**, *vol.* 46, *no.* 25.
13. J. Perchoux, A. Quotb, R. Atashkhooei, F. J. Azcona, E. E. Ramírez-Miquet, O. Bernal, A. Jha, A. Luna-Arriaga, C. Yanez, J. Caum, T. Bosch, and S. Royo. Current Developments on Optical Feedback Interferometry as an All-Optical Sensor for Biomedical Applications. Sensors. **2016**, *vol.* 16, *issue* 5, *article* 694, 10.3390/s16050694.

CHAPTER 4: Micro and nanoparticles characterizations with OFI

4.1. Context

As presented in the previous chapters, many OFI sensing techniques are capable to perform flowmetry and local velocimetry in the microfluidics field; but the researches with OFI flowmetry for particle characterization are very recent. Previous OFI works performing particle sizing, based on laser diode [1-5], solid-state laser [6-12] and He-Ne laser [13] technologies, have been limited to aqueous suspensions at multiple or single scattering regimes. To the best of our knowledge, none of them performed any kind of measurement at a single particle regime.

In the context of particle characterization with the OFI technology based on laser diode, in 2005, Zakian [1] has shown the possibility to perform particle sizing for polystyrene monodisperse nanospheres, in a diameter ranging from 20 to 202 nm, undergoing Brownian motion in watery diluted suspensions at low particle concentration (less than 0.5% in volume). In 2016, Alexandrova [3] has indicated the tendency of proportionality between the amplitude of the spectral Doppler peak and the particle concentration for watery suspensions of 1 µm-diameter Titanium Dioxide (TiO_2) spheres seeded at low concentrations (0.03%-0.8%) and pumped at high velocity (1.2 m/s).

The work depicted in this chapter shows the feasibility for the detection and the measurement of a single particle velocity in watery fluids at very low particle concentration. We present here an innovative sensing technique based on the Optical Feedback Interferometry scheme in a laser diode that enables single particle detection and velocimetry at micro and nano-scales through the Doppler-Fizeau effect. Thanks to the proposed signal processing, this sensing technique can detect the presence of single spherical micro/nanoparticles and measure their velocity, even while their diameter is far below half the laser wavelength. The method was validated with polystyrene spheres with diameter ranging from 110 nm to 39.63μm flowing in diluted aqueous suspensions.

Beyond that, we have also performed particle sizing for multiple scatterers seeded in aqueous suspensions under single scattering regime, while keeping the same particle concentration for each aqueous suspension made with a different particle size. Zakian's particle sizing method (described in Chapter 1) applies to steady aqueous suspensions, while ours fits for microfluidics applications where the fluids are pumped at laminar flow. Moreover, our method has been validated with aqueous suspensions made not only with polystyrene spheres at nanometric range, but with micrometric ones as well.

Finally, based on the very same method that we have applied to particle sizing, we will show possibility to quantify the particle concentration for aqueous suspensions made with nano/microparticles from single to multiple scattering regimes, pumped at laminar flow.

All these results indicate potential applications for the chemical engineering and biomedical fields. For instance, we depict the possibility to detect bigger particles seeded at very low concentration in an aqueous suspension of smaller particles. In this case, the technique suggests a potential application for blood clot (thrombus) detection, for example.

The increasing demand for technologies of nanoparticles detection and characterization in biomedical and chemical engineering applications has reached industrial processes where we believe OFI sensing would propose a novel interferometric method of high potential benefit.

4.2. Single particle regime

A particle detection OFI sensor is basically a laser diode with an optical configuration allowing for a sharp focus at the center of the micro-channel region where a laminar flow is established as illustrated by the *Fig. 1*.

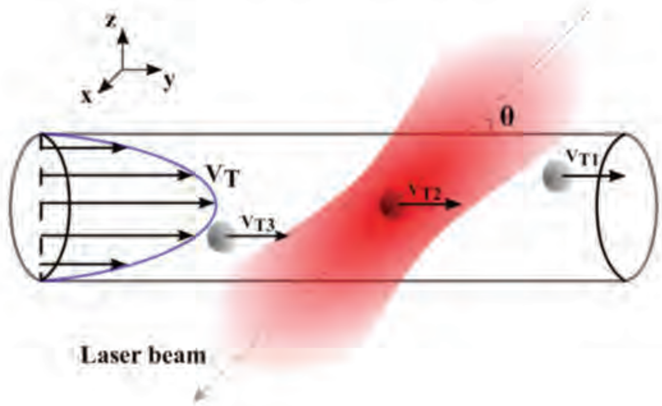

Fig. 1. Laser beam focused in the center of a circular duct with laminar flow under single particle regime.

Once a particle crosses the laser sensing volume with a velocity V_T, it generates a Doppler shift frequency (f_D) of backscattered re-injected light by Eq. 2.1.

The nature of the sensor signal is ruled by the laser power density of illumination, the scattering cross-section of the particles and their optical properties in the medium. The complete phenomenon is described by Mie scattering theory.

The particles are carried in a liquid pumped at constant flow rate into the channel. The particle concentration in such fluid is controlled to achieve a single particle regime where only one single particle is crossing the sensing volume during each signal acquisition period. The velocity V_T of each particle is dependent on its radial position in the duct according to the velocity distribution when a laminar flow profile is established.

4.3. OFI sensing scheme for single particle detection

The setup of OFI sensing used for single particle detection is represented in *Fig*. 2. It is constituted by a 785 nm Fabry-Perot laser diode (Thorlabs L785P090) with a monitoring photodiode built-in package, and a double lens system formed by two aspheric lenses: Thorlabs C240TME-B (f = 8mm) and ACL2520M-B (f = 20 mm) that collimate then focus the laser beam tightly.

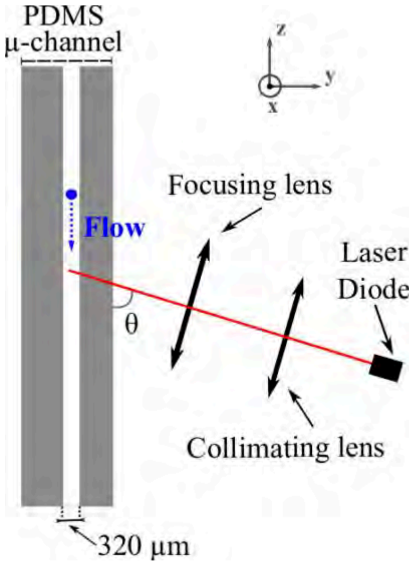

Fig. 2. Double-lens configuration for single particle detection in a microchannel set vertically.

The microfluidic chip used in our experiments is a PDMS circular duct of 320 µm diameter, and 230 mm length, fixed over a support set so that the flow direction is vertical from top to bottom. The related Reynolds number is about 2.64, which gives a hydrodynamic entrance region corresponding to 42.24 µm. The OFI sensor is set on a 3-axis linear stage (Zaber Tech. T-LSM100A), so the laser beam was focused in the center of the micro-channel and far beyond the entrance region.

In that way, the sensing volume is set over the region where the laminar velocity profile is fully developed fitting well the Hagen-Poiseuille profile for a Newtonian fluid. For a circular cross section, the maximum velocity (v_{max}, corresponding to the center of the channel) is equal to 2Q/A; where Q is the volumetric flow rate and A is the cross section area. In all experiments, the liquid was pumped at constant flow rate of 40 µL/min with a pressure pump (Fluigent MFCS-EZ) equipped with a flowmeter (Fluigent Flow Unit M, 5% accuracy over measured value) for flow rate control. The angle θ of 82° is set between optical axis and the flow direction ensuring a maximum Doppler shift of 5.9 kHz for a particle in the center of the duct.

When the laser emits onto the flowing particle, some of the scattered light can re-enter the laser cavity and interact with the free-running laser mode. The resulting output laser power is subject to modulation, and the frequency of this modulation correspond to the Doppler shift that is determined by the particle velocity. Then the sensing signal is obtained from the current of the monitoring built-in package photodiode which reveals an image of the output optical power of the laser. This OFI signal is acquired by a data acquisition card (National Instruments NI-6361 USB) through a custom transimpedance amplifier.

4.3.1. Single particle detection algorithm

The signal conditioning and processing is applied through Matlab scripts embedded in a Labview VI program, and the detection is automated and performed in real-time in order to avoid a huge big data saved for post-processing, considering of course the limited memory available in the computer.

The algorithm flow chart is shown in *Fig*. 3. In the first stage (labelled ***Acquisition)***, the acquired signal is constituted by 2^{17} samples acquired at 2 MHz sampling frequency. Consequently, the time period corresponding to each acquisition corresponds roughly to 66 ms. In order to remove the noise from mechanical vibration and electronics, the signal is filtered by a band-pass filter, which cut-off frequencies are set to 900 and 8.5 kHz respectively.

In the second stage (***Spectral conditions),*** an amplitude threshold is set in the signal spectrum after the subtraction of the average spectrum computed from the 10 previous acquisition windows without burst detection, and the actual spectrum. This subtraction allows removing the background noise. The amplitude threshold is set to 3 dB. If the detected peak does not fit the frequency range (1 to 6.5 kHz), the present acquisition is discarded, and the cycle restarts from the first stage. Otherwise, in the third stage ***(Burst scanning)***, the time domain OFI signal is sliced into 512 overlapping sub-windows of 2^{13} samples for which a FFT is performed. Later on, the spectral domain amplitude of the Doppler peak frequency is measured for all sub-windows, and the result is normalized by the maximum amplitude peak found. This works as a burst scanning system at the Doppler peak frequency. If only a single burst is found in the amplitude prominence checking, the algorithm enters stage (***Data recoding)***, where the time domain OFI signal is saved. Otherwise the current acquisition is discarded and the cycle is restarted.

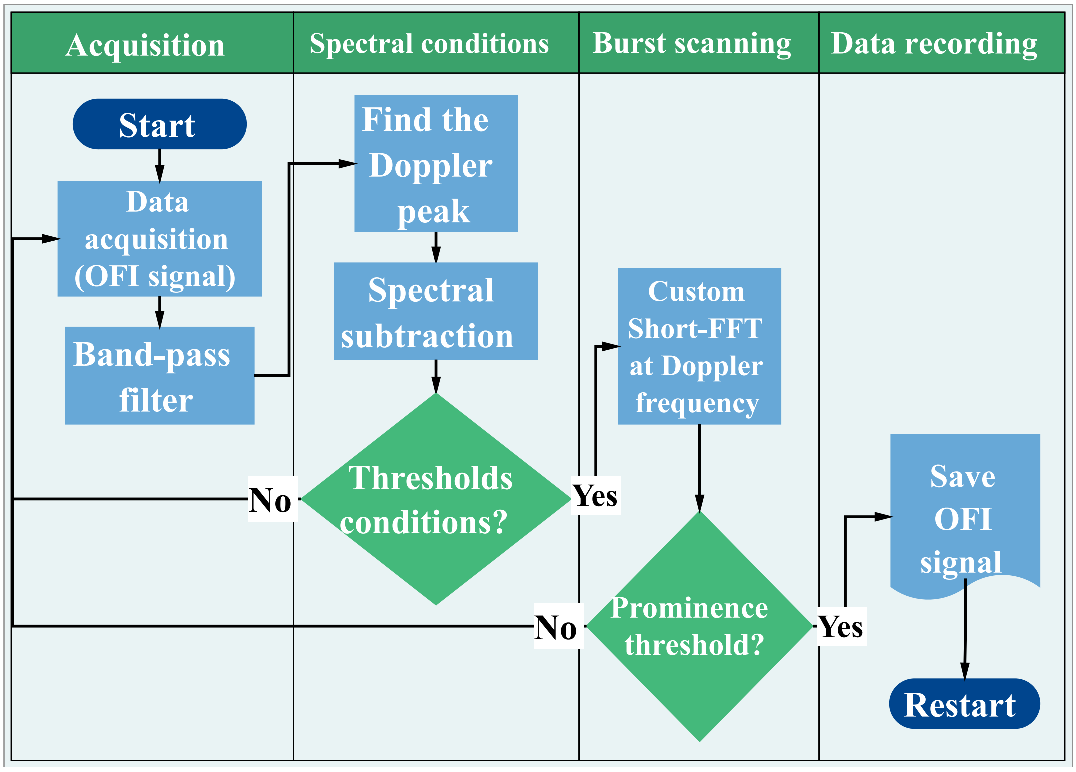

Fig. 3. Flowchart of single particle detection algorithm.

The algorithm implemented is working continuously as long as aqueous suspensions are flowing in the microchannel, thus storing all events that fit the conditions in amplitude, frequency and single burst per acquisition.

4.3.2. Scattering particles

As scattering particles for research purpose we have used polystyrene (PS) non-porous spheres at unique controlled size with very low size standard deviation, monodisperse in aqueous suspensions made of deionized water. Their surface is anionically charged, thus avoiding agglomeration.

In table 4.1 we show more pertinent details according the vendor information.

Vendor	Part number	Mean Diameter **(nm)**	Diameter Standard Deviation **(nm)**	Mother suspension concentration **(% w/v)**	Mother suspension concentration **(mg/mL)**	Mother suspension concentration **(spheres/mL)**
Corpuscular	C-PS-0.10	110	-	2.5	25	$1.21\times10^{+13}$
Microparticles GmbH	PSRKM10	196	5	5.0	50	$1.06\times10^{+13}$
Microparticles GmbH	PSRL2654	552	13	5.0	50	$5.35\times10^{+11}$
Corpuscular	C-PS-1.0	1000	-	2.5	25	$4.69\times10^{+10}$
Microparticles GmbH	PSQRKM383	4970	80	10.0	100	$1.40\times10^{+9}$
Microparticles GmbH	PSQRKM383	10140	120	10.0	100	$1.83\times10^{+8}$
Microparticles GmbH	PSQRL2547	39630	720	10.0	100	$3.07\times10^{+6}$

Table 4.1. Vendor information regarding the polystyrene spheres used.

In parallel, the spheres diameter have been thrice measured with a Malvern Zetasizer Nano ZS (range up to 6 µm), and the following results were obtained as shown in Table 4.2.

Vendor	Part number	Mean Diameter **(nm)**	Peak Diameter **(nm)**	Diameter Standard Deviation **(nm)**
Corpuscular	C-PS-0.10	158	159	17
Microparticles GmbH	PSRKM10	209	215	45
Microparticles GmbH	PSRL2654	573	589	120
Corpuscular	C-PS-1.0	1006	945	89
Microparticles GmbH	PSQRKM383	5024	4742	661

Table 4.2. Size values obtained by measurements with Zetasizer Nano ZS regarding polystyrene spheres used (up to 5 µm).

According to Bohren [14] in the case where the scattering particles are spheres, the Mie scattering theory is the most suitable, and theoretically applicable for any size and refractive index. Then using the software MiePlot [15], we could evaluate the theoretical scattering intensity expected for all diameters we are using. The *Fig. 4* reveals polar plots of the scattering intensity versus the scattering angle for each diameter of monodisperse polystyrene sphere in deionized water once illuminated by an unpolarised illumination point source (laser emitting 39 mW at 785 nm).

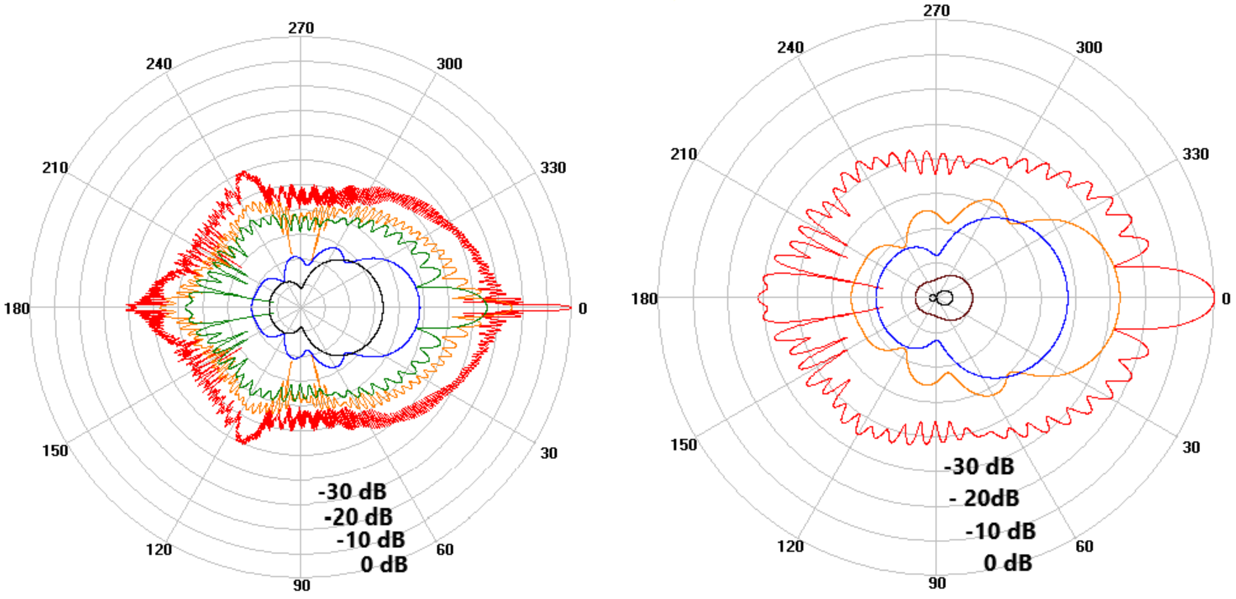

(a) (b)

Fig. 4. Polar plot based on Mie theory of the scattering intensity versus scattering angle for different monodisperse polystyrene sphere diameters: (a) 39.63μm (red), 10.14μm (orange), 4.97μm (green), 1μm (blue), 552nm (black). (b) 4.97μm (red), 1μm (orange), 552nm (blue), 196nm (brown), 110nm (black). Such patterns correspond to an illumination from a point source, a laser emitting 39.6mW at 785nm in the direction from 180° to 0°. Normalizing the scattered power intensity from each outer circle (0 dB), the inner circles corresponds respectively to (a) -100 dB, and (b) -70 dB.

As we can see in *Fig*. 4, most of the scattered power is forward-scattered in the propagation direction (0°) of the laser beam due to the transmitted rays. Only a small share (≈ 12%) is back-scattered [90°-270°], and even less is retro-injected into the laser cavity contributing with the OFI signal.

It is important to remember that the laser sensing volume is defined by the contribution capability that depends on the backscattering cross-section of each particle. So, theoretically, keeping the same scattering properties, the optical feedback power should be linked to the size parameter x:

$$x = \frac{2\pi n d}{\lambda} \qquad (4.1)$$

where n is the refractive index of the surrounding medium, λ is the wavelength of the incident light and d is the diameter of the spherical particle.

4.3.3. Detection rate evaluation

In order to ensure the purity of the deionized water (type 1 ultra-pure, from Merck Direct-Q 5UV with 0.2 µm filter) used in our dilutions, and at same time the sterility of the tools and tubing involved, deionized water was pumped at 40 µL/min during 2 hours. The system did not detect any burst corresponding to a particle. We can affirm that because during this experiment we have recorded all the few acquisitions windows presenting a signal amplitude crossing the threshold condition, and by visual checking of the time domain signals versus the burst scanning graphs, we have confirmed that such cases were really artefacts of the sensing system.

From each mother suspension, we have prepared a dilution with deionized water - so that none of the possible particles that are naturally present in plain water will affect the measurement - and obtained a particle concentration low enough to be able to reach a single particle regime over an acquisition time of 66 ms.

As the 110 nm spheres represent a real challenge for detection under the single particle regime, since the sensor is only able to detect just a very few events in hours of experiment, we have used the next smallest nanospheres available for evaluation of the detection rate of the sensor. For 196nm spheres at a particle concentration of $8.5\times10^{+4}$ mL^{-1}, we have got a detection rate of 13 burst detections/hour. When the particle concentration is higher than 10^{6}, the detection rate increases gradually against the particle concentration. When the particle density is in a range from 10^{6} mL^{-1} to 10^{7} mL^{-1}, the burst detection number increases significantly against the particle concentration. When the density approaches 10^8 mL^{-1}, multi-bursts occur within the acquisition time. The *Fig. 6* presents the trend of this detection rate evaluation for the case of 196nm PS spheres.

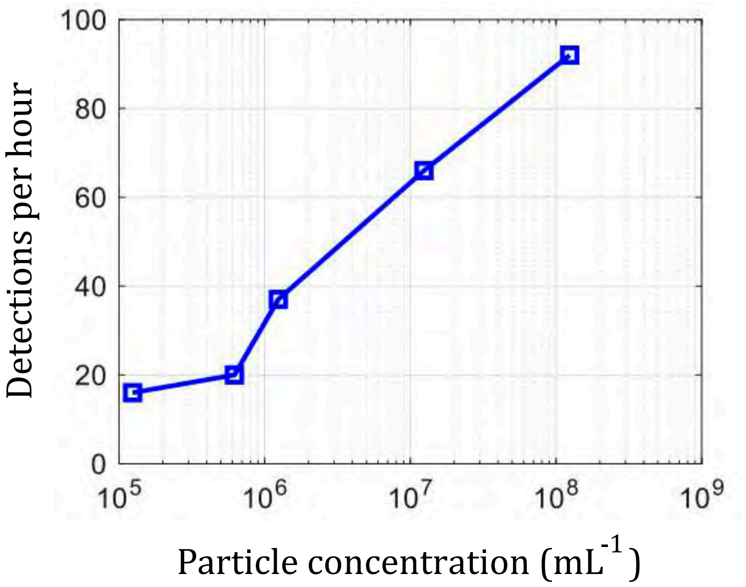

Fig. 6. Detected burst number trend versus the particle concentration in unit volume for 196nm PS sphere suspensions pumped at 40µL/min.

At micrometric diameter range the detection rate increases significantly. For example, keeping the same particle concentration of $8.5\times10^{+4}$ mL^{-1} for 10.14 µm spheres we have obtained a detection rate of 166 burst detections/hour.

We have observed that in case of mother aqueous suspensions made with polystyrene spheres of 39.63 µm diameter, the particles sink very quickly after mixing. Besides the polystyrene spheres from Microparticles GmbH are hydrophobic, these biggest ones are too dense. In that way, it seems we could not obtain a dilution to be kept as homogenous during enough time (even at low particle concentrations) for single particle detection. So, for the 39.63 µm diameter and at the same particle concentration we obtain a majority of multiple bursts in a same acquisition window. Thus, the detection rate could not be evaluated for this diameter.

4.3.4. Single detection and velocimetry

Before presenting the overall data analysis from several acquisitions obtained with the single particle detection algorithm, we will introduce one example of single detection and particle velocimetry for each particle size. Figure 7 shows the time domain signals from one selection among the single particle detections for each PS spheres size: 10.14 μm (at 2.9×10^{4} mL^{-1}), 4.97 μm (at 2.8×10^{5} mL^{-1}), 1 μm (at 9.3×10^{3} mL^{-1}), 550nm (at 1.4×10^{5} mL^{-1}), 196 nm and 110 nm (at 1.4×10^{6} mL^{-1}). The blue lines represent the original OFI signal acquired and the green onesthe same signal after filtering.

Although we can perceive a pattern of amplitude variation corresponding to a burst outline in the original time domain signal, it is only in the filtered one that we can really identify the presence of a proper burst corresponding to a particle detection. At a quick glance in these examples, we can perceive that even the visual identification become more challenging while the particle size decreases. That is why we have circled in dashed red lines the burst corresponding to the 110nm particle in *Fig. 7f*.

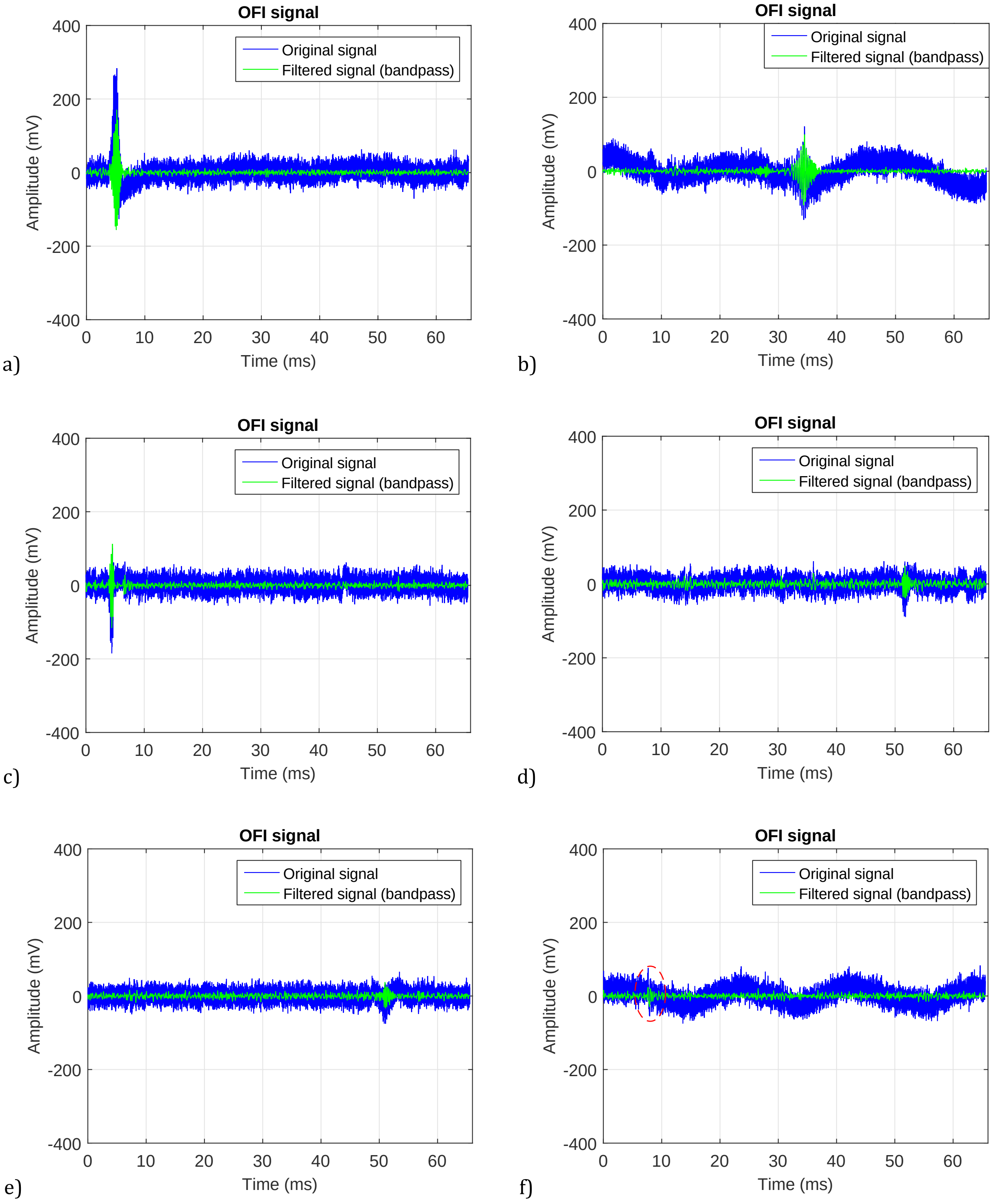

Fig. 7. OFI time domain signal acquired before (blue) and after (green) band-pass filtering, regarding a single (a) 10.14 μm, (b) 4.97 μm, (c) 1 μm, (d) 550 nm, (e) 196 nm, (f) 110 nm PS sphere detected.

Figure 8 shows the related spectra of the filtered signal (blue solid lines), where the black dashed lines correspond respectively to the filtered signal spectrum in absence of particle. This last one gives a floor reference to be compared with the respective filtered spectrum where there is particle detected.

The red asterisk indicates the Doppler frequency peak automatically detected by the algorithm over the filtered spectra. The correspondent frequency value measured is linked to the particle velocity by the *Eq. 2.1*.

The difficulty of burst visualization is reflected in the spectra by the decreasing of the SNR while the PS sphere diameter decreases. In *Fig. 8f* we can see that for the 110 nm PS sphere the amplitude of the frequency Doppler peak really approaches the noise floor.

Besides that, both time and spectral domain views suggest that bigger particles fed more power back into the laser. Among these examples, the 1 µm and 552 nm and 196 nm particles hold very close particle velocities (respectively 4.7, 4.4 and 4.5 kHz), and the biggest one presents a Doppler frequency peak with SNR 7 dB above the one with the almost half of its size. By this turn, this one reveals a SNR 2.2 dB above the one with approximately half of its size.

In that way, in the following topic, we have decided to evaluate a parameter related with this aspect in order to find a way to indicate some hint in the quantification of a single particle size.

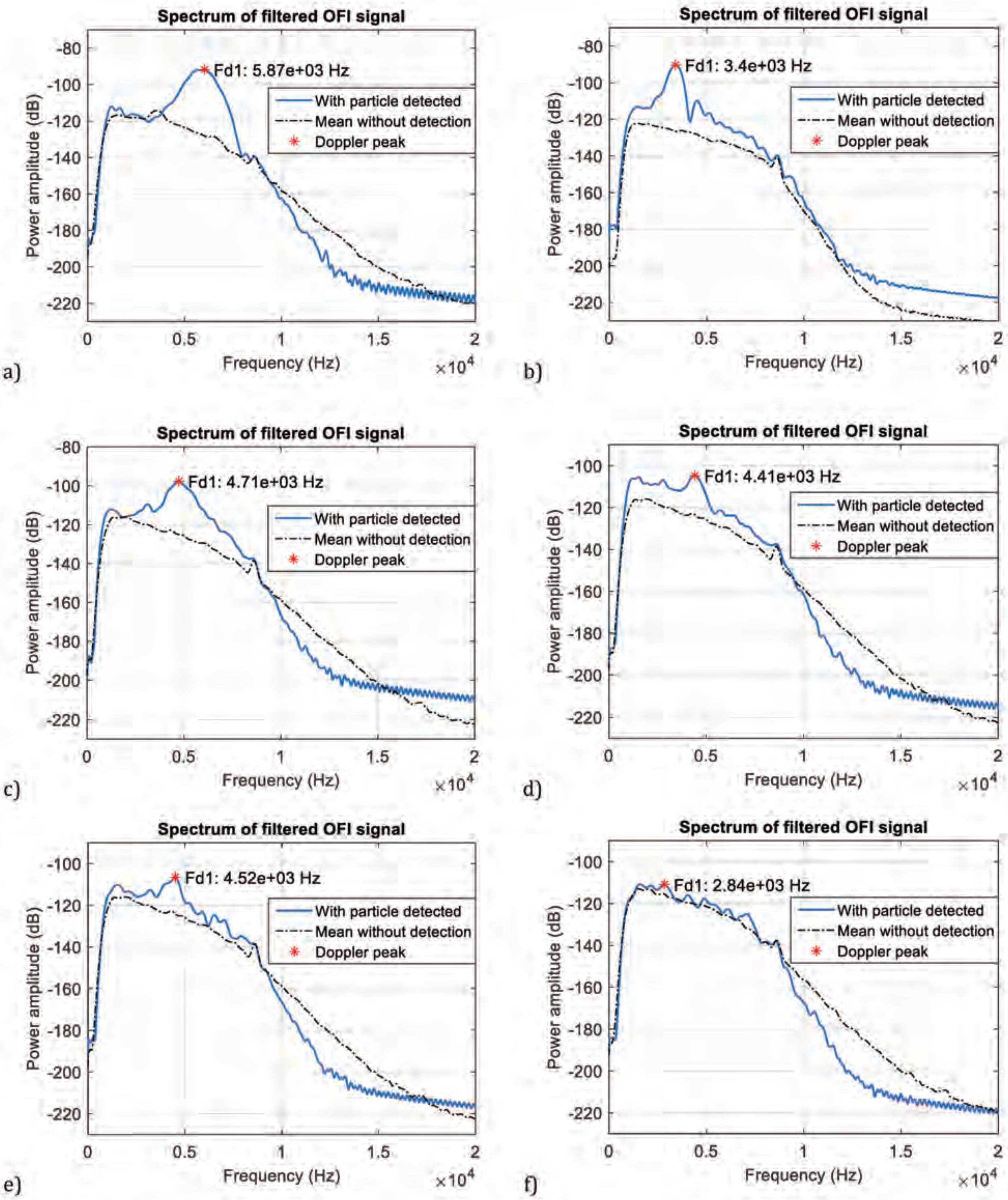

Fig. 8. Filtered signal spectrum (blue solid line) compared to the sensor signal spectrum in absence of particle (black dashed line). The Doppler peak (red asterisk) corresponds to the particle velocity (V_T) accordingly Eq. 2.1 for f_D, regarding the single PS sphere detected: (a) 10.14 μm with $f_D \approx 5.9$ kHz (b) 4.97 μm with $f_D \approx 3.4$ kHz, (c) 1 μm with $f_D \approx 4.7$ kHz, (d) 550 nm with $f_D \approx 4.4$ kHz, (e) 196 nm with $f_D \approx 4.5$ kHz, (f) 110 nm with $f_D \approx$ 2.8kHz.

In the related burst scanning graphs (*Fig. 9*) we can easily perceive the prominence condition attended for single burst detection, as the amplitude is normalized by the maximum amplitude peak found. The red dots mark the two most prominent spectral amplitude peaks of the related Doppler peak frequency, measured across the FFT spectra from 512 sliding overlapping sub-windows (as already explained for the *burst scanning* step in the detection algorithm).

These graphs reveal that the Doppler peak frequency really corresponds to the most prominent frequency that constitutes to the burst, as there is an evident correspondence with the burst positioning in the window of acquisition.

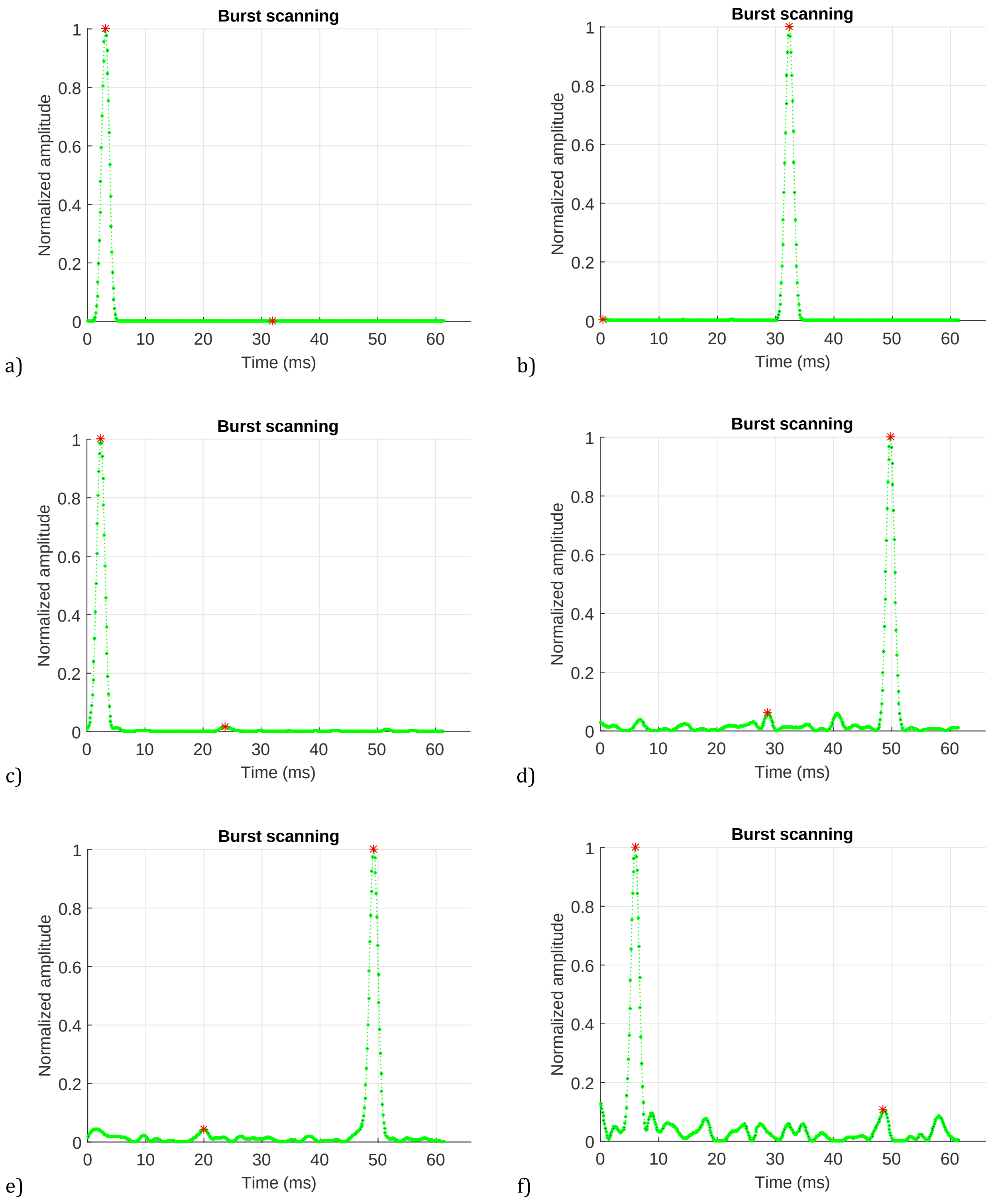

Fig. 9. Burst scanning graph revealing the burst positioning in the acquisition window for the single PS sphere detected: (a) 10.14 µm with $f_D \approx$ 5.9 kHz (b) 4.97 µm with $f_D \approx$ 3.4 kHz, (c) 1 µm with $f_D \approx$ 4.7 kHz, (d) 550 nm with $f_D \approx$ 4.4 kHz, (e)196 nm with $f_D \approx$ 4.5 kHz, and (f) 110 nm with $f_D \approx$ 2.8kHz.

4.3.5. Post-processing analysis regarding sizing prospection

Beyond the simple detection and velocity measurement, we have performed some prospections in order to try to find means to characterize the particle size or at least to discard small particles from bigger ones.

We should remember that, as stated in the previous Chapters, M_0 is linked to the light power fed back into the laser, and consequently is supposed to reveal some information for our sizing analysis.

The present analysis was performed over the database of saved files from single particle detections selected by the algorithm. Then in a post-processing MATLAB script, we compute the filtered signal exactly like it is done in the ***Acquisition*** step of the detection algorithm. We then execute a kind of burst scanning like the one described for the detection algorithm, but now based on the computation of the zeroth order Moment (M_0), instead of the amplitude of the Doppler frequency peak. In other words, M_0 is calculated for each of the 512 windows, and the maximum M_0 become the parameter from each detection for our evaluations. *Figure 10* presents the burst obtained for the same samples presented in the previous topic. For all of them it corresponds to the burst position as obtained to the burst scanning by the amplitude of the maximum Doppler peak. The red asterisk indicates the maximum M_0 for each case.

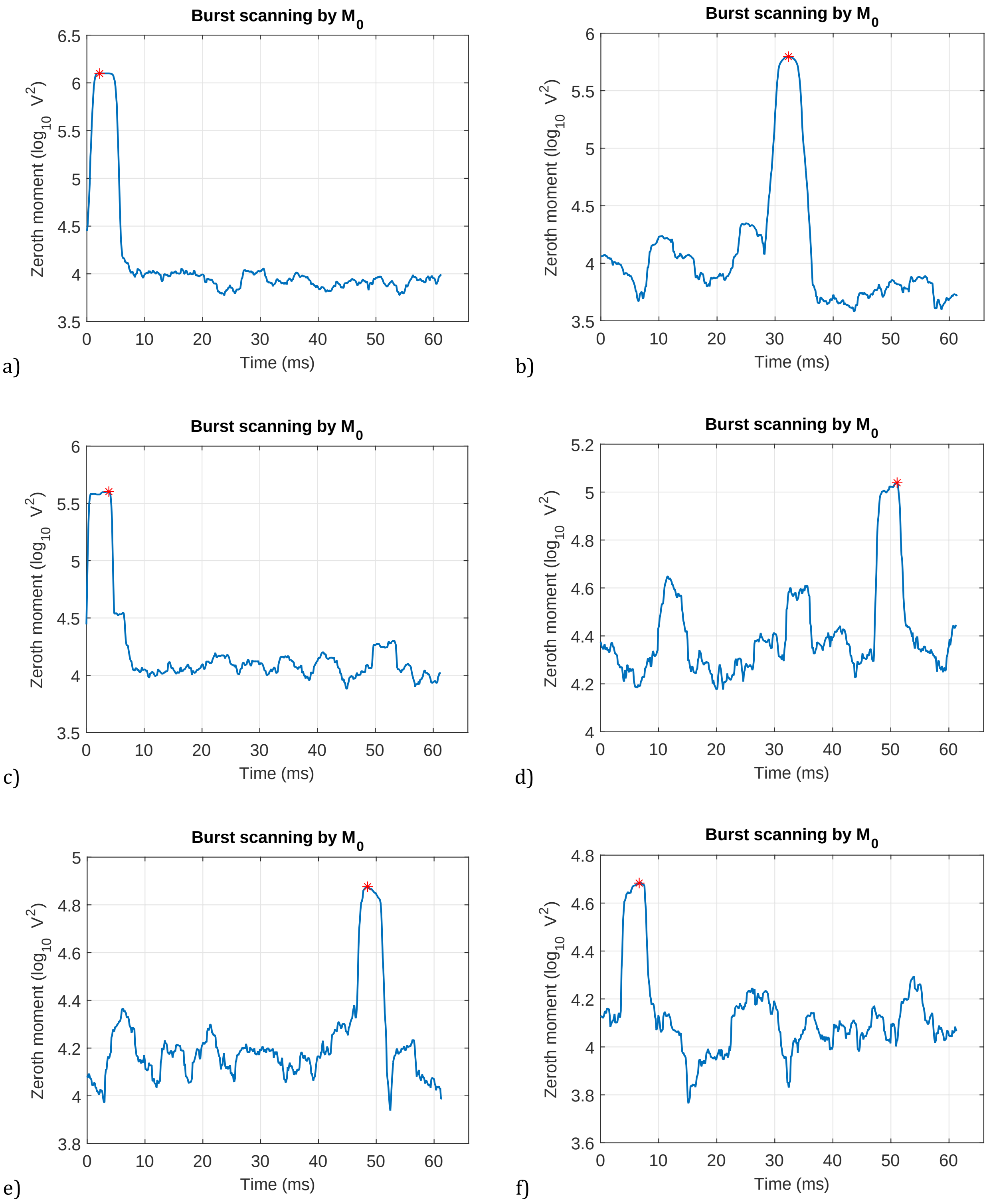

Fig. 10. Burst computed by M_0 amplitude in base 10 logarithm scale, revealing the burst positioning in the acquisition window for the single PS sphere detected: (a) 10.14 μm with $f_D \approx 5.9$ kHz (b) 4.97 μm with $f_D \approx 3.4$ kHz, (c)1μm with $f_D \approx 4.7$ kHz, (d) 550 nm with $f_D \approx 4.4$ kHz, (e) 196 nm with $f_D \approx 4.5$ kHz, and (f) 110 nm with $f_D \approx 2.8$kHz.

For each PS sphere diameter, we present the results of our analysis in a 3D histogram, where (*Fig. 11-15*): the x-axis indicates the frequency range where the spectral Doppler frequency peak of the particle is detected; the y-axis shows the range in logarithm scale of the maximum M_0 of the bursts. In order to evaluate the energy fed back from particles detected around a short variation of velocity, we have defined a width of 250 Hz for each bin of the x-axis in the histogram.

As stated in the experimental description for single particle detection, we highlight that all these experiments under single particle regime were realised in a constant flow rate of 40μL/min.

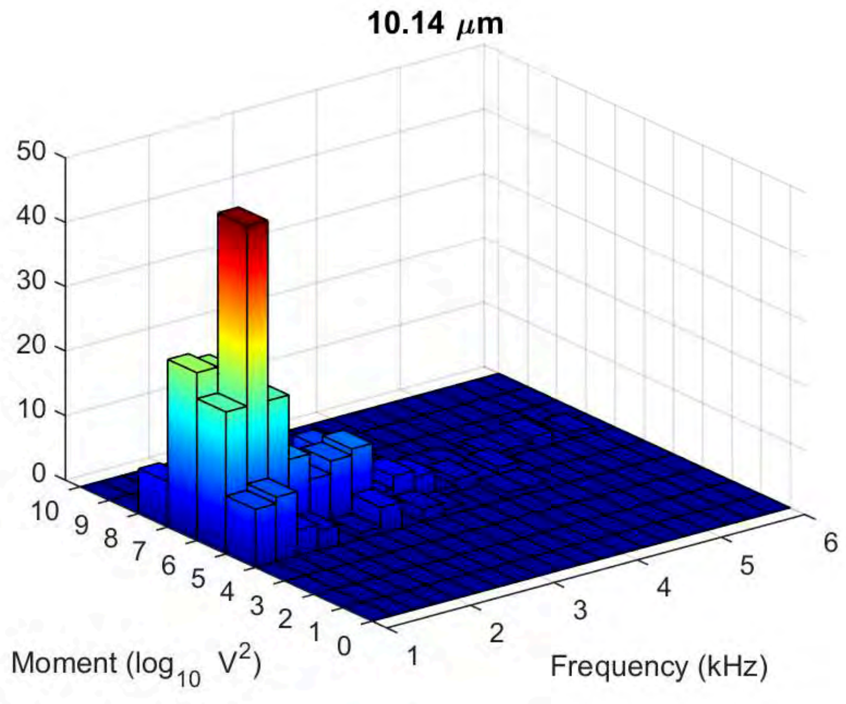

Fig. 11. 3D histogram for 10.14μm polystyrene spheres from an aqueous suspension with particle concentration of $1.8\times10^{+5}$ mL^{-1} pumped at 40μL/min. X-axis: frequency range (each histogram bin corresponds to 250Hz) where fits the spectral Doppler frequency peak of the particle detected; y-axis: range in base 10 logarithm scale of the maximum M_0 corresponding to the detected burst.

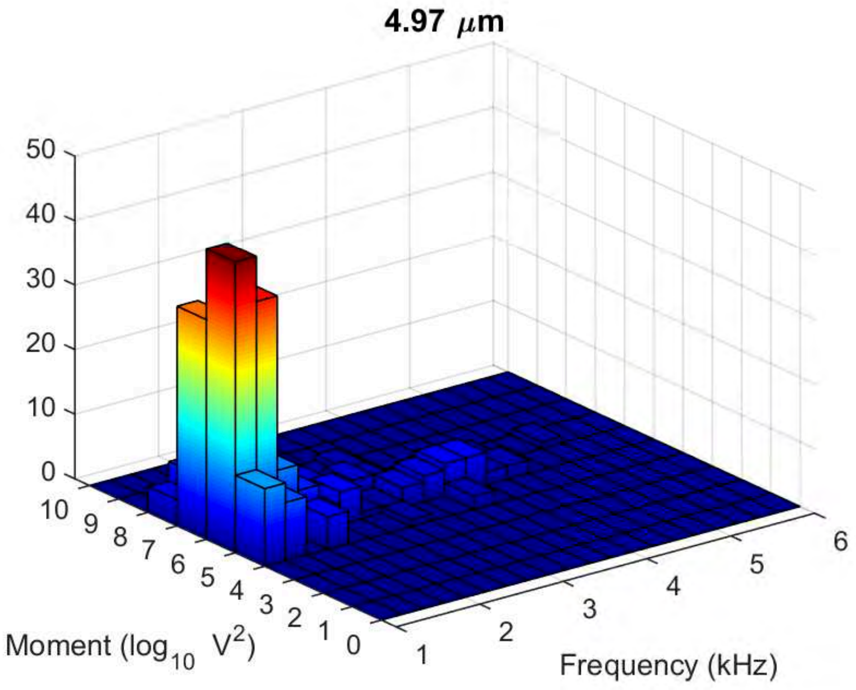

Fig. 12. 3D histogram for 4.97μm polystyrene spheres from an aqueous suspension with particle concentration of $2.8\times10^{+5}$ mL^{-1} pumped at 40μL/min**.** X-axis: frequency range (each histogram bin corresponds to 250Hz) where fits the spectral Doppler frequency peak of the particle detected; y-axis: range in base 10 logarithm scale of the maximum M_0 corresponding to the detected burst.

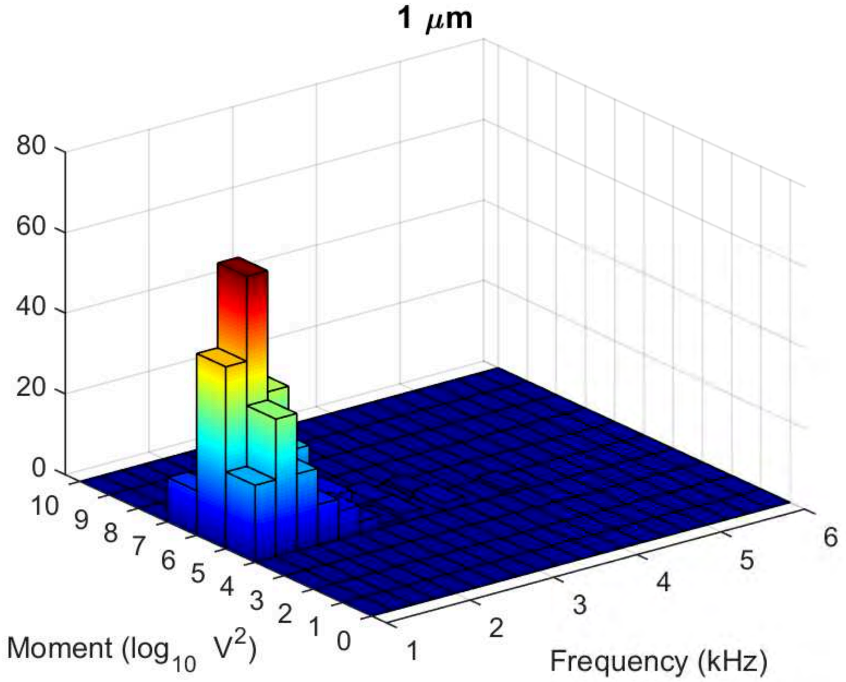

Fig. 13. 3D histogram for 1μm polystyrene spheres from an aqueous suspension with particle concentration of $1.4\times10^{+5}$ mL^{-1} pumped at 40μL/min**.** X-axis: frequency range (each histogram bin corresponds to 250Hz) where fits the spectral Doppler frequency peak of the particle detected; y-axis: range in base 10 logarithm scale of the maximum M_0 corresponding to the detected burst

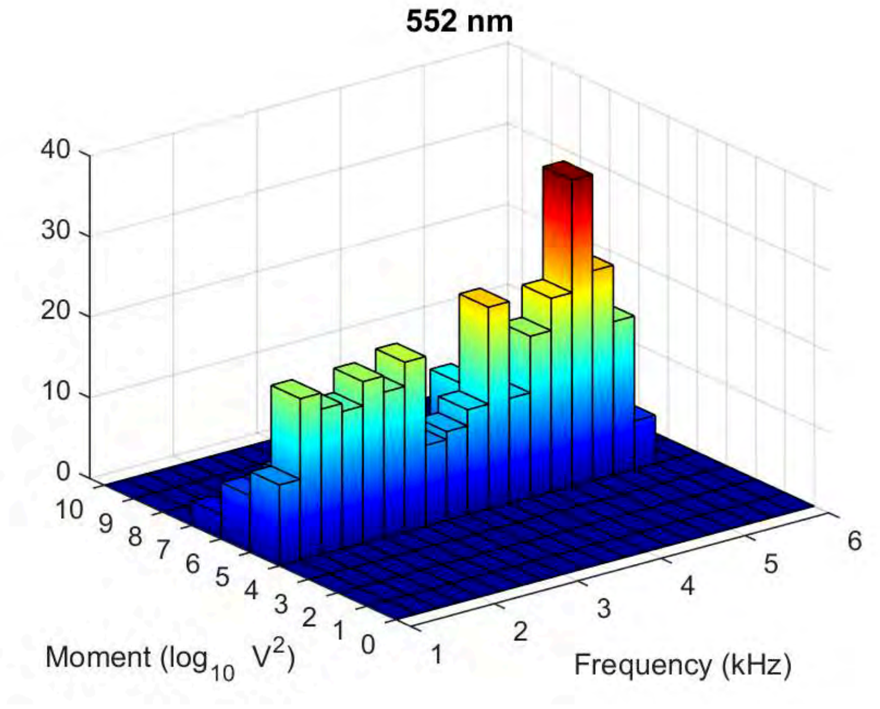

Fig. 14. 3D histogram for 552nm polystyrene spheres from an aqueous suspension with particle concentration of $1.2\times10^{+5}$ mL^{-1} pumped at 40µL/min**.** X-axis: frequency range (each histogram bin corresponds to 250Hz) where fits the spectral Doppler frequency peak of the particle detected; y-axis: range in base 10 logarithm scale of the maximum M_0 corresponding to the detected burst.

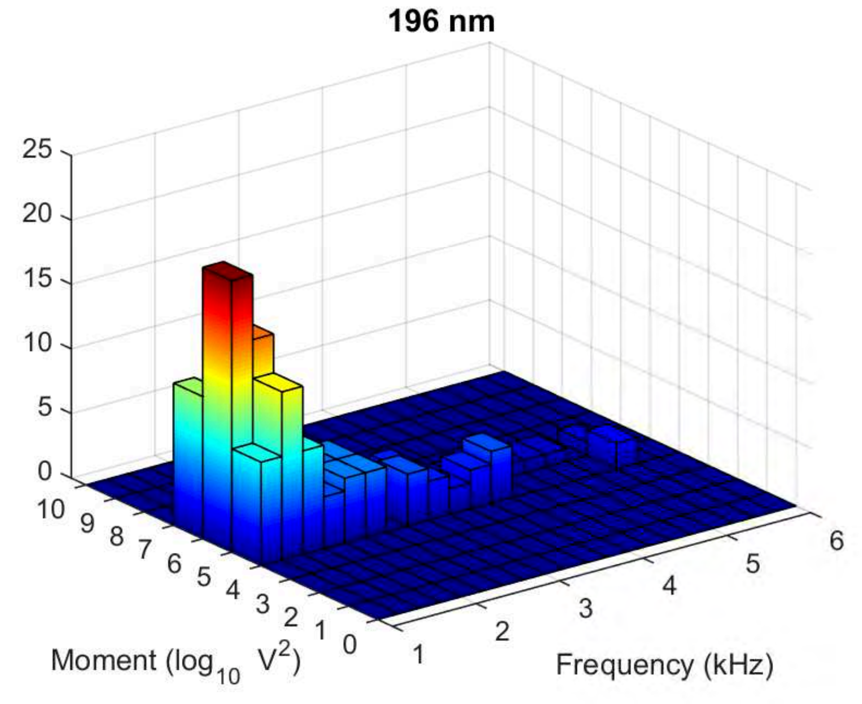

Fig. 15. 3D histogram for 196nm polystyrene spheres from an aqueous suspension with particle concentration of $1.6\times10^{+6}$ mL^{-1} pumped at 40µL/min**.** X-axis: frequency range (each histogram bin corresponds to 250Hz) where fits the spectral Doppler frequency peak of the particle detected; y-axis: range in base 10 logarithm scale of the maximum M_0 corresponding to the detected burst.

From *Fig. 11-15*, we observe that a majority of M_0 values are located below 1.9×10^6 V^2, while for 1 µm particles the maximum M_0 can reach up to 8.6×10^6 V^2, and for both 4.97 µm and 10.14 µm, up to 2.3×10^7 V^2. However, for 196 and 552 nm, the maximum M_0 values are never bigger than 1.9×10^6 V^2. This provides us a first element for potential particle size characterisation, where the maximum M_0 corresponding to the single nanoparticles (196 and 552 nm) never cross the 1.9×10^6 V^2 threshold.

A particular observation is that for 552 nm, the "detectability" is well distributed in the whole frequency range, while for the others that is mostly concentrated up to 2kHz. We don't know to justify this phenomenon. Maybe there is an interferometric effect that rises when the light wavelength and the sphere diameter are close. Moreover, the limitation of the Doppler shift of detected particles is complex to understand, but could be explained by the modelling proposed by Zhao et al [16] where the measurement volume is concentrated at the vicinity of the channel walls due to forward reflected scattering.

In order to obtain an overall evaluation from the histograms' data (*Fig. 11-15*) for the different particle sizes, we have performed averaging for each frequency bin. We have computed the average of all maximum M_0 detected which the frequency Doppler peak is inside the same frequency bin range of 250 Hz. Then we can evaluate the feasibility of particle size characterization by the M_0 parameter while comparing its mean value among a set of particles holding similar velocities. In such perspective, we could evaluate also an eventual correspondence between the mean values of: the M_0 parameter and the frequency Doppler peak (*Fig. 16.*)

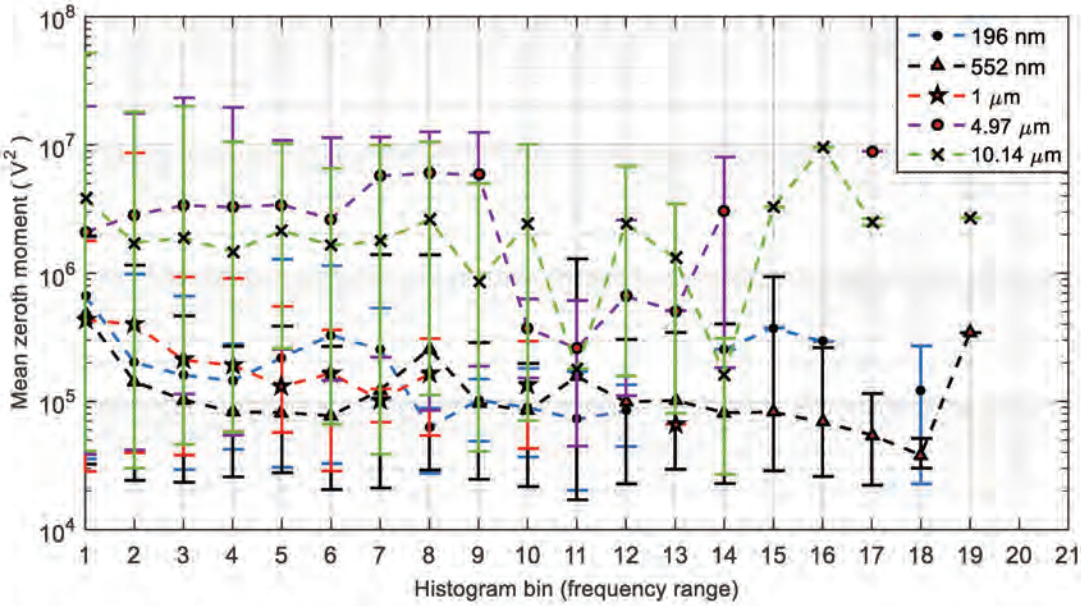

Fig. 16. Computed mean zeroth order moment among all particles for each frequency range from the histogram bin. The error bars represent the minimum and maximum M_0 values.

At first sight, it is clear by the error bars that we can't characterise the particle size by a single particle detection. We should consider a minimum number of detections in order obtain a mean quantity to evaluate a tendency for a sizing parameter. Even by that, the interpretation of the results isn't trivial as, for a same range of velocity, bigger particles are expected to induce a larger backscattered power into the laser, and thus a larger M_0 quantity while, at a quick glance, we see that is not always the case, especially for the particles of 4.97 µm and 196 nm. Anyway, for the whole frequency range, we could discriminate by the mean M_0, the 10.14 µm or 4.97 µm from the 1 µm particles and below.

4.3.6. Detection and velocimetry of large single particles

In order to evaluate the capability of the single particle detection algorithm to detect large particles seeded at very low concentration (under single particle regime) in an aqueous suspension of smaller particles with concentration high enough to generate a single scattering regime for the mixture, we have performed experiments with mixtures of two aqueous suspensions made with particles of two different diameters.

Beyond the fact of being a further step on particle characterisation with OFI, the potential application of OFI sensing in the biomedical field for blood clot (thrombus) detection is among the main motivations for these experiments.

The mixtures used for our initial prospections were obtained by mixing aqueous suspensions as follows:

a) one seeded with 10.14 μm spheres and another seeded with 110 nm spheres, in a way that the concentration for each particle size in the final mixture corresponded to: 4.3×10^{5} mL^{-1} and 1.4×10^{10} mL^{-1}, respectively.

b) one seeded with 10.14 μm spheres with another one seeded with 1 μm spheres. The final concentration for each particle size in the mixture corresponded to: 2.3×10^{5} mL^{-1} and 1.4×10^{10} mL^{-1}, respectively. This was done as a next step of evaluation regarding the detectability, while reducing by around 10 times the gap between the diameter sizes.

c) one seeded with 39.63 μm spheres with another one seeded with 4.97 μm spheres, in a way that the concentration for each particle size in the final mixture corresponded to: $7\times10^{+4}$ mL^{-1} and $1.4\times10^{+7}$ mL^{-1}, respectively.

The experimental setup was kept in the same conditions as described previously. Figure 17 shows the OFI signal from a single large particle detection for each mixture.

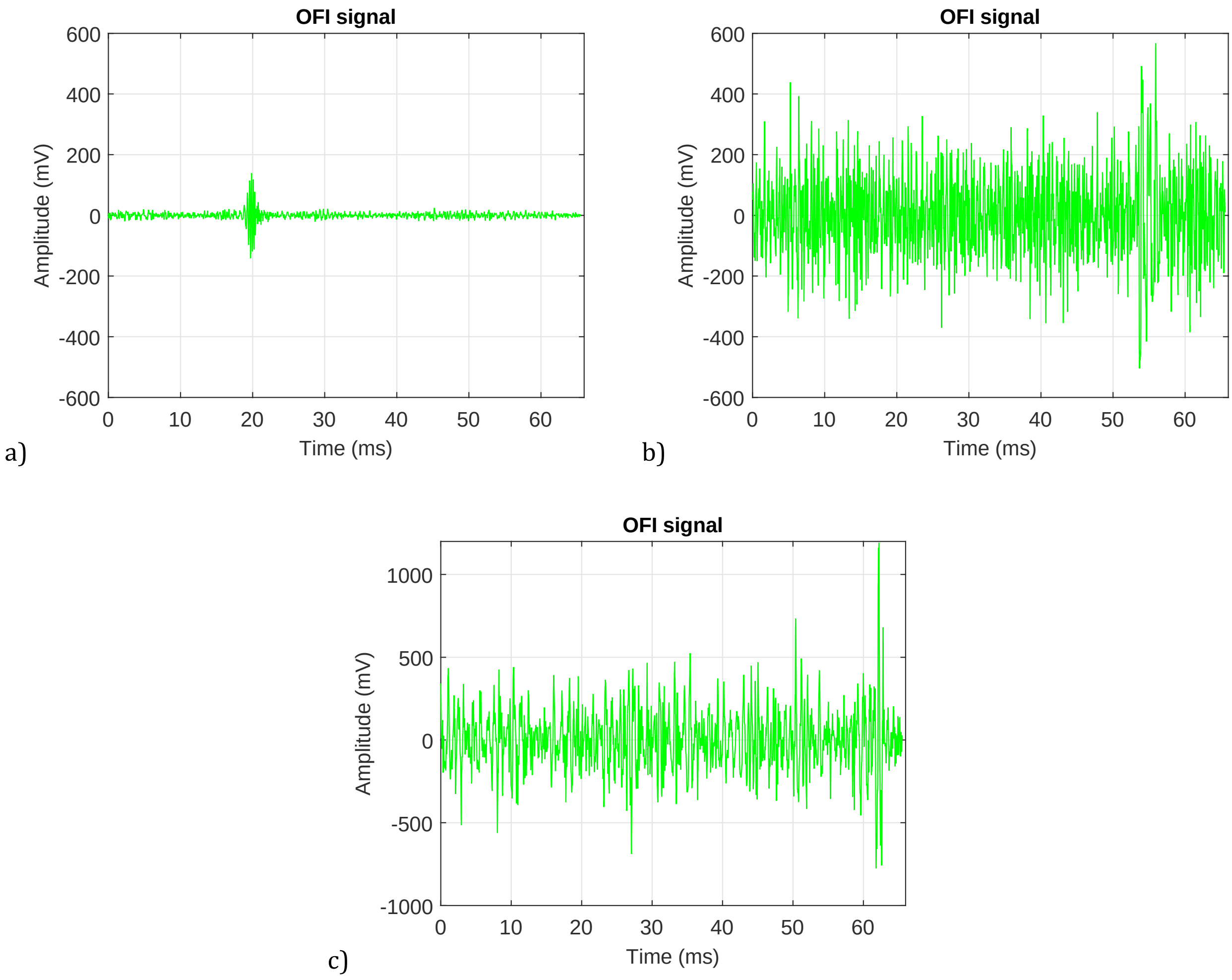

Fig. 17. OFI time domain signal before (blue) and after (green) band-pass filtering regarding: (a) a single 10.14µm sphere detected in an mixture with 110 nm spheres; (b) a single 10.14 µm sphere detected in an mixture with 1 µm spheres; (c) a single 39.63 µm sphere detected in mixture with 4.97 µm spheres.

In the filtered signals we can perceive that, by the progressive reduction of the gap between the diameters of the two particles in each mixture, the burst due to the single large particle become less distinguishable in amplitude from the background floor. At same time, we see that the amplitude levels of such floors increase. These effects can be confirmed in the spectral domain either, as shown in *Fig.* 18.

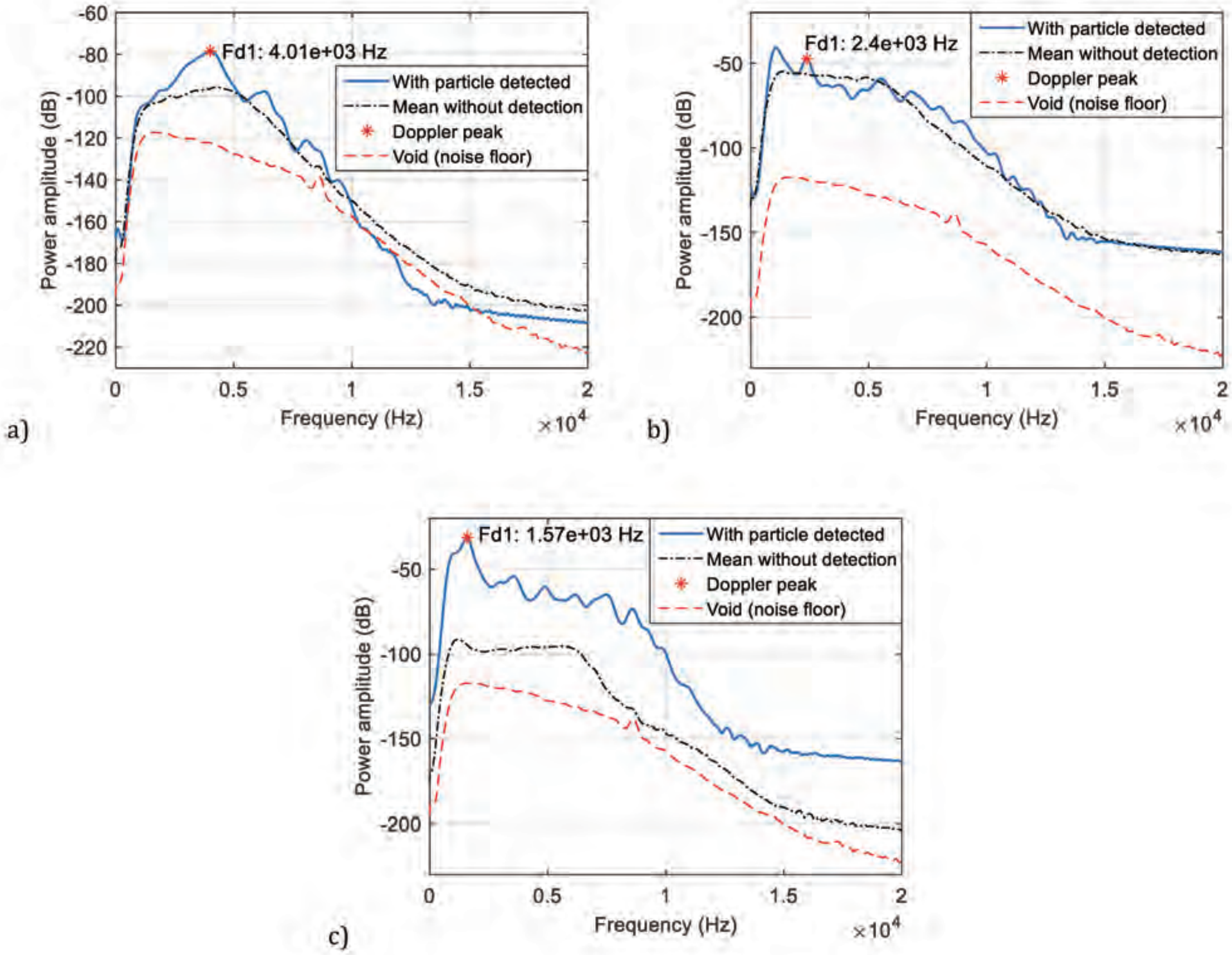

Fig. 18. Filtered signal spectrum (blue solid line) compared to the computed mean of filtered sensor signal spectrum in absence of the bigger single particle (black dashed line), so corresponding only to the smaller spheres under single scattering regime. The computed mean of the filtered OFI noise floor spectrum (red dashed line) is indicated as reference. The Doppler peak (red asterisk) corresponds to the particle velocity (V_T) accordingly Eq. 2.1 for f_D, regarding the bigger single PS sphere detected: (a) 10.14μm with $f_D \approx 4$ kHz, among 110nm spheres; (b) 10.14μm with $f_D \approx 2.4$ kHz, among 1 μm spheres; (c) 39.63μm with $f_D \approx 1.6$ kHz, among 4.97 μm spheres.

We should highlight that the morphology of the averaged spectra (dashed lines) without large particle detection corresponds to the ones observed for the single scattering regime. For each detection of a single large particle, the a spectral Doppler peak is emerging from the averaged spectra.

In the burst scanning graphs (*Fig. 19*) we observe similar burst shapes as in the previous configuration, thus validating the nature of the signal detected.

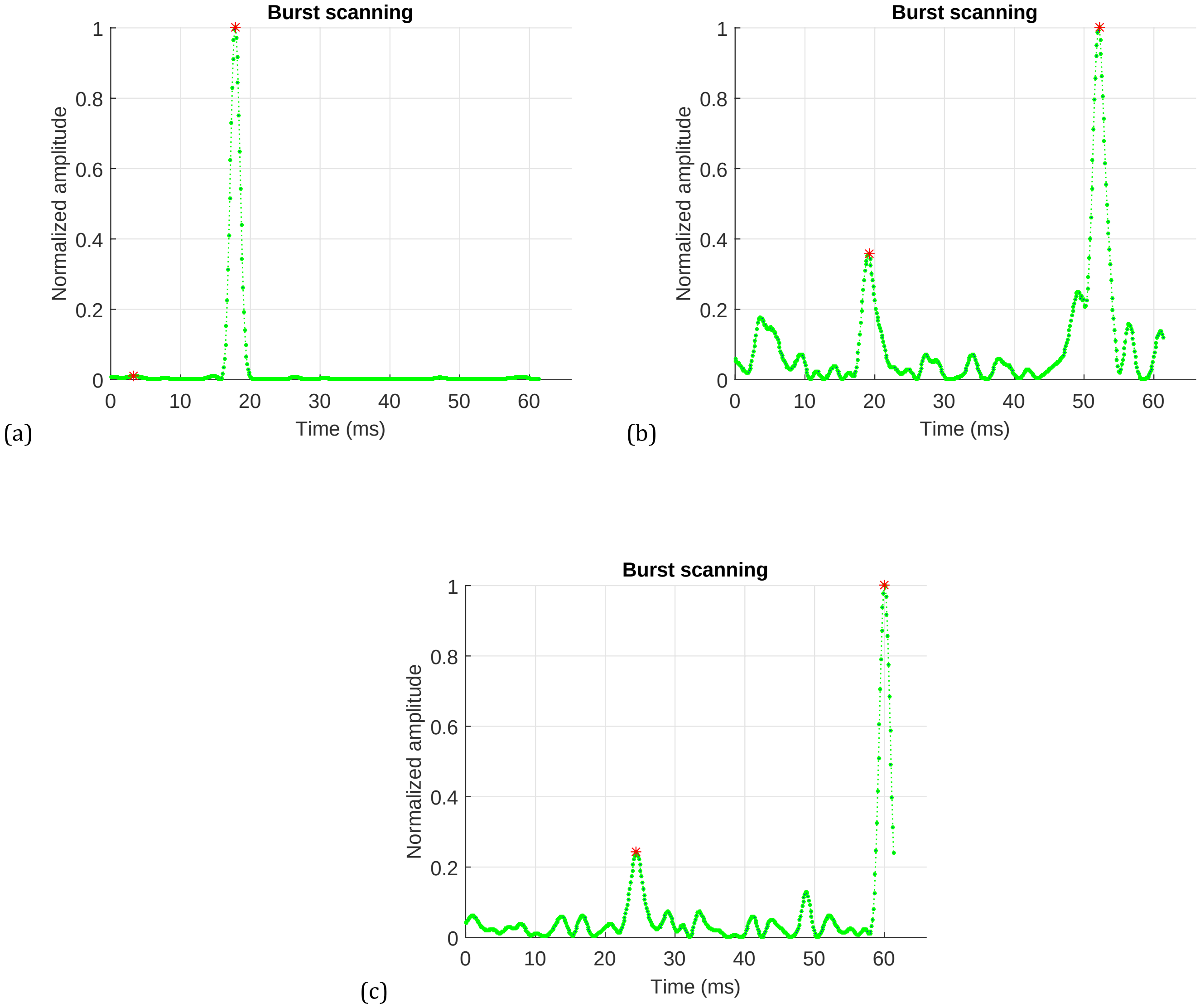

Fig. 19. Burst scanning graph revealing the burst positioning in the acquisition window for the bigger single (a), (b) 10.14 µm and (c) 39.63 µm sphere detected in the mixture.

The usual prominence condition from the burst scanning was normally attended for the first mixture (10.14 µm with 110 nm spheres), where the diameter gap was large enough. But we should highlight that for the second mixture

(10.14µm with 1µm spheres), it was necessary to change the prominence condition (the minimum gap between the two most prominent peaks, from 0.9 to 0.6) in order to select the related large particle detection.

For the third mixture (39.63 µm with 4.97 µm spheres), we should remember that 39.63 µm particles are heavy and sink too fast, avoiding any homogeneity for the mixture. Thus, during most of time of the experiment we observed no large particle detection, while by the end of the experiment multiple large particle detections in a single acquisition window were measured. For that reason, it was still very difficult to have an acquisition selected by the burst scanning procedure.

As it could be observed with the results detailed in this topic, the detection of a unique large particle in a flow of smaller ones is not trivial under the conditions we have set. It requires a minimum factor of 10 on the particles' diameter.

However, for finer discrimination at single particle regime, the use of 3D hydrodynamic particle focalization technology could be of great benefit as it would considerably reduce the uncertainty on the frequency and reduce the width of the burst. This could be achieved by the use of a more complex microchannel design. In that way, all particles would be aligned in the central axis of the microchannel, consequently holding a unique constant velocity with low standard deviation for a constant pumping flow rate. This approach could contribute to guarantee a more constant particle scattering cross-section regarding the laser spot. In that way, once the laser beam would be focalized in the central axis of the microchannel, we would have a higher probability that the particle will be mostly passing in the waist of the focused beam.

4.3.7. Micro and nanoparticle characterization under single scattering regime

Inspired by the observations gathered with the previous experiments, a further step of our present research of micro and nanoparticle characterization has been performed under the single scattering regime. In this case, beyond the flow rate, we tried to quantify the particle size and the particle concentration.

We show experimentally that our method goes beyond the one firstly presented by Zakian [17, 18], as our method concerns flowing suspensions (while Zakian uses steady suspensions only) and addresses not only nano-scale but also micro-scale particles. Eventually, we added the capability to evaluate the particle concentration in the suspension.

The experimental setup is similar to the one for single particle detection apart for the particle concentration of the polystyrene spheres that ensures the single scattering regime operation. Similarly to the flowmetry experiments performed in the Chapter 2, we have computed the average spectra of OFI signals acquired at different particle concentrations in five constant flow rates from 10 to 50 µL/min. From the spectral analysis based on the computation of the zeroth order moment we intend to quantify the particle size and concentration.

For the computation of each spectrum, the OFI signal was acquired with 2^{17} samples at 2 MHz sampling rate. Then, averaging FFTs of consecutive acquisitions was computed and smoothed using a Savitzky-Golay filter.

Figure 20 shows the average from thirty OFI spectra computed for aqueous suspensions made with the smallest polystyrene spheres (110 nm diameter). The computed spectra obtained for different particle concentrations at a constant flow rate of 50µL/min are plotted. For this particle size, at the particle concentration of $1.4\times10^{+8}$ mL^{-1} no spectral peak is observed, and for the higher concentrations a frequency Doppler peak appears and remains stable across the different concentrations.

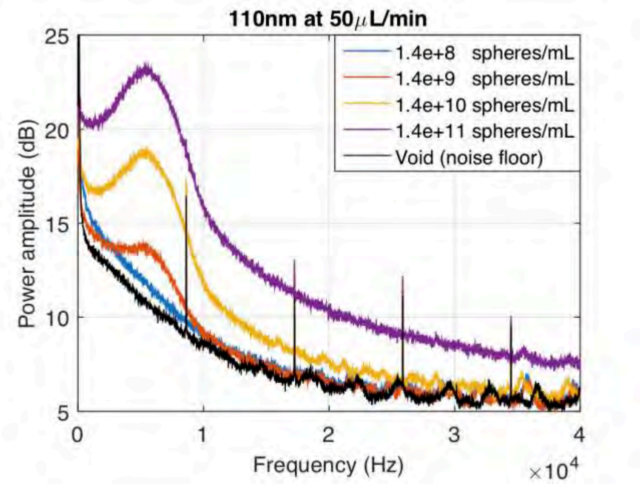

Fig. 20. Computed spectra of the OFI signal measured for 110 nm aqueous suspensions at a constant flow rate of 50 μL/min for different particle concentrations.

From each spectrum obtained, the subtraction – in linear scale - of the reference spectrum measured for the empty channel (corresponding to the noise floor of the system) was performed. Over the resulting spectrum, we have computed the zeroth order moment for the whole spectrum without any truncation. For each flow rate at a given concentration, we have performed 30 consecutive measurements in order to evaluate the standard deviation of the zeroth moment parameter.

Particle sizing

It's usual to the commercial particle sizing systems to specify a measurement range for the particle size, defining a specific particle concentration for the aqueous suspension under measurement. In our case, our experiments were limited by the specification of the flowmeter associated to the flow rate control for our pumping system. In order to avoid the pumping system clogging, the particle fraction of the diluted aqueous suspension must be below 1% w/v. That is the reason why, under a particle concentration of $1.4\times10^{+11}$ mL^{-1} for example, we could perform measurements only with aqueous suspensions made with polystyrene spheres of 110 and 196 nm. Using the data of Table 4.1 we can see that for the particle size of 552 nm, the mother suspension concentration is 5.35 $\times 10^{+11}$ mL^{-1} with 5% w/v. So we have kept $1.4\times 10^{+11}$ mL^{-1} as the maximum particle concentration for all solutions tested in this section.

As our main goal was to be able to quantify and discriminate particles at the nanometric range, and considering the fact that we could not detect any Doppler peak for the 110 nm at the $1.4\times 10^{+8}$ mL^{-1}, we have defined this particle concentration as the lowest for our particle sizing experiments. In this context, the biggest particles concerned were the ones of 4.97 µm, as the mother suspension concentration for 10.14 µm is 1.83 $\times 10^{+8}$ mL^{-1} with 10% w/v.

Figure 21 shows the computed zeroth order moment for measurements of aqueous suspensions made with four different particle sizes (110 nm, 196 nm, 552 nm and 1 µm) at the same particle concentration of $1.4\times 10^{+9}$ mL^{-1} pumped at the five constant flow rates (10-50 µL/min). The error bars represent the minimum and maximum values among the thirty computations of the zeroth moment. We can see that for this particle concentration we can always discriminate the particle size, not only by the mean value of the zeroth order moment parameter over the full set of detected particles, but also, by the computation of the zeroth order moment in any single measurement. As we have observed throughout our experiment that dependence of the mean M_0 quantity with the flow rate could be neglected, for the next graphs we will ignore this aspect and present comparisons over the average of the mean values across the five flow rates.

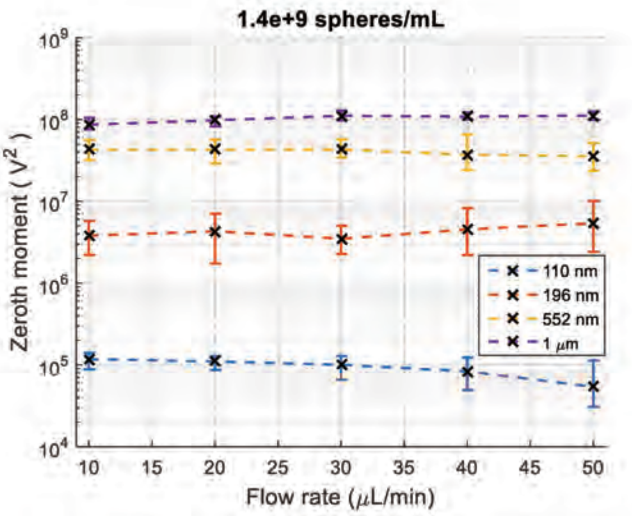

Fig. 21. Mean zeroth order moment computed from 30 consecutive measurements related with aqueous suspensions with particle concentration of $1.4\times10^{+9}$ mL^{-1} made respectively with particles of 110 nm, 196 nm, 552 nm and 1 μm; pumped at five flow rates (10-50 μL/min). Error bars indicate the minimum and maximum values of the zeroth moment from the 30 consecutive measurements.

Figure 22 shows the computed average zeroth order moment concerning the measurements of aqueous suspensions made with different particle sizes at a same particle concentration ($1.4\times10^{+8}$, $\times10^{+9}$, $\times10^{+10}$ and $\times10^{+11}$ mL^{-1}).

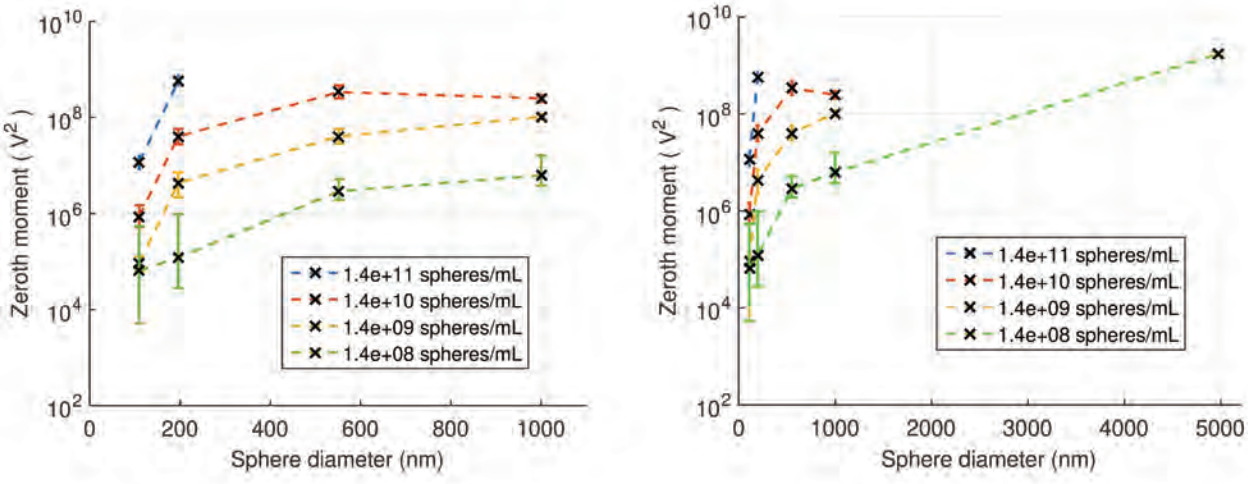

(a) (b)

Fig. 22. Average across the five flow rates (10-50 μL/min) of the mean zeroth moments computed from 30 consecutive measurements related with aqueous suspensions with four particle concentrations of $1.4\times10^{+8}$, $\times10^{+9}$, $\times10^{+10}$, $\times10^{+11}$ mL^{-1} made with (a) 110, 196, 552 nm, 1 μm PS spheres, and (b) adding 4.97 μm PS spheres. Error bars indicate the minimum and maximum average of the mean values across the five flow rates.

As we can easily see, for a same particle concentration, in most of the cases we can discriminate the particle size by the M_0 parameter. Anyway, we see that there is not a large difference between: 110 versus 196 nm in the lowest concentration ($1.4\times10^{+8}$ mL^{-1}); and 552 nm versus 1 µm (in $1.4\times10^{+8}$ and $\times10^{+9}$ mL^{-1}), which unexpectedly in $1.4\times10^{+10}$ mL^{-1}, 552 nm slightly overcomes the 1 µm.

Our explanation is that for the two smallest particles (110 and 196 nm) in the lowest concentration, the number of spheres contributing to the laser sensing volume is not large enough to differentiate them.

In the case for the M_0 quantity for 552 nm approaching the one for 1 µm at $1.4\times10^{+8}$, $\times10^{+9}$ mL^{-1} and slightly overcoming it for $1.4\times10^{+10}$ mL^{-1}, we believe possible that some interferometric effect implied by the proximity between the particle diameter and the half-wavelength of the laser. 552 nm particle have demonstrated a specific detectability in the whole frequency range (as shown in *Fig.14* for 40µL/min). *Fig. 23* shows the average spectra from the 30 consecutive measurements for 552 nm and 1 µm particles at 40µL/min and 50µL/min flow rates. *Fig. 23a* shows the spectra at $1.4\times10^{+8}$ mL^{-1} and *Fig. 23b* shows the spectra at $1.4\times10^{+10}$ mL^{-1}.

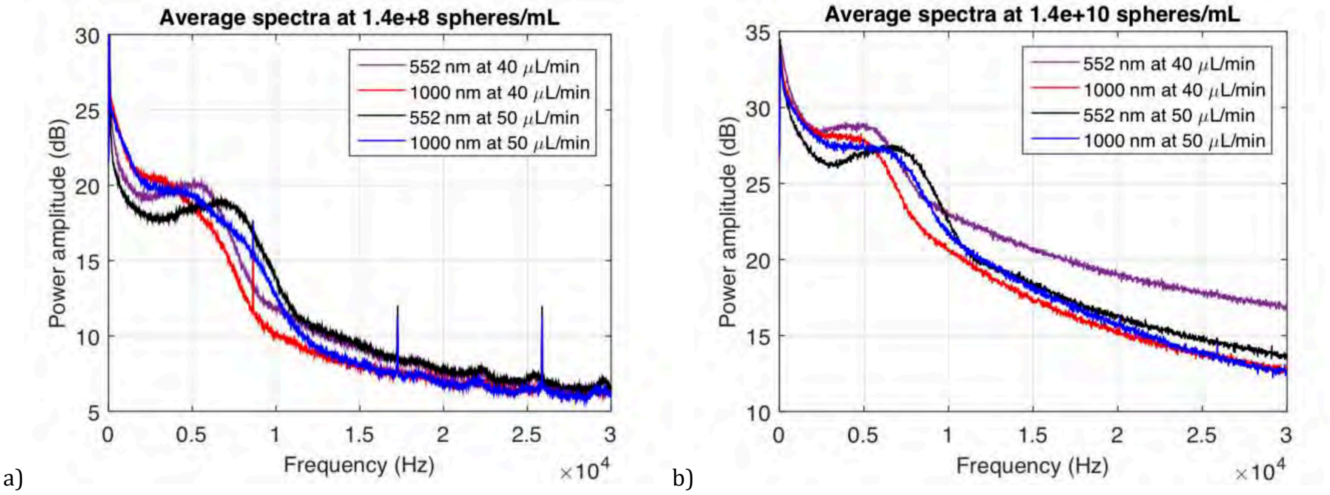

Fig. 23. Computed spectra averaged from 30 consecutive measurements concerning aqueous suspensions made with 552nm and 1μm PS spheres at (a) $1.4\times10^{+8}$ mL^{-1}, and (b) $1.4\times10^{+10}$ mL^{-1} particle concentrations.

Quantification of particle concentration

Using the same zeroth order moment parameter and procedure as explained for particle sizing, we can also discriminate the particle concentration for aqueous suspensions made with a unique particle size.

Figure 24 shows the computed average zeroth order moment of aqueous suspensions made with a given particle diameter at different particle concentrations, pumped at the five constant flow rates.

Obviously, for a given particle size, in most of the cases we can discriminate the particle concentration by the M_0 parameter, except for 110 nm at the two lowest concentrations ($1.4\times10^{+8}$ and $\times10^{+9}$ mL^{-1}).

Although we lacked of resolution in the dispersions, we can observe in almost all cases a linear relationship between the concentration and the M_0 parameter which is a good indication that with a dedicated methodology it could be possible to perform proper quantification of the particle density using this method.

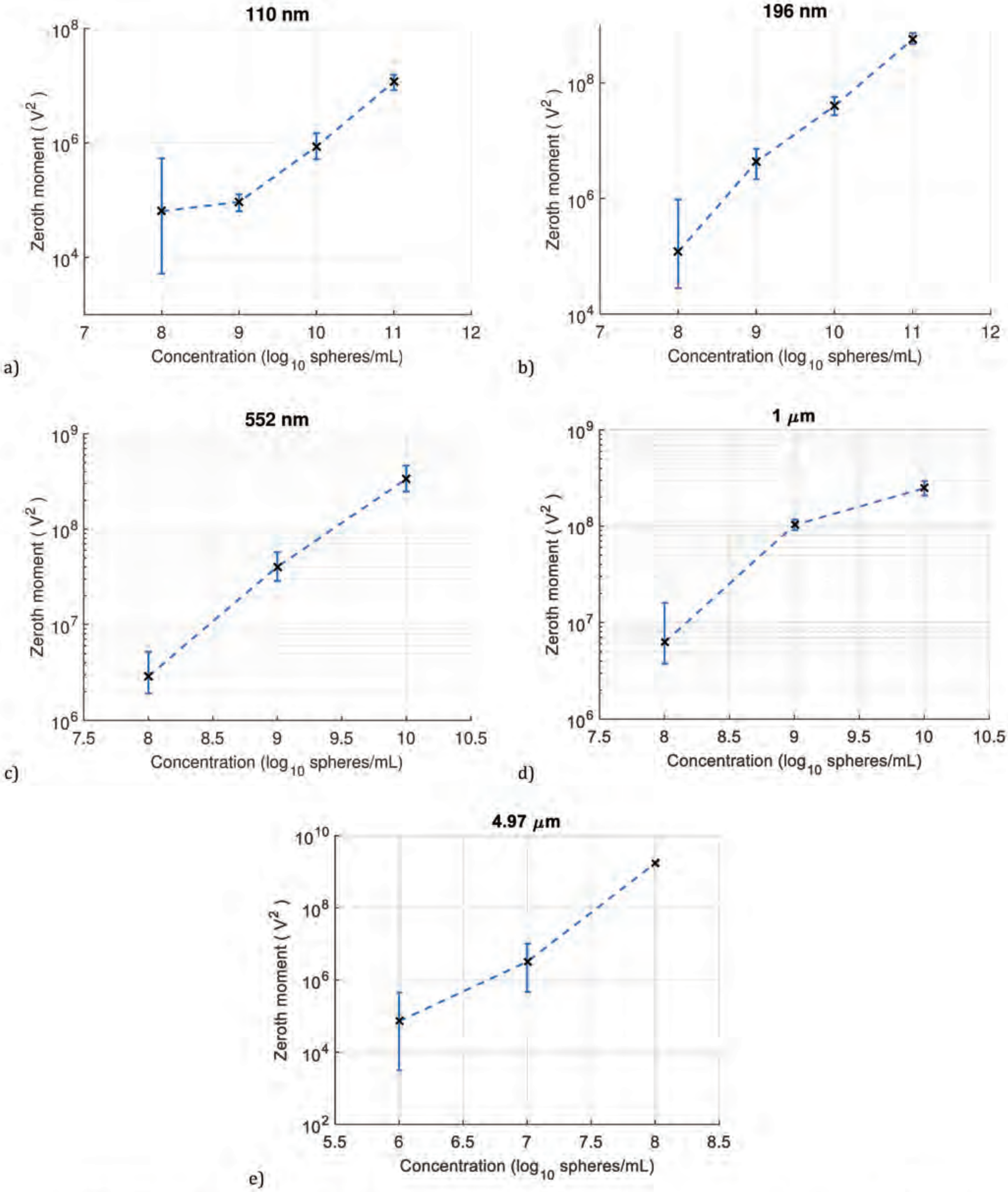

Fig. 24. Average across the five flow rates (10-50 μL/min) of the mean zeroth moments computed from 30 consecutive measurements regarding aqueous suspensions made with PS spheres of: (a) 110 nm ($1.4\times10^{+8}$, $\times10^{+9}$, $\times10^{+10}$ mL^{-1}), (b) 196 nm ($1.4\times10^{+8}$, $\times10^{+9}$, $\times10^{+10}$, $\times10^{+11}$ mL^{-1}), (c) 552 nm ($1.4\times10^{+8}$, $\times10^{+9}$, $\times10^{+10}$ mL^{-1}), (d) 1μm ($1.4\times10^{+8}$, $\times10^{+9}$, $\times10^{+10}$ mL^{-1}), (e) 4.97 μm ($1.4\times10^{+6}$, $\times10^{+7}$, $\times10^{+8}$ mL^{-1}). Error bars indicate the minimum and maximum average of the mean values across the five flow rates.

4.4. Conclusion

We presented an innovating OFI sensing scheme for single particle characterization that is able to address the nanoscale range. By comparison with commercial technologies for particle characterization (detection, velocimetry, quantification of size and concentration), the OFI technique, while being an optical non-invasive method, presents the benefits of higher capability of integration and compactness. The integration aspect as well as the sensor sensitivity could be improved by coupling the methodology and processing described in this chapter with the technical solution proposed by Zhao et al [19] where lenses are integrated on both the laser and the microfluidic channel with a significant improvement of the signal amplitude.

Among the main potential applications of this innovating technique, we could mention: flow cytometry; real-time cell counting; velocimetry at chemical microreactors for production of chemical substances and pharmaceuticals; biosensing for sickness diagnosis; blood clot detection; detection of solid contaminants in fluid flows, like for water quality control; and also for prospections at marine science researches.

Chapter references

1. C. Zakian, M. Dickinson and T. King. *Particle sizing and flow measurement using self-mixing interferometry with a laser diode*. IOP, Journal of Optics A: Pure and Applied Optics. **2005**, *vol.* 7, *no.* 6.
2. C. Zakian, M. Dickinson and T. King. *Dynamic light scattering by using self-mixing interferometry with a laser diode*. Applied Optics. **2006**, *vol.* 45, *no.* 10.
3. A. Alexandrova and C. P. Welsch. *Laser diode self-mixing technique for liquid velocimetry*. Nuclear Instruments and Methods in Physics Research A. **2016**, *vol.* 830, *pp.* 497-503.
4. H. Wang and J. Shen. *Power spectral density of self-mixing signals from a flowing Brownian motion system*. J. Appl. Phys. B. **2012**, *vol.* 106, *no.* 1, *pp.* 127-134, *doi:* s00340-011-4700-3
5. H. Wang and J. Shen. Fast and economic signal processing technique of laser diode self-mixing interferometry for nanoparticle size measurement. Appl. Phys. B. **2014**, *vol.* 115, *no.* 2, *pp.* 285-291, *doi*: s00340-013-5604-1.
6. K. Otsuka, K. Abe, N. Sano, S. Sudo and J. Ko. *Two-channel self-mixing laser Doppler measurement with carrier-frequency-division multiplexing*. Applied Optics. **2005**, *vol.* 44, *no.* 9.
7. K. Otsuka, K. Abe, N.Sano, S. Sudo, and J.-Y. Ko. *Two-channel self-mixing laser Doppler measurement with carrier-frequency-division multiplexing*. Appl. Opt. **2005**, *vol.* 44, *pp.* 1709-1714.
8. S. Sudo, Y. Miyasaka and K. Otsuka. *Quick and easy measurement of particle size of Brownian particles and plankton in water using self-mixing laser*. Optics Express. **2006**, *vol.* 14, *no.* 3.
9. S. Sudo, Y. Miyasaka, K. Nemoto, K. Kamikariya and K. Otsuka. *Detection of small particles in fluid flow using a self-mixing laser*. Optics Express. **2007**, *vol.* 15, *no.* 13.
10. T. Ohtomo, S. Sudo, and K. Otsuka. Three-channel three-dimensional self-mixing thin-slice solid-state laser-Doppler measurements. Appl. Opt. **2009**, *vol.* 48, *pp.* 609-616.
11. K. Otsuka. Self-Mixing Thin-Slice Solid-State Laser Metrology. **2011**, *vol.* 11, *no.* 2, *pp.* 2195-2245, *doi*: 10.3390/s110202195.
12. T. Ohtomo, S. Sudo, and K. Otsuka. *Detection and counting of a submicrometer particle in liquid flow by self-mixing microchip Yb:YAG laser velocimetry*. Appl. Opt. **2016**, *vol.* 55, *pp.* 7574-7582.
13. L. Ming-yi, W. Guo-dong L. Cheng-cui Li. *Size measurement of nano-particles with a self-mixing laser*. Proc. SPIE 8192, International Symposium on Photoelectronic Detection and Imaging 2011: Laser Sensing and Imaging; and Biological and Medical Applications of Photonics Sensing and Imaging, 81922A (19 August **2011**), *doi*: 10.1117/12.900569.
14. C. F. Bohren and D. R. Huffman. *Absorption and Scattering of Light by Small Particles*. Wiley VCH. **2012**. *isbn*: 9780471293408.
15. MiePlot: a computer program for scattering of light from a sphere using Mie theory & the Debye series, by Philip Laven. Available online: http://www.philiplaven.com/mieplot.htm (accessed on 25th December, 2018).
16. Y. Zhao, J. Perchoux, L. Campagnolo, T. Camps, R. Atashkhooei, and V. Bardinal. *Optical feedback interferometry for microscale-flow sensing study: numerical simulation and experimental validation*. Opt. Express. **2016**, *vol.* 24, *pp.* 23849-23862.
17. C. Zakian, M. Dickinson and T. King. *Particle Sizing and flow measurements using self-mixing interferometry with a laser diode*. J. Opt. A: Pure Appl. Opt. **2005**, *vol.* 7, *no.* 6, *p.* 445, 10.1088/1464-4258/7/6/029.
18. C. Zakian, M. Dickinson, and T. King. *Dynamic light scattering by using self-mixing interferometry with a laser diode*. Appl. Opt. **2006**, *vol.* 45, *pp.* 2240-2245.
19. Y. Zhao. Optical feedback sensing in microfluidics: design and characterization of VCSEL-based compact systems. Institut National Polytechnique de Toulouse. PhD Thesis defended at September 28th, **2017**.

CONCLUSIONS

The present thesis has been carried out with the general objective to improve the implementation of the Doppler optical feedback interferometry sensing technique in microfluidics systems. Its finality is to provide new potential sensing applications to OFI sensing in the fields of biomedical and chemical engineering.

In the first chapter, we have reviewed the sensing techniques in micro-scale flows and signal processing methods based on Doppler optical feedback interferometry using laser diodes. We extended the bibliography to the main flowmetry results for OFI sensors based on Speckle analysis and highlighted the superior potential of the Doppler OFI approach to support our choice. This conclusion was achieved especially while considering one of our goal: to be able to detect single micro and nanoparticles in aqueous suspensions. Then, we have introduced the definitions of the scattering regimes that governs the laser-fluid interaction and as it has been stated in the second chapter have major influence on the electrical spectrum of the sensor signal and thus on the signal processing strategy. Then, we reported the most advanced models of optical feedback effect describing the laser diode output power behavior under feedback interference provoked from a multiplicity of scatterers. For this, the rate equations ruling the the laser diodes subject to external feedback have been derived and extended to generate a simple model that takes into account the impact of a plurality of particles contributing to the laser feedback. Finally, we have exposed the main motivations of this thesis in order to place our choices in the actual sensing problematic.

In Chapter 2 we have discussed the different aspects that can affect the electrical spectrum morphology of the OFI signal, as beyond the scattering regime associated to the scatterers density, the channel physical dimensions and the sensor optical configuration play a major role. Thus, we introduced different OFI flow monitoring signal processing methods based on the spectral analysis. Three optical configurations were experimentally evaluated with a detailed comparison on the accuracy of the flow velocity measurements from single to multiple scattering regimes, performed with each of those optical configurations. In the meantime, the pertinent signal processing methods were confronted showing that it remains uneasy to deploy a unique processing approach that would remain valid over all conditions of scattering regime and optical arrangement. This analysis highlighted the performance of the optical configuration based on the use of a transmission diffraction grating that was first proposed in this thesis. This configuration reached the smallest mean relative error (0.73%) in the measurements of the relative flow velocity, with a workable relative standard deviation (2.52%) over 30 consecutive measurements.

In the chapter 3, we presented a 2D Doppler imager based on OFI that was developed during our researches for *ex-vivo* and *in-vivo* flowmetry applications in the frame of the European funded project Diagnoptics. As an intermediary prospection towards an embedded version, we have presented the setup and experiments performed with a setup on an optical table with bulk translation stage scanning systems. This first step showed the need for an innovating OFI signal processing method that includes a conditioning step in order to handle the signal high amplitude interferometric fringes induced by the vibrations due to displacement of the sensor and that were likely to occur in *in-vivo* acquisitions. This processing approach has been introduced and validated first by imaging the blood perfusion in a human radial subcutaneous vein, and second obtaining a 500-pixels image of the blood perfusion from a visible Y-shape vein in a human hand. Following that, we have presented and evaluated our design of a handheld 2D OFI Doppler flow imager that has been realized using a 2-axis beam-steering mirror mounted on a Micro-Electro-Mechanical System (MEMS). This arrangement allows to take the full advantage of the compactness offered by the OFI sensing scheme and it demonstrate that like no other OFI sensors are well suited for applications in embedded imaging systems. Besides the compactness, the MEMS mirror made possible the improvement of the scanning time by a factor of ten as comparing to the translation stages system. Finally, we have presented and discussed the results of the clinical study performed in the frame of the European funded project Diagnoptics that targeted the biomedical field of skin cancer diagnosis. In this context, the analysis of the signal acquisition with the handheld 2D OFI imager suggested offering additional information in the differential diagnosis of some skin lesions while compared to health skin of similar kind. Although these preliminary results were promising and supports the continuation of the prospections with this system, the clinical study was actually not sufficiently conclusive on the gain provided by the OFI imager. A better management of the sensor to patient movement, a higher resolution for the same scanning area seems necessary despite the consequent increasing of the rasterization time. Although the advances achieved on enhancing the robustness against mechanical noises due to inherent movements of in vivo targets, improvements are still to be done with the signal conditioning or alternative processing approach when the measurement is performed while handling the imager.

Finally, in the Chapter 4 a huge amount of our experimental works were presented that opened a new domain in OFI sensing in the context of micro and nanoparticle detection and characterization. Firstly, we defined the single particle regime and a real-time algorithm that is based on the maximum Doppler peak detection and a time-domain burst scanning for single particle detection and velocimetry in watery suspensions is described and validated experimentally. The method has been able to address the micro and nanoscale range, detecting single polystyrene spheres up to 110nm with a 785 nm laser diode. It has been shown experimentally that the same algorithm is potentially able to detect large particles seeded with a concentration that would correspond to a single particle regime, in watery suspension of smaller ones under the single scattering regime. This result was observed for various particle size and with a minimal diameter contrast of five times. In a different approach, we investigated the particle size evaluation under the multiple particles regime (in the single and multiple scattering regimes). While other existent technologies that would allow such results are bulk, they also require manipulation of the fluid, tending towards always smaller volume handling with precise flow and concentration control in order to size particles at macro or nanoscale, we have proposed the use of the compact and potentially embedded OFI technology to quantify the particle size (110 nm, 196 nm, 552 nm, 1μm, 4.97μm) and concentration ($1.4\times10^{+8}$, $\times10^{+9}$, $\times10^{+10}$ and $\times10^{+11}$ mL^{-1}) with watery suspensions at single and multiple scattering regimes, pumped under a wide flow rate range (10-50 μL/min).

In a further extension of the present study several paths were opened here that are of interest. At first, concerning a higher level of integration of the optical feedback flowmetry for embedded sensing into the microfluidic chip, custom Binary Optical Elements (BOEs) could be designed to integrate a top layer over the micro-channel design. Such BOE could replace the focal lens and the transmission diffraction grating, and could enable setting of an optimal diffraction angle that would eventually improve the feedback power ratio, as the usual transmission gratings are usually designed for forward transmission applications.

While the *in vivo* measurement and attempt of subcutaneous blood flow imaging where a major result of this thesis it remains clear that progress in the signal processing shall be addressed to actually provide clearer images of capillaries networks. Another approach could be the immunization of the sensor to vibration by mechanical or optical methods as it is most often performed in biomedical imaging devices.

Eventually, in the context of single particle detection, counting and discrimination, the actual system would take a major benefit of using custom microchannels enabling a 3D hydrofocalisation of the particles. This solution is highly suggested, as it would significantly improve the experimental control of the particle position and velocity, and thus reduce the uncertainty on many parameters that are involved in the OFI signal produced by a unique scatterer. It is not too optimistic to say that, using such microfluidic chips, the OFI sensing approach could be deployed as a new flow cytometry solution.

List of publications

Conference papers

1. R. da Costa Moreira, A. Quotb, C. Tronche, F. Jayat, T. Bosch, J. Perchoux. *An Embedded 2D Imager for Microscale flowmetry Based on Optical Feedback Interferometry*. IEEE Sensors 2016, Orlando, FL, **2016**, *pp.* 1-3. doi: 10.1109/ICSENS.2016.7808586
2. E. E. Ramírez-Miquet, R. da Costa Moreira, Y. Zhao, J. Perchoux. Particle detection and size estimation in microfluidic devices using optical feedback interferometry. VIII Taller International TECHNOLASER **2016**. LA OPTICA Y LA TECNOLOGIA LASER EN LA CIENCIA, LA INDUSTRIA Y LA CULTURA.
3. R. da Costa Moreira, J. Perchoux, Y. Zhao, C. Tronche, F. Jayat and T. Bosch. Single nano-particle flow detection and velocimetry using optical feedback interferometry. 2017 IEEE SENSORS, Glasgow, **2017**, *pp.* 1-3. doi: 10.1109/ICSENS.2017.8234105

Journal papers

1. E. E. Ramírez-Miquet, J. Perchoux, R. da Costa Moreira, Y. Zhao, A. Luna-Arriaga, C. Tronche, and O. Sotolongo-Costa. *Optical Feedback Interferometry: from basics to applications of laser flowmetry*. Rev. Cub. Fis. *vol.* 34, *p.* 48, **2017**.
2. R. Atashkhooei, E. E. Ramírez-Miquet, R. da Costa Moreira, A. Quotb, S. Royo and J. Perchoux. *Optical Feedback Flowmetry: Impact of Particle Concentration on the Signal Processing Method*. IEEE Sensors Journal, vol. 18, no. 4, pp. 1457-1463, 15 Feb.15, **2018**. doi: 10.1109/JSEN.2017.2781902

Procedures for a custom made PDMS channel

Our PDMS channels were made of silicon elastomer (Sylgard 184) which is a two-component elastomer: a silicon elastomer base, and the curing agent (mixed in a ratio of 10 to 1, respectively).

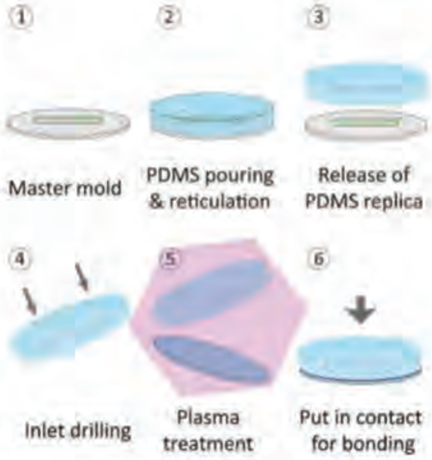

Fig. 1. 6-step fabrication for a rectangular/square PDMS microfluidic chip by softlitography technique. [1]

Figure 1 describes a 6-step procedure to fabricate a rectangular or square PDMS channel. Firstly, a master mold is designed corresponding to the channel dimension. In our case, the layout was drawn in CleWin 5 (*Fig. 2*) and the master mold was fabricated by photolitography on a silicon master in a white room. The liquid PDMS is mixed with a curing agent, and after the air bubbles are extracted by a vacuum chamber the PDMS is poured into a vertical sealed support containing the master mold. Then, it's placed into a oven (at 75 °C) to bake for 4 hours in order to harden the PDMS. Such support avoids a PDMS leakage while it's hardened, being helpful to impose a sufficient PDMS thickness as substrate. Once done, the replic is taken out from the mold and properly cut accordingly to the glass cover. Then, the inlet(s) and outlet(s) are drilled with a proper dimension (usually 1 mm) accordingly the needle or tubing size. So the PDMS is cleaned with isopropanol into an ultrasound pool for 5 min. The PDMS becomes hydrophobe. Both PDMS and the covering glass plate are exposed to plasma into the side to enable the bonding. So finally, both are set in contact to bond and put into the oven (at 75 °C) for 20 minutes to fix the bonding. The PDMS channel is ready.

Fig. 2. CleWin5 layout of the 5-inch mask for PDMS fluidic channels.

Annex reference

1. L. CAMPAGNOLO, Optical feedback interferometry sensing technique for flow measurements in microchannels. PhD thesis, Université de Toulouse, France, February 12th, **2013**.